

AFRL-IF-RS-TR-2003-48
Final Technical Report
March 2003



MASSIVELY PARALLEL POST-PACKAGING FOR MICROELECTROMECHANICAL SYSTEMS (MEMS)

University of Michigan

Sponsored by
Defense Advanced Research Projects Agency
DARPA Order No. E117


APPROVED FOR PUBLIC RELEASE; DISTRIBUTION UNLIMITED.

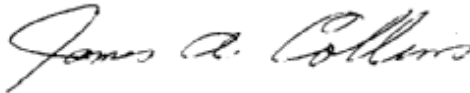
The views and conclusions contained in this document are those of the authors and should not be interpreted as necessarily representing the official policies, either expressed or implied, of the Defense Advanced Research Projects Agency or the U.S. Government.

AIR FORCE RESEARCH LABORATORY
INFORMATION DIRECTORATE
ROME RESEARCH SITE
ROME, NEW YORK

This report has been reviewed by the Air Force Research Laboratory, Information Directorate, Public Affairs Office (IFOIPA) and is releasable to the National Technical Information Service (NTIS). At NTIS it will be releasable to the general public, including foreign nations.

AFRL-IF-RS-TR-2003-48 has been reviewed and is approved for publication.

APPROVED: 
DUANE GILMOUR
Project Engineer

FOR THE DIRECTOR: 
JAMES A. COLLINS, Acting Chief
Information Technology Division
Information Directorate

REPORT DOCUMENTATION PAGE			Form Approved OMB No. 074-0188	
Public reporting burden for this collection of information is estimated to average 1 hour per response, including the time for reviewing instructions, searching existing data sources, gathering and maintaining the data needed, and completing and reviewing this collection of information. Send comments regarding this burden estimate or any other aspect of this collection of information, including suggestions for reducing this burden to Washington Headquarters Services, Directorate for Information Operations and Reports, 1215 Jefferson Davis Highway, Suite 1204, Arlington, VA 22202-4302, and to the Office of Management and Budget, Paperwork Reduction Project (0704-0188), Washington, DC 20503				
1. AGENCY USE ONLY (Leave blank)		2. REPORT DATE MARCH 2003	3. REPORT TYPE AND DATES COVERED Final May 98 – May 02	
4. TITLE AND SUBTITLE MASSIVELY PARALLEL POST-PACKAGING FOR MICROELECTROMECHANICAL SYSTEMS (MEMS)			5. FUNDING NUMBERS C - F30602-98-2-0227 PE - 63739E PR - E117 TA - 00 WU - 41	
6. AUTHOR(S) Liwei Lin and Kensall Wise				
7. PERFORMING ORGANIZATION NAME(S) AND ADDRESS(ES) University of Michigan Division of Research Development and Administrations Room 1058, 3003 S. State Street Ann Arbor Michigan 48109-1274			8. PERFORMING ORGANIZATION REPORT NUMBER	
9. SPONSORING / MONITORING AGENCY NAME(S) AND ADDRESS(ES) Defense Advanced Research Projects Agency AFRL/IFTC 3701 North Fairfax Drive Arlington Virginia 22203-1714			10. SPONSORING / MONITORING AGENCY REPORT NUMBER AFRL-IF-RS-TR-2003-48	
11. SUPPLEMENTARY NOTES AFRL Project Engineer: Duane Gilmour/IFTC/(315) 330-3550/ Duane.Gilmour@rl.af.mil				
12a. DISTRIBUTION / AVAILABILITY STATEMENT APPROVED FOR PUBLIC RELEASE; DISTRIBUTION UNLIMITED.				12b. DISTRIBUTION CODE
13. ABSTRACT (Maximum 200 Words) This project has achieved many accomplishments toward "Massively Parallel Post-Packaging for MEMS." These achievements can be summarized as follows: (1) innovative bonding processes; (2) post-fabrication packaging demonstrations and characterizations on various MEMS devices; and (3) demonstrations and characterizations of post-fabrication device trimming. In summary, we were able to develop several new localized bonding processes, including eutectic bonding, fusion bonding, solder bonding, chemical vapor deposition (CVD) bonding, nano-second laser welding, inductive heating and bonding, ultrasonic bonding and rapid thermal processing (RTP) bonding. Every bonding process represents technology innovation and advancement. In addition, new material bonding systems were also investigated and established. These include aluminum-to-glass, aluminum-to-nitride, and aluminum-to-aluminum bonding systems. The new bonding processes and systems make possible the device encapsulation demonstrations, such as vacuum encapsulated micro resonators, by using localized aluminum-to-glass bonding, RTP bonding and localized CVD bonding. These vacuum bonded devices have gone through various types of characterization, including quality factor measurements, long-term stability monitoring and accelerated tests. In another device packaging area, selective trimming of micro resonators was successfully demonstrated by three different schemes, including active trimming by a localized heating and stressing effect, permanent trimming by localized CVD deposition and by pulsed laser deposition.				
14. SUBJECT TERMS MEMS, Microelectromechanical Systems, Vacuum Packaging, Localized Heating, Localized Bonding, Packaging, Trimming, Resonator, Encapsulation, Eutectic Bonding, Fusion Bonding, Solder Bonding, CVD Bonding, RTP Bonding, Inductive Heating, Accelerated Testing			15. NUMBER OF PAGES 68	
			16. PRICE CODE	
17. SECURITY CLASSIFICATION OF REPORT UNCLASSIFIED	18. SECURITY CLASSIFICATION OF THIS PAGE UNCLASSIFIED	19. SECURITY CLASSIFICATION OF ABSTRACT UNCLASSIFIED	20. LIMITATION OF ABSTRACT UL	

Table of Contents

1.0 Executive Summary	1
2.0 Introduction.....	2
3.0 Methods, Assumptions, and Procedures	3
3.1 Task I: Characterization of Localized Heating, Bonding and Deposition.....	4
3.2 Task II: Selective Encapsulation for MEMS Post-Packaging	4
3.3 Task III: Massively Selective Trimming	5
4.0 Results and Discussion	6
4.1 Task I: Characterization of Localized Heating, Bonding and Deposition.....	6
4.1.1 Localized Eutectic/Fusion Bonding Process.....	6
4.1.2 Localized PSG (Phosphorous Silicate Glass)-to-Glass Bonding Process by Using PSG as the Intermediate Layer	7
4.1.3 Localized Indium-to-Glass Bonding Process with Indium as the Intermediate Layer	8
4.1.4 Selective and Localized Hermetic Bonding using Inductive Heating	9
4.1.5 MEMS Post-packaging by Nanosecond Laser Technology	11
4.1.6 Localized Ultrasonic Bonding Process	15
4.1.7 Residual Stress Analysis of Thermal Bonding Processes for MEMS Packaging	16
4.2 Task II: Selective Encapsulation for MEMS Post-Packaging	19
4.2.1 Vacuum Packaging Technology Using Localized Aluminum/Silicon-to-Glass Bonding.....	19
4.2.2 Localized CVD Bonding for MEMS Post-Packaging	25
4.2.3 Zinc Bonding for MEMS Packaging at the Wafer-Level	29
4.2.4 Massively Parallel MEMS Post-Packaging by Using Aluminum-to-Nitride RTP Bonding	32
4.2.5 Vacuum Packaging Using Localized CVD Deposition	36
4.2.6 Reliability Tests of MEMS Packages	41
4.3 Task III: Massively Selective Trimming	47
4.3.1 Frequency Tuning Using Electro-Thermal Effects.....	47
4.3.2 Frequency Tuning Using Localized CVD Deposition.....	49
4.3.3 Frequency Tuning Using Pulsed Laser Deposition (PLD)	51
5.0 Conclusions and Recommendations	53
5.1 Conclusions.....	53
5.2 Recommendations.....	53
Bibliography	55
List of Publications	57
Journals	57
Conferences.....	58

List of Figures

Figure		Page
1	A MEMS sensor with pre-fabricated microelectronics.	5
2	Schematic diagram of MEMS post-packaging by localized sealing.	5
3	MEMS post-trimming by a global deposition process.	5
4	Eutectic bonding by global heating.	6
5	Eutectic bonding by localized heating.	6
6	Localized fusion bonding.	7
7	Microheater shows up after HF dipping.	7
8	A SEM micrograph of the silicon substrate showing the PSG is stripped.	7
9	A SEM micrograph of the glass cap showing PSG is bonded to the glass.	7
10	A SEM micrograph of the silicon substrate after breaking the indium-glass bond.	8
11	A SEM micrograph of glass cap after breaking the Indium-glass bond. Indium is uniformly attached to the glass cap.	8
12	Indium solder reflows after heating to seal the gap created by the interconnection.	8
13	Induction heating and bonding concept; using externally applied alternating magnetic field to induce eddy currents and resistive heating in a metallic bonding ring	9
14	Induction heating setup using an 8 turned helical coil driven between 10-15MHz.	10
15	Measured temperature with respect to time of 4 μ m thick, 200 μ m-wide and 1mm diameter gold bonding ring under varying induction heating power.	10
16	Temperature distribution in a 50mm wide aluminum bonding ring on Pyrex wafer heated with 1kW for 100ms.	10
17	Pyrex to Pyrex bonding using 1mm diameter, 200mm wide, 4mm thick gold solder ring with 20nm of Cr adhesion layer on both Pyrex surfaces.	11
18	Two halves of a forcefully broken cavity bonded with 1.5kw for 3 seconds.	11
19	The experimental set up of glass-to-silicon bonding with an intermediate layer of indium and a built-in mask.	12
20	A top view of the laser welding result where glass-to-indium bond is formed.	12
21	A side view (SEM) of the bonding spot after we break the glass-to-indium bond: (a) on the glass layer, (b) on the indium layer	12

List of Figures (Con't)

Figure		Page
22	A top view of the bonding result using a built-in mask after random laser shots on the mask: (a) a ring-shape pattern as the mask with the outer diameter of 4 mm and inner diameter of 1.8 mm, (b) bonding result with the bonding area of the same size as that of the pattern. The laser-beam size is 1 mm in diameter, smaller than the radial length of the ring pattern of 1.1 mm.	13
23	Schematic representation of the laser welding process of the system.	13
24	Two simulation (software ANSYS 5.5) results of heat-affected zones on the cross section after the indium layer absorbs energy under irradiation of laser beam with diameter of 1mm and output energy 22 mJ: (a) The result after 1ms, (b) The result after 1 second.	15
25	Schematic setup of the process.	16
26	Ultrasonic hermetic sealing results.	16
27	Schematic diagram of the bonding system analyzed.	16
28	Mask design.	16
29	Quartz bonded to silicon with an aluminum bonding strip.	17
30	FEM thermal analysis of the cooling after global heating (at .3 seconds).	17
31	FEM residual stress analysis using temperature dependent properties for all materials.	17
32	FEM residual stress analysis including non-linear stress-strain properties for aluminum.	18
33	Localized aluminum-glass bond after breaking the bonding interface. (a) part of glass is attached to the silicon substrate. (b) part of aluminum is attached to the glass substrate	20
34	Enlarged views of localized bonding results. (a) aluminum/silicon-glass bond, (b) aluminum-glass bond.	20
35	Bonding interface after type-A aluminum etching.	21
36	Bonding interface after TMAH etching.	21
37	Fabrication process flow of vacuum encapsulation using localized aluminum/silicon-to-glass bonding.	22
38	SEM microphoto of folded-beam μ - resonators.	23
39	Enlarged view of folded-beam μ -resonators.	23
40	The SEM photograph of encapsulated μ -resonators after the glass cap is forcefully broken away.	24
41	The frequency spectrum of glass encapsulated μ -resonator with 90 minutes wait time in vacuum ($Q=2500$).	24
42	Simulation result of the cavity pressure versus the gas resident time inside the cavity.	24
43	The frequency spectrum of glass encapsulated μ -resonator with 90 minutes wait time in vacuum.	24

List of Figures (Con't)

Figure		Page
44	(a) Schematic diagram of the bonding test. (b) localized CVD polysilicon has filled and sealed the gap.	25
45	Top view of the device substrate showing interconnection line and detached microheater.	26
46	SEM photo of the packaging cap showing trails of localized CVD polysilicon.	26
47	Selectively deposited polysilicon has filled the 1 μm deep gap. (a) The intersection of the interconnection line and microheater. (b) The close view showing step coverage.	26
48	Step coverage after dipping in 10:1 HF for 30 seconds and silicon etchant for 5 seconds.	27
49	Cross sectional view of localized CVD bond.	27
50	Cross sectional view of a cleaved CVD bond.	28
51	The profile of localized CVD polysilicon.	28
52	FEA temperature stimulation.	28
53	Localized CVD polysilicon is uniformly deposited on a rectangular heater, 1000 x 800 μm^2 , to enclose MEMS devices.	28
54	(a) Device substrate after CVD bonding. (b) Cap substrate after CVD bonding.	29
55	Schematic of the zinc bonding process: The electroplated zinc is bonded to the metal (Au) on the cap under a bonding temperature of 425°C while the electroplated nickel is not melted.	30
56	Microfabrication process for the zinc bonding: zinc is electroplated on top of electroplated nickel; zinc is melted for bonding at 425°C, while nickel is not melted at this temperature and nickel functions as the structural layer to form the cavity.	30
57	SEM photograph of the electroplated nickel and zinc before bonding.	31
58	Enlarged view of A in Fig. 57. The zinc is electroplated on the top of the electroplated nickel.	31
59	SEM photograph of the silicon substrate after zinc bonding. The bonded wafer was forcefully broken.	32
60	Enlarged view of B in Figure 59. The broken silicon substrate suggests that the bonding strength between zinc & gold is comparable to the fracture toughness of silicon.	32
61	Enlarged view of C in Figure 59. Electroplated nickel is covered with recrystallized zinc, generated after heating; the torn zinc is on the top of nickel.	32
62	The Schematic diagram of massively parallel MEMS post-packaging by using RTP aluminum-to-nitride bonding.	33

List of Figures (Con't)

Figure		Page
63	A comb resonator is resonating at 17kHz while immersed in DI water.	33
64	Glass debris is attached to the silicon substrate after forcefully breaking the bond.	33
65	X-ray diffraction (XRD) spectrum result at the bonding interface.	34
66	Experimental tests of RTP bonding showing an activation energy of 2.5eV for the aluminum-to-nitride bonding system.	34
67	Quartz tube for the RTP vacuum packaging process.	34
68	Long-term stability tests of Q for 37 weeks. Q is found increasing with pre-baking time in vacuum.	35
69	Accelerated testing results of a vacuum-packaged comb-resonator. The Q stays at 200 after 24 hours of testing time in harsh environment.	35
70	SEM microphoto of silicon substrate after forcefully breaking the bond. Bulk glass is found on the silicon substrate.	36
71	Schematic diagram of the packaging approach.	36
72	An optical photograph of a device array.	37
73	Photographs of a single device and its contents.	38
74	A transmission spectra obtained from a packaged comb resonator.	38
75	Quality factor vs. pressure obtained from an unpackaged resonator.	39
76	An optical photograph of the fabricated pressure sensor array.	39
77	Layout of the absolute pressure sensor.	39
78	Optical photograph of a single device (back side view) and its contents.	40
79	Optical photograph showing the details of the sealing channel region.	40
80	Pressure vs. change in C obtained from some of the fabricated pressure sensors.	40
81	Schematic diagram of hermetic package fabricated by localized aluminum/Si-to-glass bonding.	41
82	Optical photograph of the hermetic package seen through the glass capsule.	41
83	Results from the autoclave test. After 30 hours, a drastic change is measured.	42
84	Moisture condensation is found inside the package on the sensor.	42
85	Statistical autoclave test results of another 11 packages produced by increasing bonding time and pressure.	43
86	Schematic of bonding by RTP (Rapid Thermal Processing).	44

List of Figures (Con't)

Figure		Page
87	Sealed cavities by RTP bonding with solder widths of 50, 100 and 150 μm .	44
88	Hermetic sealing is demonstrated by immersing into IPA liquid.	45
89	Glass wafer under SEM after breaking the bond.	45
90	IPA leak test by immersing packaged die into IPA for 240 hours. Where “h” is the aluminum solder thickness.	45
91	Autoclave test by putting packaged die in a 120 ⁰ C, 20.7 Psi steam chamber for 80 minutes after passing IPA tests.	45
92	Statistical failure function verses time for accelerated testing analysis.	46
93	Schematic diagram of a tunable comb-shape resonator. Beam 1 is the heating and tuning beam.	47
94	Electrothermal model showing the elements of each discrete nodes. A total of 124 nodes were used.	47
95	Transient temperature simulation indicates 0.2 msec is required for heating to reach steady state.	48
96	Temperature distribution of the microsystem based on the electrothermal model.	48
97	A simplified model for dynamic analysis.	49
98	(a) Frequency response of a tunable resonator at 5 different tuning amperages. (b) Variation of resonant frequency vs. tuning power for 5 different devices compared to theoretical model.	49
99	Design layout of the special comb-drive resonator for tuning using selective polysilicon deposition.	50
100	SEM of special comb-drive resonator with selectively deposited polysilicon. The change in resonant frequency was 2.6%.	51
101	The schematic diagram of the post-packaging frequency tuning process by PLD for MEMS resonators.	51
102	SEM microphoto shows indium is deposited onto a resonator shuttle plate using PLD.	52
103	Spectrum measured by a micro-stroboscope for a resonator before and after PLD. A frequency shift of -1.2% is observed.	52
104	Experimental results showing the linear correspondence of Δf and $[(m_0 / (m_0 + \Delta m))^{0.5} - 1]$ as predicted by the undamped vibration model.	52

1.0 Executive Summary

The research covered in this report was motivated by the packaging needs for MEMS (Microelectromechanical Systems) devices. In the conventional IC industry, up to 95% of the manufacturing cost may be attributed to the packaging processes^{*}[1]. For MEMS devices, this number may go even higher due to the stringent packaging requirements for microstructures. In the past, anodic bonding [2]; fusion bonding [3]; reactive gas sealing [4] and LPCVD sealing [5] processes have been used to encapsulate MEMS devices. However, none of them are suitable for the general purpose of MEMS post-packaging at low temperature at the wafer-level and at low cost. We have developed and demonstrated several MEMS post-packaging procedures based on localized heating and bonding, that are insensitive to the various possible MEMS fabrication processes, with three technical tasks in this project, as described below. The fourth task is a non-technical one on the establishment of a MEMS technical division in ASME (American Society of Mechanical Engineers). Major accomplishments have been demonstrated in each of the tasks and disseminated by various publications, including 3 US patents (two granted¹ and one filed); 14 journal papers and 24 conference papers (several more to be published); 8 overview presentations in conferences; 8 project presentations in industrial companies; and 1 MEMS packaging specific short course. Furthermore, the MEMS technical subdivision was successfully established in 1998.

Task I: Characterization of Localized Heating, Bonding and Deposition

The main goal of this task is to characterize newly developed localized heating, localized deposition, and localized bonding processes analytically and experimentally. We have been able to demonstrate several new bonding processes for MEMS packaging and/or trimming applications, including localized eutectic bonding, localized fusion bonding, localized solder bonding, localized CVD bonding, localized nano-second laser welding, localized ultrasonic bonding, and localized induction-heating and bonding processes.

Task II: Selective Encapsulation for MEMS Post-Packaging

This task is to apply the newly developed bonding processes to MEMS packaging applications. We have been able to accomplish vacuum encapsulated MEMS devices by using the localized solder bonding process, by using the RTP (Rapid Thermal Processing) bonding process, and by using the localized CVD sealing process. Furthermore, we were able to conduct accelerated tests to predict the lifetime of packaged devices, including long-term tests on vacuum encapsulated MEMS resonators. In another device packaging demonstration, we were able to develop a post-packaging pressure control system for barometric pressure sensor with the capability of internal reference vacuum control.

Task III: Massively Selective Trimming

This task aims to demonstrate frequency trimming of micro resonators. We have been able to achieve selective trimming by means of localized CVD mass deposition; by localized laser mass deposition process; and by localized heating and stressing process. These accomplishments will be detailed in this report.

^{*} In more general cases, 1/3 in wafer fabrication, 1/3 in encapsulation and 1/3 in testing

¹ Lin, Cheng, Najafi and Wise "Process for Making Microstructures and Microstructures Made Thereby," *US patent*, No. 6,232,150, May 15, 2001. Lin, Cheng, Najafi and Wise, "Microstructures," *US patent*, No. 6,436,853 August 20, 2002.

2.0 Introduction

Microelectromechanical Systems are shrinking sensors and actuators into micro- and nanometer scales while micropackaging emerges as the bottleneck for successful device commercialization. In the conventional IC (Integrated Circuit) fabrication, packaging contributes about one-third of the manufacturing cost. MEMS packaging processes have stringent requirements due to the fragile microstructures and are generally considered to be the most expensive steps in MEMS manufacturing. It has been suggested that MEMS packaging should be incorporated in the device fabrication stage as part of the micromachining process. Although this approach solves the packaging need for individual devices, it does not solve the packaging need for the microsystem. Especially, many MEMS devices are now fabricated by various foundry services and there is a tremendous need for a uniform packaging process. The MEMS post-packaging process must meet several requirements. It should not damage either pre-fabricated MEMS microstructures or microelectronics. It should be applicable to different MEMS pre-processing for various applications. It should adopt the well-developed IC packaging technology to save research and development efforts. In addition, some MEMS devices require *hermetic vacuum sealing* and some others require *low temperature packaging*. In order to accomplish these goals, several key elements are proposed: a cap to protect MEMS devices, a strong bond for hermetic sealing, wafer-level and batch processing to lower the manufacturing cost, and low temperature processing to prevent damage to MEMS devices.

This research project aimed to demonstrate a *massively parallel microassembly* based on *localized heating* and *localized bonding processes*. The innovation is to raise the bonding temperature at the bonding interface but to maintain low temperature at the wafer-level for strong bonding without affecting temperature sensitive materials or devices. These processes were able to selectively encapsulate and selectively trim MEMS devices. After this process, MEMS devices are ready for the standard packaging processes commonly used in the IC industry. Therefore, manufacturing cost can be reduced. Furthermore, the research has the potential to solve packaging issues that have hindered the progress of some MEMS devices. In addition to the technical approach, a non-technical task of establishing a new MEMS sub-division in ASME (American Society of Mechanical Engineers) was accomplished in the program.

3.0 Methods, Assumptions, and Procedures

It is well known that “*intimate contact*” and “*temperature*” are two major factors for the bonding process and bonding is the key in device packaging. “Intimate contact” puts two separated surfaces together and “temperature” provides the bonding energy. Previously, researchers have done theoretical studies on the effects of surface roughness to the anodic bonding process and it is concluded that surface imperfection affects the bonding results. Although “reflow” or “mechanical polishing” processes can improve the surface flatness, these processes are not readily applicable in most of the MEMS fabrication processes. On the temperature side, many commonly used bonding methods such as fusion and anodic bonding require high temperatures that may damage the devices and cause thermal stress problems. Unfortunately, raising the processing temperature may be inevitable to achieve good bonding strength. Previously, silicon-bonding technologies have been used in many types of MEMS devices. For example, devices like pressure sensors, micropumps, bio-medical sensors or chemical sensors require mechanical interconnectors to be bonded on the substrate. Glass has been commonly used as the bonding material by anodic bonding at a temperature of about 300~450°C. Eutectic bonding of various bonding systems and temperatures for different applications were conducted. Different types of Si-Si fusion bonding and Si-SiO₂ bonding processes at very high temperatures of over 1000°C have been demonstrated. For example, silicon fusion bonding is mostly used in silicon-on-insulator (SOI) technology such as Si-SiO₂ bonding and Si-Si bonding. These proven methods can achieve great bonding strength. Unfortunately, since the temperature requirements are high, these existing bonding processes are not suitable for the proposed MEMS post-packaging.

Figure 1 shows a microaccelerometer fabricated by Analog Devices Inc. [6] and is the illustration example in this project for MEMS post-packaging. The most fragile part on this device is the mechanical sensor at the center that is a freestanding mechanical, mass-spring microstructure. It is desirable to protect this mechanical part during the packaging and handling process. At the same time, the process temperature during the packaging procedures must be kept low to prevent damage to the microelectronics or temperature-sensitive materials on the chip. Moreover, vacuum encapsulation may be required for these microstructures in applications such as resonant accelerometers or gyroscopes. Therefore, the proposed approach must be versatile. Figure 2 shows the schematic diagram of “MEMS post-packaging by localized heating and bonding.” A “packaging cap” with properly designed micro cavity, insulation layer, microheater and micro glue layer is fabricated to encapsulate and protect the fragile MEMS structure as the zero-level MEMS post-packaging process. The wafer can be diced afterwards and packaged using well-established IC industry packaging technology. This project proposes several tasks aimed at establishing a reliable encapsulation process to protect MEMS devices after the completion of all micromachining processes, including frequency trimming. The primary vehicle for this research program is massively parallel encapsulation of microstructures, either mechanical structures or bio/chemical substances, that require physical protection during higher level packaging processes. It is noted that none of the current technologies meets this requirement [7]. The proposed method, as shown in Figure 2, will meet this requirement. The cap-substrate will be

fabricated separately and put on the MEMS devices that may have pre-fabricated microelectronics. Microheaters or other heating methods can be used to provide localized heating such that localized bonding processes can occur to seal the gap. After this wafer-level MEMS *post-packaging* process, the wafer can be diced and the well-established chip-scale packaging technology in IC industry can follow to finish the final packaging. The schemes proposed here can be conducted massively and in parallel for high volume production to reduce the manufacturing cost. In order to accomplish MEMS post-packaging procedures, specific tasks in this program were:

3.1 Task I: Characterization of Localized Heating, Bonding and Deposition

The key element of this task is to provide *localized heating* such that *localized bonding processes* can occur selectively for hermetic sealing without affecting the surrounding circuitry or temperature sensitive materials. This task concentrated on theoretical and experimental heat transfer and bonding processes to achieve optimized processing conditions. Theoretical modeling and experimental characterization, including both time domain analysis and computer simulation, were accomplished. The possible stress problems induced by localized heating were characterized in this task. Organization of this work as a separate task ensured that the results were well documented for use in CAD systems, so that the efforts here became generic for the MEMS community and were not limited to one or two isolated devices.

3.2 Task II: Selective Encapsulation for MEMS Post-Packaging

Selective encapsulation for MEMS post-packaging was conducted under this task by using the proposed method as shown in Fig. 2. The cap-substrate were fabricated separately and put on the MEMS wafer that has pre-fabricated microelectronics. Microheaters were used to provide localized heating such that localized LPCVD process can occur to seal the gap. Other means of localized heating such as laser, inductive and ultrasonic means were also investigated in the project. In addition to cap encapsulations, packaging schemes were applied to several MEMS devices for both demonstration and characterization purposes and the common devices used were comb-shape micro resonators. In addition to cap encapsulations, the packaging scheme can be applied to other applications. For example, for *MEMS optical applications* such as laser beam for bar-code-readers [8], transparent encapsulation is required. In this case, a transparent glass substrate was used as the cap material. For *MEMS microfluidics applications*, micro-to-macro connectors are required [9]. In this case, the cap substrate was designed to have large openings at the top for interconnections with macro scale pipes. For *MEMS vacuum applications*, vacuum inside the cap is required for damping control [10]. In this case, issues of reliability and lifetime of the packages were studied statistically in this project. After this wafer-level MEMS *post-packaging* process, the wafer can be diced and the well-established chip-scale packaging technology in IC industry can follow to finish the final packaging. This scheme proposed here can be conducted massively and in parallel for high volume production to reduce the manufacturing cost.

3.3 Task III: Massively Selective Trimming

In working on microelectromechanical filters [10] for wireless communications in the past, we have found that mechanical resonators have to be trimmed individually for frequency control. Unfortunately, trimming on a single device level is expensive and sometimes impractical if the device geometry is too small to be trimmed by conventional schemes. Selective CVD coating provides a unique way to massively trim individual mechanical structures. Figure 3 illustrates an example of micro trimming by a global LPCVD process [5]. LPCVD nitride is deposited onto the surface of polysilicon beams of a comb resonator [11] and the resonant frequency has been changed from 17 to 24 kHz. Unfortunately, this previous achievement of micro trimming has no control over individual devices in a regular CVD deposition process. In this project, several localized and selective trimming processes were developed, including localized CVD trimming, localized heating and stress trimming and localized laser deposition for trimming applications. As such, devices on a whole wafer can be trimmed individually and in parallel to save manufacturing cost and the same scheme can be applied to other MEMS devices.

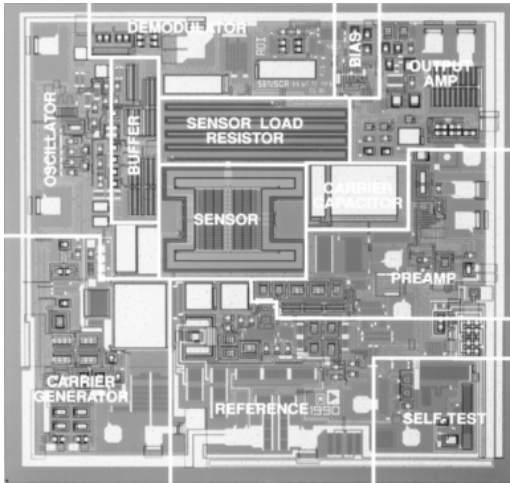


Fig. 1. A MEMS sensor with pre-fabricated microelectronics.

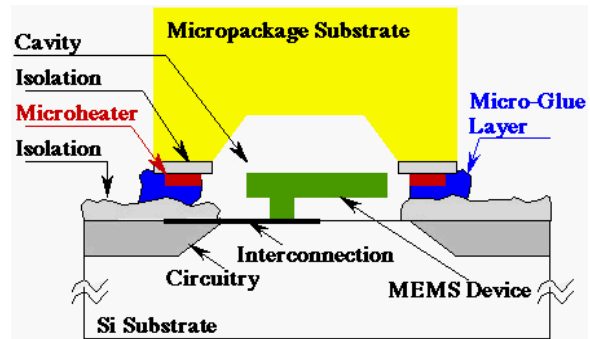


Fig. 2. Schematic diagram of MEMS post-packaging by localized sealing.

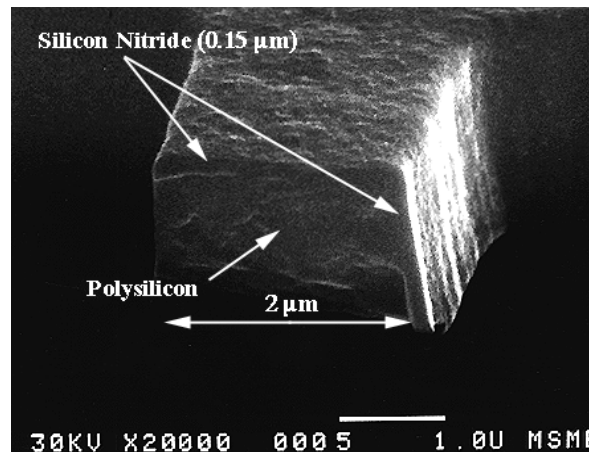


Fig. 3. MEMS post-trimming by a global deposition process.

4.0 Results and Discussion

4.1 Task I: Characterization of Localized Heating, Bonding and Deposition

In task I, we have worked on the characterization of several innovative new bonding processes for applications in MEMS packaging and trimming. These processes were applied in tasks II and III of the project and are primarily based on the concept of “localized heating and bonding”, as discussed below.

4.1.1 Localized Eutectic/Fusion Bonding Process

We have successfully demonstrated localized gold-to-silicon eutectic bonding [12,13]. The process takes only about 5 minutes in atmospheric environment. This is a dramatic reduction of time when compared with the conventional eutectic bonding process that is performed in an oven by the global heating process. Figures 4 and 5 show the global and localized gold-to-silicon eutectic bonding processes, respectively, after the bonds are forcefully broken. Non-uniformity can be clearly observed in Figure 4, where only a portion of the gold is bonded. For the case of the localized eutectic bonding test, as shown in Figure 5, the silicon is broken and attached to the gold microheater after the bond is forcefully broken. This indicates that the eutectic bond is as strong as the fracture toughness of silicon. Moreover, the bond is rather uniform in that gold and silicon has bonded together and the whole gold line has disappeared.

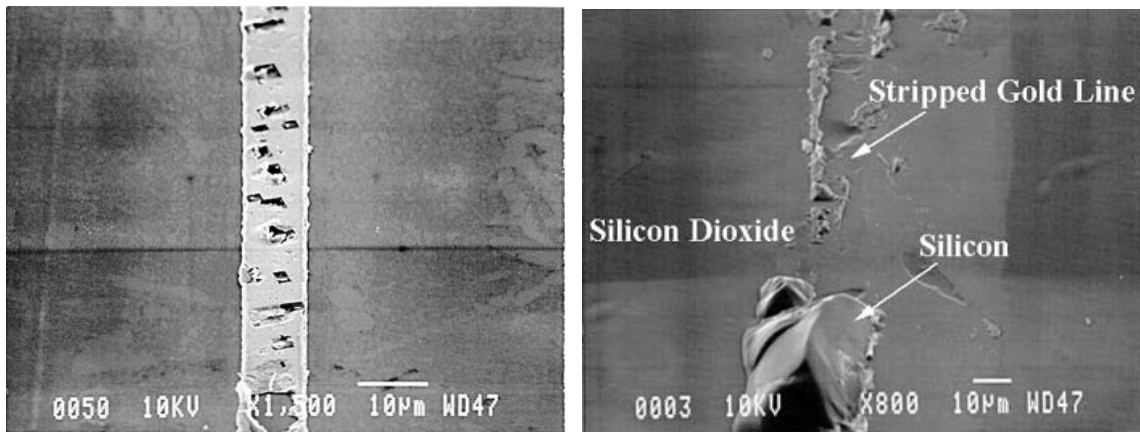


Fig. 4. Eutectic bonding by global heating. Fig. 5. Eutectic bonding by localized heating.

A localized silicon-to-glass fusion bonding process has been demonstrated in atmospheric environment. The process takes only about 5 minutes. We have broken the bonds and taken SEM microphotographs. Figures 6 and 7 show the same sample under SEM before and after dipping into HF, respectively. It reveals that the silicon-glass bond is rather strong and uniform such that the polysilicon heater has become part of the overall structure and cannot be identified before dipping into HF. Some part of the glass substrate was melted during the process due to the high local temperature. As compared to the conventional fusion bonding process that normally requires in excess of 1000°C for more than 1 hour, the localized fusion bonding process was accomplished in a very short time with excellent bonding results. As such, it has great potential as a new bonding process for MEMS fabrication and packaging applications, especially for

devices that may have pre-existing temperature-sensitive materials and can not sustain any high temperature process globally.

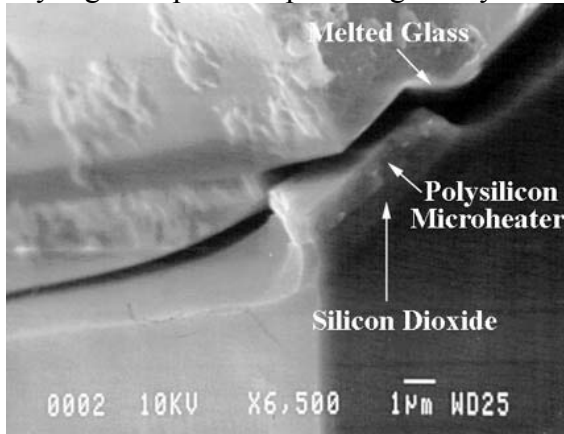


Fig. 6. Localized fusion bonding.

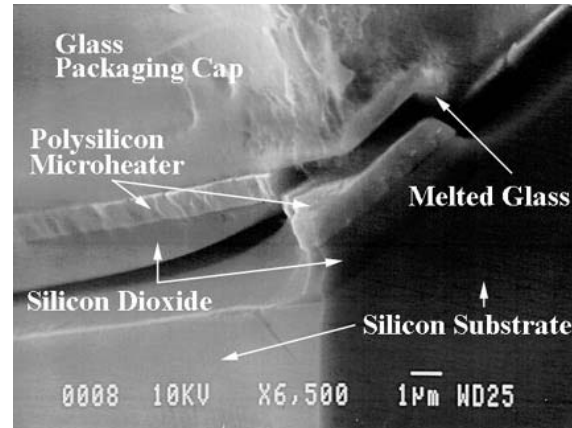


Fig. 7. Microheater shows up after HF dipping.

4.1.2 Localized PSG (Phosphorous Silicate Glass)-to-Glass Bonding Process by Using PSG as the Intermediate Layer

We have successfully demonstrated a localized PSG-to-glass fusion bonding process by using PSG as the intermediate layer [13]. The process takes only about 2 minutes in atmospheric environment while the local temperature can be as high as 1000°C. A pressure of 1 MPa is applied on top of two wafers, and a current of 10 to 70 mA (exact amount depends on the design of the microheaters and the intermediate layer) is passed through the heater. Figures 8 and 9 show the results of the PSG-to-glass bonding via the intermediate layer after breaking the silicon and glass wafers. In contrast to 4.1.1 where the resistive heating element also served as the bonding material, the significance of this new bonding system is that an intermediate layer is used as the bonding material. As such, the reaction of heating and bonding can be separated for much better process control.

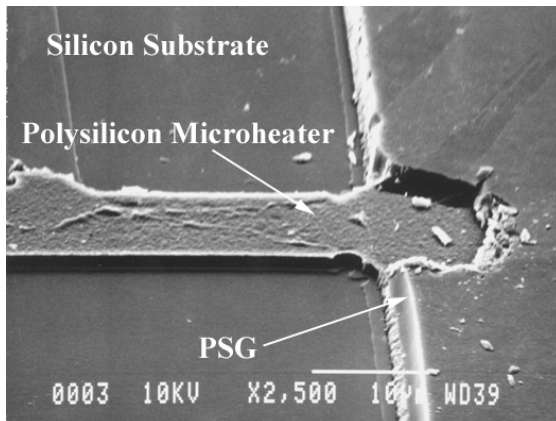


Fig 8. A SEM micrograph of the silicon substrate showing the PSG is stripped.

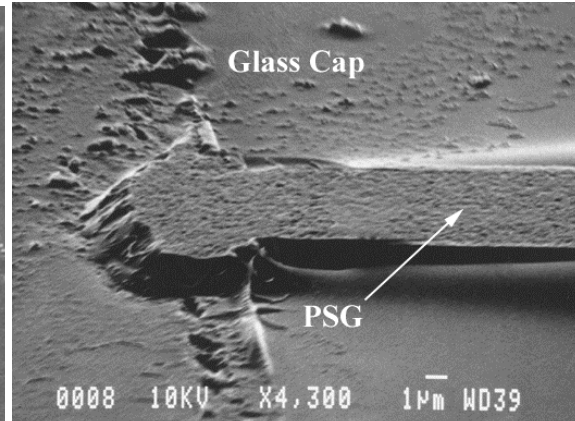


Fig. 9. A SEM micrograph of the glass cap showing PSG is bonded to the glass.

4.1.3 Localized Indium-to-Glass Bonding Process with Indium as the Intermediate Layer

In another technology advance, we were able to use metal solder as the intermediate bonding layer for packaging applications [14]. Moreover, we fabricated a dew-point sensor inside the packaged cavity in an effort to monitor the moisture inside the packaged cavity. However, we later determined that this dew point sensor was not sensitive enough to evaluate the hermeticity of the packaging, and comb-shape resonators were used in the later packages to evaluate our packaging processes. Figures 10 and 11 are the results of the Indium-to-glass bonding after breaking the silicon and glass wafers. The dew point sensor is shown in Figure 10. The interconnection line from the device to the outside contact pad presents a common problem for MEMS packaging – it creates a step-up surface roughness condition as shown in Fig. 12. Because of this, a planarization process is required for global bonding processes, such as fusion bonding and anodic bonding, to make a flat surface for bonding. The concept of localized bonding using an intermediate layer allows the bonding material to be softened or reflowed, as shown in Figure 12. Therefore, the surface roughness problem can be alleviated.

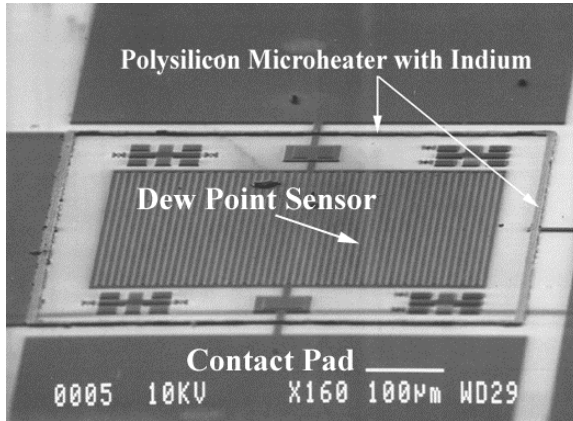


Fig. 10. A SEM micrograph of the silicon substrate after breaking the indium-glass bond.

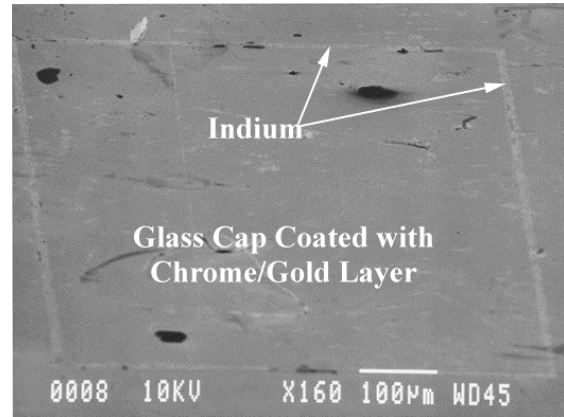


Fig. 11. A SEM micrograph of the glass cap after breaking the Indium-glass bond. Indium is uniformly attached to the glass cap.

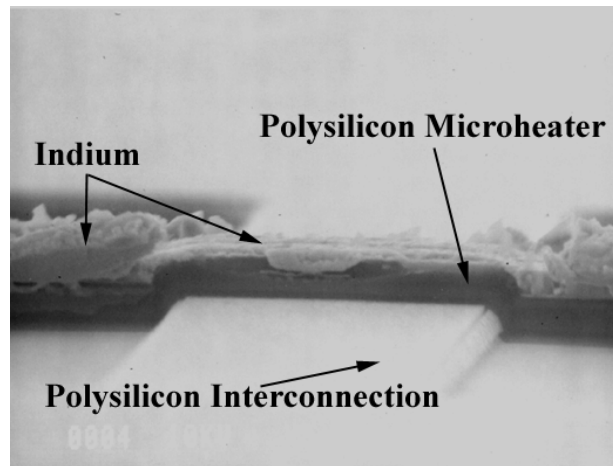


Fig. 12. Indium solder reflows after heating to seal the gap created by the interconnection.

4.1.4 Selective and Localized Hermetic Bonding using Inductive Heating

The previous sections (4.1.1, 4.1.2 & 4.1.3) are based on resistive heating. However, the process may be too tedious to put electrical current into the resistive heater individually with physical contacts. This section discusses a new heating concept based on remote, inductive heating. Fast, selective and localized hermetic wafer bonding using induction heating has been successfully demonstrated to encapsulate a water droplet [15]. This demonstrates the capability of low temperature processing at the wafer-level. Furthermore, autoclave test at 120°C, 100% humidity and 200kPa for 30 minutes was performed and no visible leakage can be found.

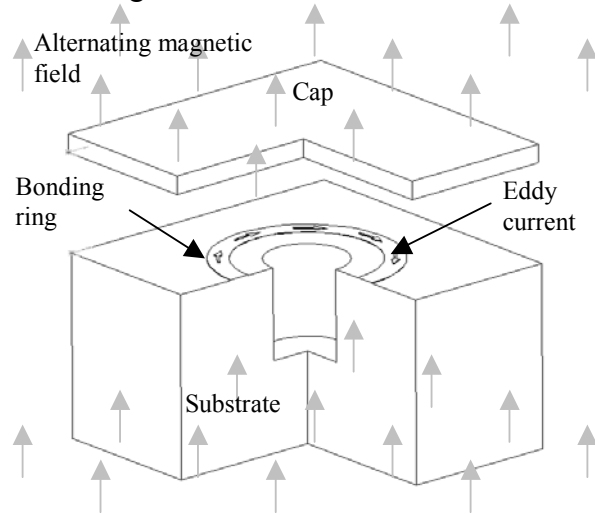


Fig. 13. Induction heating and bonding concept; using externally applied alternating magnetic field to induce eddy currents and resistive heating in a metallic bonding ring.

Figure 13 shows the idea of induction heating by placing a metallic bonding ring under an externally applied oscillating magnetic field. Induced eddy currents selectively heat the metal bonding ring, but not the substrate. The actual induction heating setup is shown in Figure 14 where the heating sample is placed in the middle of the helical coil that generates an alternating magnetic field at 10-15MHz. Induction heating can create high temperature in a short time. Figure 15 shows the measured transient temperature reached by a gold bonding ring when heated under different induction power. The rapid heating rate makes it possible to achieve bonding quickly and locally without heating the whole substrate. Transient FEM analysis of two polycarbonate substrates during a 100ms bonding cycle is shown in Figure 16. The FEM results indicate that high temperature can be reached near the bonding ring, but the heat is confined to a localized region, verifying the capability of low temperature processing at the wafer-level. As such, this scheme can be applied to massively parallel MEMS packaging applications.

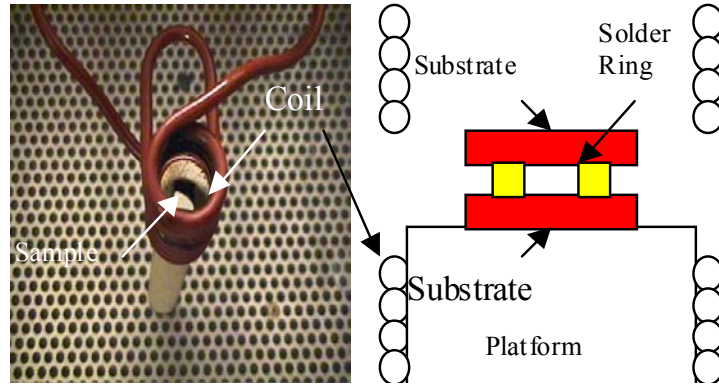


Fig. 14. Induction heating setup using an 8 turned helical coil driven between 10-15MHz.

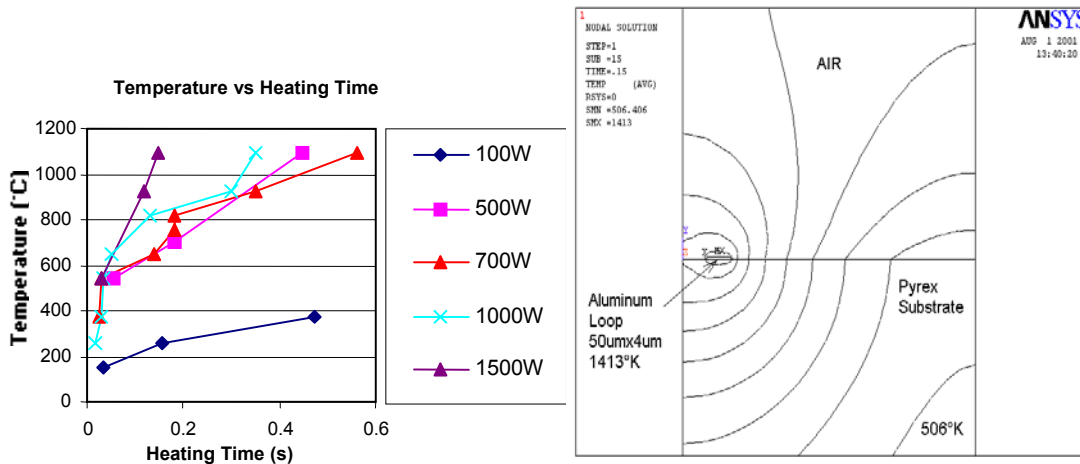


Fig. 15. (left) Measured temperature with respect to time of $4\mu\text{m}$ thick, $200\mu\text{m}$ -wide and 1mm diameter gold bonding ring under varying induction heating power. Fig. 16. (right) Temperature distribution in a 50mm wide aluminum bonding ring on Pyrex wafer heated with 1kW for 100ms.

Experimentally, induction heating can be used for hermetic bonding using a metallic solder loop as small as 1mm in diameter. Different combinations of solder and substrate have been tested, including chrome, gold indium and aluminum as solders and silicon, SOI, and Pyrex glass as substrates. One combination tested is a Pyrex wafer patterned with a 1mm diameter bonding ring made from 20nm of Cr and $4\mu\text{m}$ of Au, bonded to another Pyrex wafer coated with 20nm of Cr. The bonding was performed using 1500W applied for 3 seconds. A close up view of the bonding interface is shown in Figure 17. The metallic solder ring has heated and bonded with the glass substrate. A short distance away from the metallic ring, the two glass substrates got hot enough to bond directly with each other. Figure 18 shows a 1mm bonding loop that has been forcefully broken apart. Glass from one substrate has been torn off and is firmly attached to the second substrate, suggesting the bond strength is very high, perhaps comparable to the bulk strength of the Pyrex. Two different methods were used to test the bonded package for hermetic sealing. The bonded loop was first wetted with isopropyl alcohol and ink, and no ink could be observed going inside the loop. The bonded loop was then

inserted into a 120°C steam pressure chamber for 30 minutes. Again, no visible leakage or fogging could be observed.

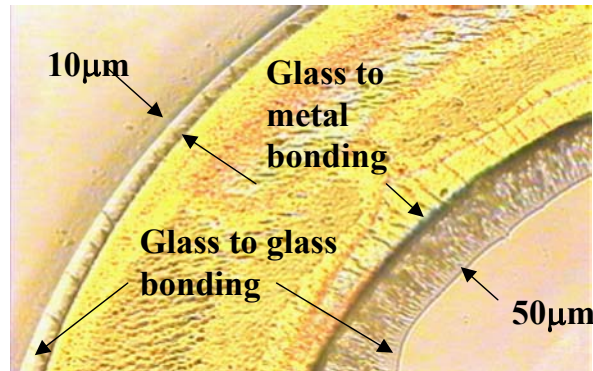


Fig. 17. Pyrex to Pyrex bonding using 1mm diameter, 200mm wide, 4mm thick gold solder ring with 20nm of Cr adhesion layer on both Pyrex surfaces.

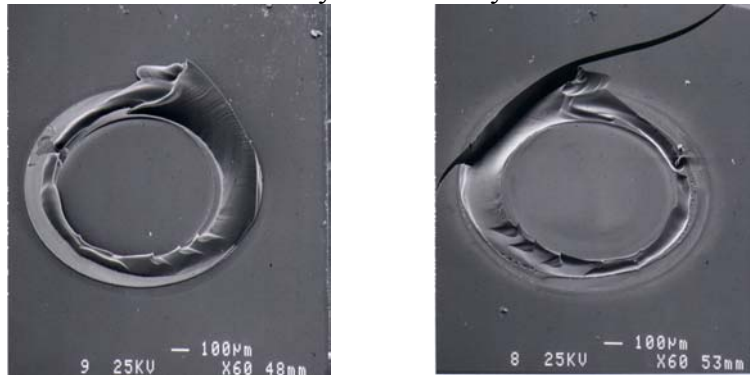


Fig. 18. Two halves of a forcefully broken cavity bonded with 1.5kw for 3 seconds.

4.1.5 MEMS Post-packaging by Nanosecond Laser Technology

Another possible way to provide a remote source for localized heating is to use laser. An Nd: YAG Surelit II laser with pulse duration of 4-6ns and a wavelength of 355nm was used to form glass-to-silicon bonding with an intermediate layer of indium [16]. The purpose of nanosecond laser heating is for rapid and localized heating profile. The experimental setup is shown in Figure 19. A 5µm-thick indium layer is deposited on the silicon substrate. A glass (7740 from Dow Corning) substrate is transparent to laser light with a wavelength of 355nm, such that it does not absorb laser irradiation when the laser light goes through it, while the indium layer does. A mask consisting of reflective material, which is plain white paper in the current investigation, is put on the glass layer. The material corresponding to the bonding area is removed from the mask. This allows the laser beam to reach the bonding area. Indium in the spot of laser irradiation melts and achieves chemical bond with glass at the interface. Multiple laser shots at one spot allow more materials to melt and provide more reaction time, which leads to stronger bonding results.

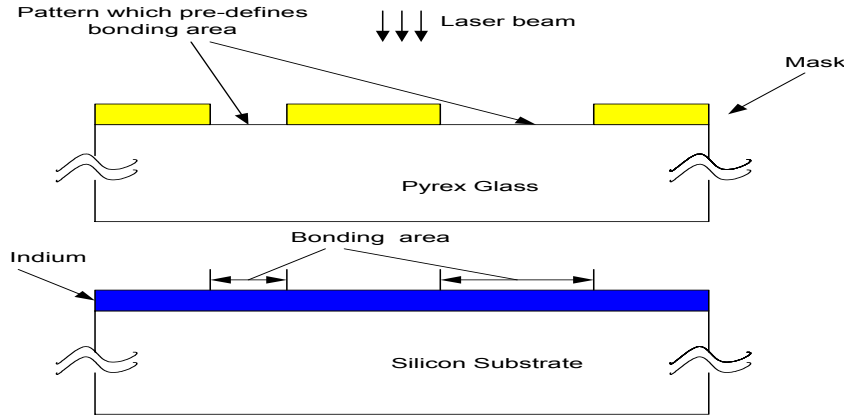


Fig. 19. The experimental set up of glass-to-silicon bonding with an intermediate layer of indium and a built-in mask

An optimal bonding region was obtained, based on experimental results, to choose the laser output power and number of shots at one spot, with other laser-welding parameters fixed. Several observations are concluded: (1) very high laser output power may damage the bonding interface and lead to the failure of bonding; (2) very low laser output power fails to generate enough energy to form a strong bond; (3) too many shots at one spot may destroy the bond which has already been formed previously; (4) too few shots at one spot does not form a good bond. In Figure 20, an example of bonded area of 1 mm in diameter is shown after 10 shots of a laser beam with 10mj energy. Then, the glass-to-indium bond is forcefully broken to examine the bonding interface. From Figure 21, it can be seen that the bond is broken in the indium layer. This indicates that bonding strength is similar to the yielding strength of indium at 2.6MPa. This example demonstrates that a nanosecond pulsed laser can be used to form strong bonding. In Figure 22, the result is shown corresponding to a round pattern on the mask. These indicate that the laser light does not go beyond the bonding area. The first result implies that the laser-beam size can be larger than the characteristic length of the bonding area, while the second indicates that it can be smaller.

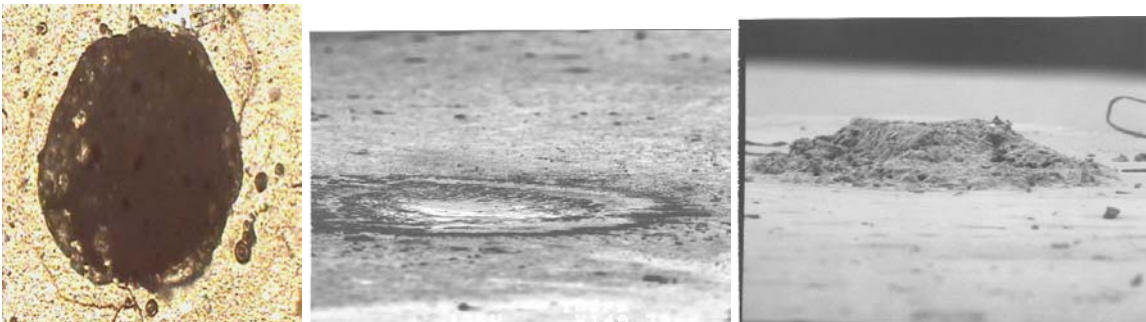


Fig. 20. (left) A top view of the laser welding result where glass-to-indium bond is formed. The diameter of the spot is 1mm with 10 shots of laser power of 10 mJ. Fig. 21. (center and right) A side view (SEM) of the bonding spot after we break the glass-to-indium bond: (center) on the glass layer, (right) on the indium layer.

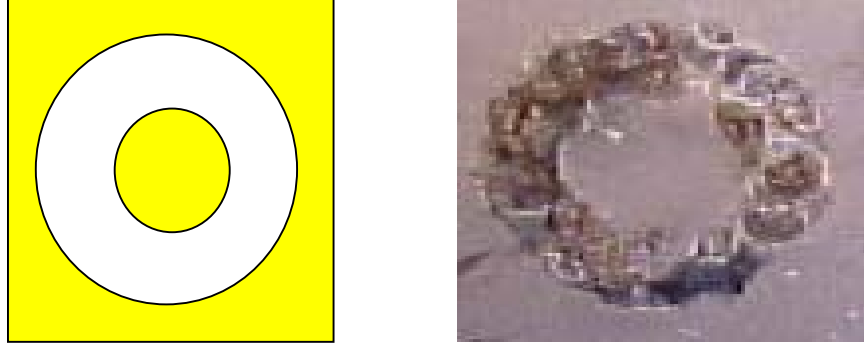


Fig. 22. A top view of the bonding result using a built-in mask after random laser shots on the mask: (left) a ring-shape pattern as the mask with the outer diameter of 4 mm and inner diameter of 1.8 mm, (right) bonding result with the bonding area of the same size as that of the pattern. The laser-beam size is 1 mm in diameter, smaller than the radial length of the ring pattern of 1.1 mm.

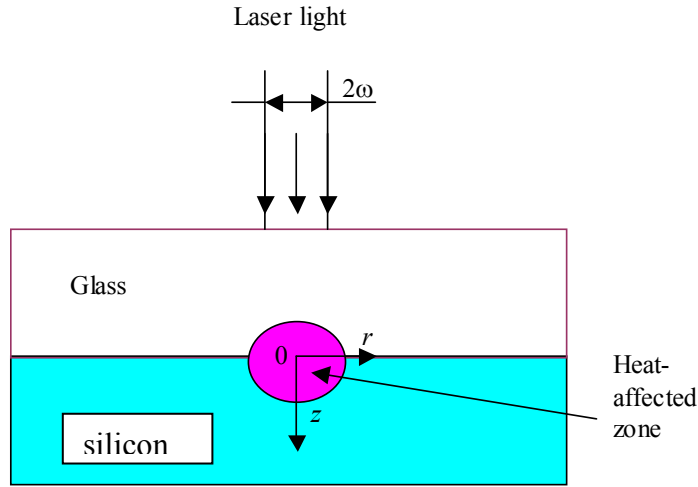


Fig. 23. Schematic representation of the laser welding process of the system.

The nanosecond laser-welding system is shown in Figure 23. A glass substrate is placed on top of the silicon substrate that may have a layer of bonding material, such as indium. Glass is transparent to laser and does not absorb laser energy and either silicon or indium will absorb laser energy and generate heat. Therefore, if enough laser energy is absorbed, a chemical bond may form at the interface. Energy from the laser source may be strong enough to create evaporation and if the evaporation is significant, the outgoing indium vapor may push the glass surface away from that of indium by means of thermal shock. This situation is not desirable in the bonding process since the bonding system may lose intimate contact and fail to form the bond. Therefore, it is important to conduct numerical simulation to characterize the proper temperature distributions for bonding.

A two-dimensional mathematical model is adopted to determine the heating zone in the bonding system. Heat conduction along both the radial direction and axial direction is considered. The modeling of heat transfer in the substrate irradiated by a laser pulse of short duration has been studied recently. Instead of the Fourier heat diffusion model, a hyperbolic heat conduction, vibrational cooling model, and equations of phonon radiative

transfer (EPRT) based on Boltzmann transport theory have been developed. During the time of a nanosecond or millisecond laser pulse, electrons that absorb the photons from laser light experience many collisions, both among themselves and with lattice phonons. Then energy absorbed by an electron will be immediately redistributed and passed on to the lattice. The electromagnetic energy from laser light can be viewed as being instantaneously converted into heat at the location of absorption. Therefore, it is reasonable to assume a local thermodynamic equilibrium state, and the classical concept of temperature and thermal properties can be defined and used in this study.

The absorption penetration depth on the substrate layer is of the order of 10 nm. We treat it as a volumetric heating source. The incident laser power intensity distribution is considered as Gaussian, that is:

$$I(r, z, t) = (1 - R) \frac{2P}{\pi\omega^2} \exp\left(-\frac{2r^2}{\omega^2}\right) \exp(-az) * H(t), \quad (4.1)$$

where R is reflectivity, P is the laser output power, ω is the radius of the incident laser beam size, and $H(t)$ represents the time variation of the pulse and has the form of a unit step input:

$$H(t) = \begin{cases} 1 & \text{as } 1 < t < t_p, \\ 0 & \text{as } t > t_p. \end{cases} \quad (4.2)$$

The governing equation in the substrate during the pulse duration is:

$$\rho C \frac{\partial T}{\partial \tau} = k \left[\frac{\partial^2 T}{\partial r^2} + \frac{1}{r} \frac{\partial T}{\partial r} + \frac{\partial^2 T}{\partial z^2} + I(r, z, t) \right], \quad (4.3)$$

where ρ denotes mass density, C is specific heat, T stands for temperature, k denotes heat conduction coefficient, r represents radial coordinate, and z is axial coordinate. ρ , C and k will change with temperature.

The governing equation in the glass during the pulse duration is:

$$\rho C \frac{\partial T}{\partial \tau} = k \left[\frac{\partial^2 T}{\partial r^2} + \frac{1}{r} \frac{\partial T}{\partial r} + \frac{\partial^2 T}{\partial z^2} \right]. \quad (4.4)$$

The boundary condition at the interface is

$$\left(k \frac{\partial T}{\partial x} \right)_{\text{glass}} = \left(k \frac{\partial T}{\partial x} \right)_{\text{substrate}}. \quad (4.5)$$

We assume that at $t=0$, the temperature of the whole structure is uniform and is equal to the ambient temperature, 300 K.

$$T(r, z, t = 0) = 300 \text{ K} \quad (4.6)$$

It is assumed that there is no heat loss at the upper surface of the glass layer and lower surface of the substrate layer by radiation, convection, and conduction.

$$\frac{\partial T}{\partial z} = 0 \quad (4.7)$$

At the center $r = 0$, because of the axisymmetry of temperature distribution, we have

$$\frac{\partial T}{\partial r} = 0. \quad (4.8)$$

At the place $r \rightarrow \infty$, the temperature is the same as the ambient temperature, 300 K, that is,

$$T(r \rightarrow \infty, z, t) = 300 \text{ K} . \quad (4.9)$$

After a laser pulse is applied, the governing equation in both the glass and substrate layers is the same:

$$\rho C \frac{\partial T}{\partial \tau} = k \left[\frac{\partial^2 T}{\partial r^2} + \frac{1}{r} \frac{\partial T}{\partial r} + \frac{\partial^2 T}{\partial z^2} \right]. \quad (4.10)$$

The boundary conditions (4.5), (4.7)-(4.9) are still valid but equation (4.6) cannot be used as the initial condition here. The initial temperature distribution in this case is the temperature just after one pulse of laser duration. The laser fluence is set as $7 \times 10^{12} \text{ J/(m}^2 \text{ sec)}$. Two simulation (software ANSYS 5.5) results are given in Figure 24 to illustrate heat-affected zones and temperature distribution during the bonding process for the combination of glass, indium and silicon under the irradiation of a nanosecond pulsed laser. Clearly, localized heating is achieved because the very short-term laser pulse provides heating in a very limited area. Therefore, this method provides another technique of remote heating for localized bonding, as compared to the resistive heating introduced in sections 4.1.1, 4.1.2 and 4.1.3.

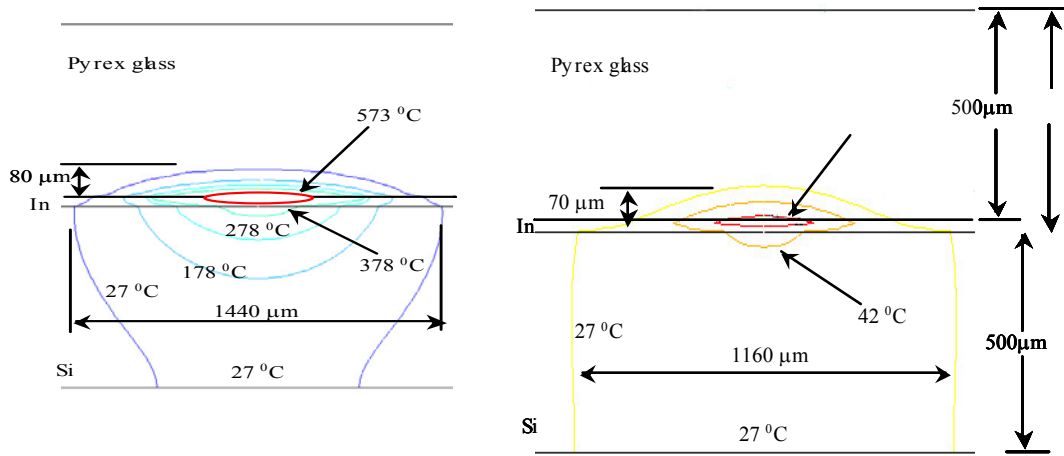


Fig. 24. Two simulation (software ANSYS 5.5) results of heat-affected zones on the cross section after the indium layer absorbs energy under irradiation of laser beam with diameter of 1mm and output energy of 22 mJ: (left) the result after 1 ms, (right) the result after 1 second.

4.1.6 Localized Ultrasonic Bonding Process

This process utilizes purely mechanical vibration energy and enables low temperature bonding between similar or dissimilar materials without pre-cleaning of the bonding surfaces. As such, ultrasonic bonding can be broadly applied not only for electrical interconnection, but also for hermetic MEMS sealing and packaging, especially where temperature limitation is a critical issue [17]. Figures 25 and 26 show the schematic of the bonding setup and results. Ultrasonic power, applied vertical load and operation time are three control parameters to achieve hermetic sealing for MEMS application. Two different bonding equipment setups were used in this experiment and it was concluded that the lateral vibration setup (as shown in Figure 25) gives better bonding results for MEMS level packaging than the vertical vibration setup. Figure 26

shows the hermetic testing results of two sealing rings. The top one is a failed bonding ring for comparison purpose as colored water enters inside the cavity. The bottom sealing ring prevents the penetration of liquid and is a successful result.

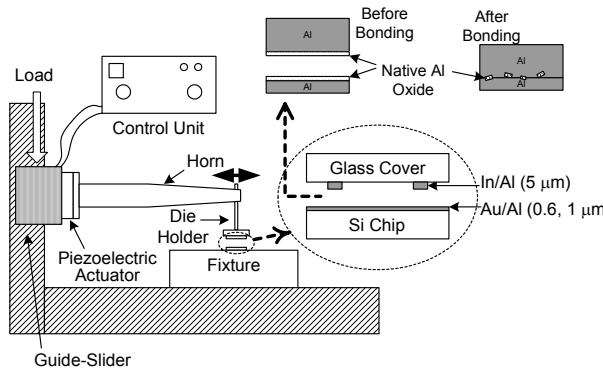


Fig. 25. Schematic setup of the process.

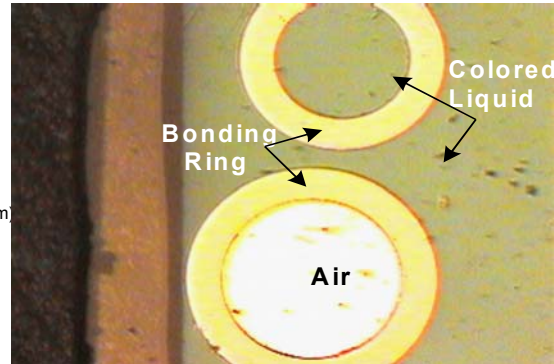


Fig. 26. Ultrasonic hermetic sealing results.

4.1.7 Residual Stress Analysis of Thermal Bonding Processes for MEMS Packaging

One of the concerns for localized heating and bonding is the local residual stress generated during the bonding process. In order to investigate this effect, finite element analysis is used to predict the stress level and compare with experimental results [18]. Figure 27 is the schematic diagram of the bonding system under investigation, including a silicon substrate, a glass cap and a bonding aluminum strip with a thickness of $3\mu\text{m}$. The aluminum-to-glass bonding system is used in these simulations, because it gives the best sealing results, to be shown in Section 4.2. Figure 28 shows the mask design for the aluminum to be deposited onto the glass substrate. To determine the effects of width when bonding, the aluminum will be deposited with varying widths of $30\mu\text{m}$, $50\mu\text{m}$, $100\mu\text{m}$, and $150\mu\text{m}$. Once the aluminum is bonded to the silicon substrate, measurements will be taken using a Raman Spectroscope to measure the residual stress. The cross-section line in Figure 28 shows where the FEM ANSYS analysis is simulated. The ANSYS FEM computer simulation used is two-dimensional; therefore the length to width ratio of the Aluminum strip in the experimental analysis is substantially large to enable accurate comparison between the experimental and analytical techniques.

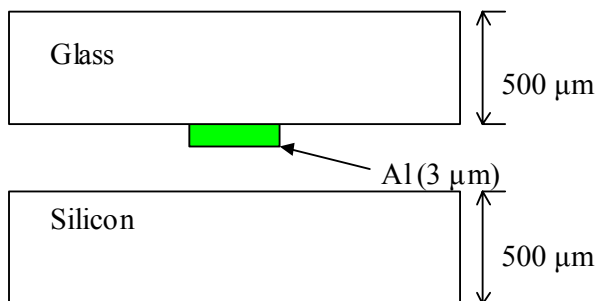


Fig. 27. (left) Schematic diagram of the bonding system analyzed

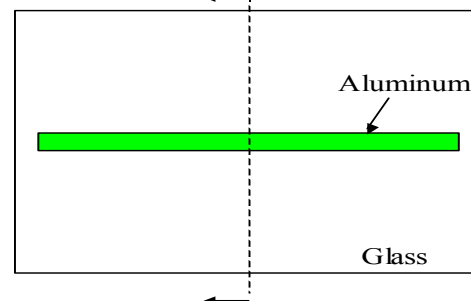


Fig. 28. (right) Mask design.

Figure 29 is a picture taken of a quartz-aluminum-silicon bond. Fracture is observed in this picture, which proves the need for residual stress analysis in different materials in order to correctly predict when fracture will or will not occur. Figure 30 is

the results of the thermal simulation done on ANSYS. This predicts how long it will take for the entire system to cool down and produces input for the structural part of the analysis in ANSYS. Figure 31 shows the residual stress analysis of the Pyrex glass-aluminum-silicon system using temperature dependent properties only. The non-linear stress-strain curve for aluminum is not input into this particular analysis, which predicts the residual stresses to exceed the yield point and even the ultimate stress point. Figure 32 shows the residual stress analysis when the non-linear stress-strain curve for aluminum is input into the analysis, predicting residual stresses below the yield point. These results are dramatically different than those produced by the other analysis, showing the need for such a precise analysis. Furthermore, the simulation and experimental results suggest that the quartz-aluminum-silicon bonding system may create residual stress that is larger than the yielding stress of quartz causing fracture of the substrate. On the other hand, the pyrex glass-aluminum-silicon bonding system can generate acceptable stress that is lower than the yielding stress of glass.

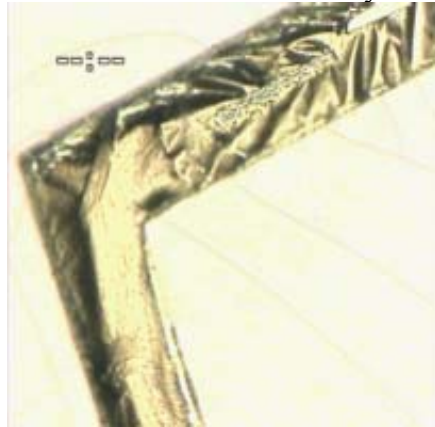


Fig. 29. Quartz bonded to silicon with an aluminum bonding strip

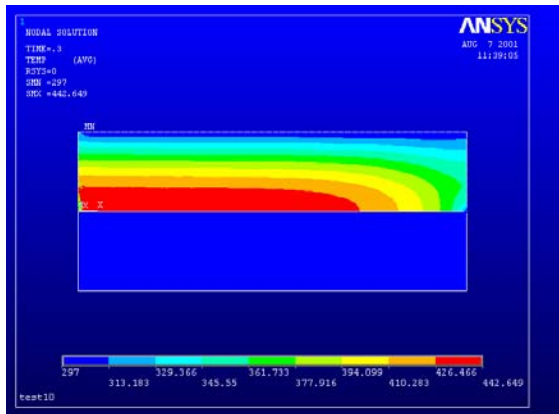


Fig. 30. (left) FEM thermal analysis of the cooling after global heating (at .3 seconds).

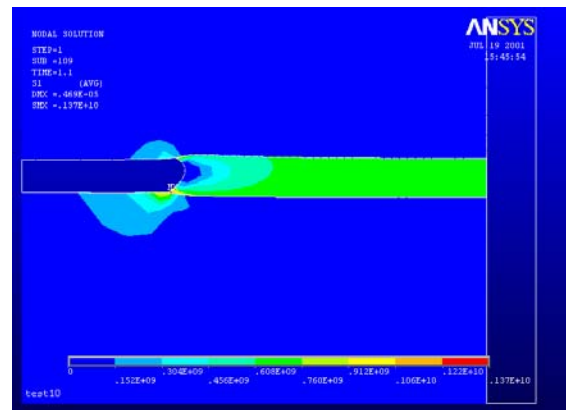


Fig. 31. (right) FEM residual stress analysis using temperature dependent properties for all materials.

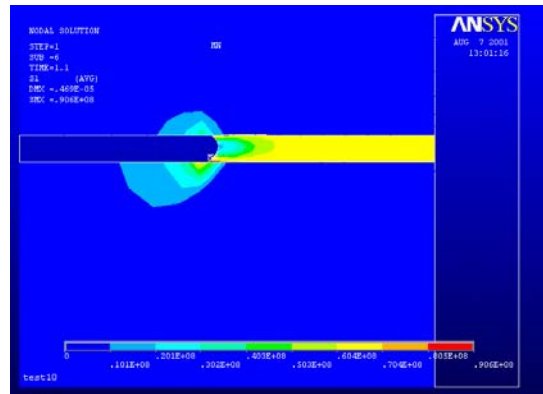


Fig. 32. FEM residual stress analysis including non-linear stress-strain properties for aluminum.

4.2 Task II: Selective Encapsulation for MEMS Post-Packaging

Task II applies the bonding results from task I for device packaging applications. The important results in this task are the demonstrations of vacuum packaging and post-packaging technologies based on localized aluminum/silicon-to-glass bonding, localized CVD bonding and Rapid Thermal Processing (RTP) wafer bonding. Furthermore, accelerated tests in harsh environment (130°C, 2.7atm and 100%RH) were performed to evaluate the lifetime of the MEMS packages.

4.2.1 Vacuum Packaging Technology Using Localized Aluminum/Silicon-to-Glass Bonding

The localized resistive heating and bonding method, as described in the previous section, is used here for device packaging demonstrations. The first thing we have noticed was the indium used in section 4.1.2 was a rather soft material and the bonding strength was too weak for packaging applications. Localized aluminum-glass and aluminum/silicon-glass bonds were demonstrated for the first time in this project by using micro resistors made of phosphorus-doped polysilicon resulting in a bonding strength that was very strong for packaging, including vacuum packaging applications. At the interface of aluminum and glass, the formation of bonds takes place in less than 3 minutes. Several important experimental results were obtained. 1) The activation energy of the localized aluminum-glass and aluminum/silicon-glass system is characterized as 1 eV and 1.5 eV, respectively. 2) It appears that the bonding strength of the two localized bonds can reach the fracture toughness of the glass substrate. 3) Adding silicon into the aluminum-glass system helps the formation of silicon and aluminum oxide at high temperature and speeds up the bonding process.

Metal solder joints have been utilized in IC (Integrated Circuit) and MEMS (Microelectromechanical Systems) assembly for many years. They provide better electrical properties and hermeticity than other materials such as ceramic or epoxy. Previously, aluminum has been shown to react with amorphous oxide, vitreous silica, and thermal oxide and cause breakdown phenomena. Being a CMOS (Complementary Metal-Oxide-Silicon) compatible material, aluminum has the potential to become an excellent material for jointing applications in microsystems. Pyrex glass substrates (7740 from Dow Corning) are used in both bonding tests and pressed on top of the silicon substrates. The high bonding temperature is provided by means of localized heating via the lineshape microheaters. The temperature on the resistive heater is measured by monitoring the resistivity changes of the microheater and by assuming a linear dependence of resistivity changes with respect to temperature. According to a two-dimensional, cross-sectional heat transfer simulation by using FEA (Finite Element Analysis), the temperature on aluminum is about 90% of the temperature on the microheaters due to the heat conduction loss to the insulation layers.

The localized aluminum-glass bonding process finished in 3 minutes by passing an input current of 50 mA to the microheater that generated a bonding temperature of about 775°C. After the bond is forcefully broken, glass debris can be found on the silicon substrate as shown in Figure 33(a). On other hand, some of the aluminum structure is detached from the silicon substrate and attached to the Pyrex glass, as observed in Figure 33(b). This demonstrates that the aluminum-glass bond is comparable to the adhesion force of aluminum to the underneath oxide and the bonding strength reaches the fracture

toughness of the glass substrate. Moreover, the uniformity of bonding is excellent as evidenced by Figure 33, where an area of 500 x 500 μm is encompassed by the aluminum bonding lines and the complete reflection of those bonding lines can be observed on the glass substrate. Very similar bonding characteristics can be found in the aluminum/silicon-glass bonding systems with a major observable difference that the broken interface generally happens at the microheater and its underneath thermal oxide layer.

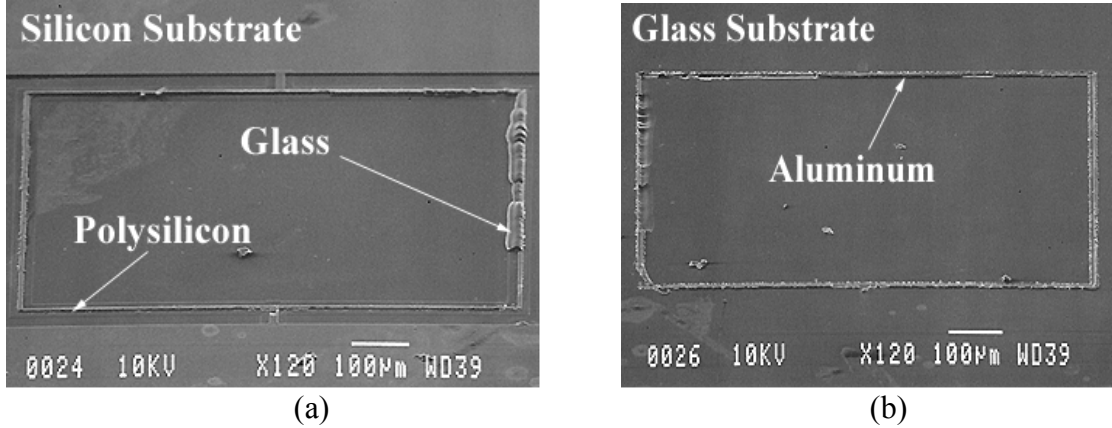


Fig. 33. Localized aluminum-glass bond after breaking the bonding interface. (a) part of glass is attached to the silicon substrate. (b) part of aluminum is attached to the glass substrate.

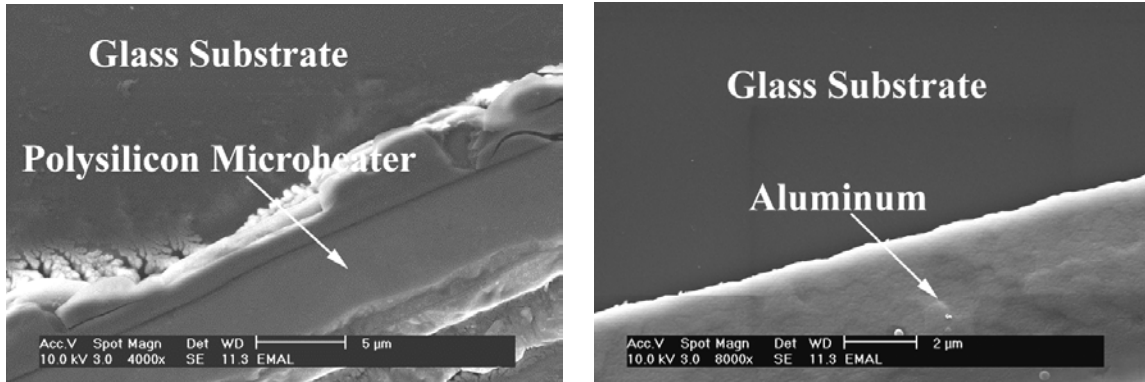


Fig. 34. Enlarged views of localized bonding results. (left) (a) aluminum/silicon-glass bond, (right) (b) aluminum-glass bond.

Figure 34(b) is an enlarged view of Figure 33(b) showing the aluminum line is attached to the glass substrate. Figure 34(a) is the comparative results from the aluminum/silicon-glass bonding system showing that the whole polysilicon microheater is transferred onto the glass substrate. This indicates that aluminum/silicon-glass bond provides a stronger bonding force between the aluminum/silicon and glass interface. The bonding mechanisms of aluminum-glass and aluminum/silicon-glass systems are examined by measuring the activation energy (E_a) in the temperature regions above the eutectic point, 577°C, of the silicon-aluminum alloy. The interface bonding reaction can be described by an Arrhenius relationship, $\ln(t) = E_a/K^*(1/T) + C$, where C is a constant and E_a is found to be 1.0 eV and 1.5 eV for the aluminum-glass and aluminum/silicon-

glass systems, respectively. The activation energy of the localized aluminum-glass bond is very close to the reports by Prabripataloong et al. for the activation energy of aluminum-vitreous glass (1.1 eV) and by Brendel et al. for the reaction of aluminum-a-SiO_x (0.98 eV). Both of them suggested that aluminum atoms would replace the silicon atoms to form aluminum oxide and pure silicon.

In order to examine the bonding mechanisms in the localized aluminum-glass bonding experiments, the sample in Figure 34(b) is put into the type-A aluminum etchant for 10 minutes to remove aluminum. The result is shown in Figure 35. A porous layer on top of the glass substrate is observed with all the aluminum removed. The sample is then dipped into tetramethyl ammonium hydroxide (TMAH) solution for 20 minutes to remove silicon precipitate. Figure 36 is the etching result and the remaining material is believed to be aluminum oxide. A similar phenomenon is also found in the aluminum/silicon-glass bond. These post-bonding examinations strongly suggest that the aluminum-glass and aluminum/silicon-glass bonds depend on the formation of aluminum oxide and silicon precipitate.

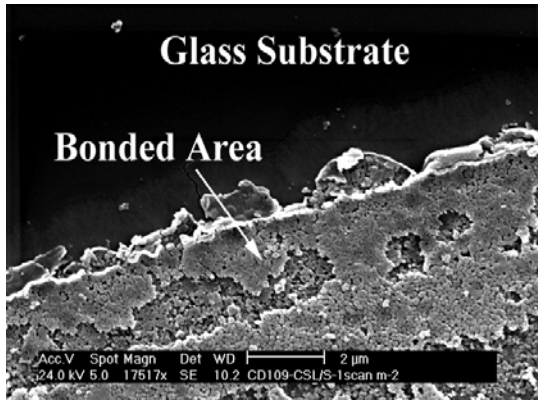


Fig. 35. Bonding interface after type-A aluminum etching.

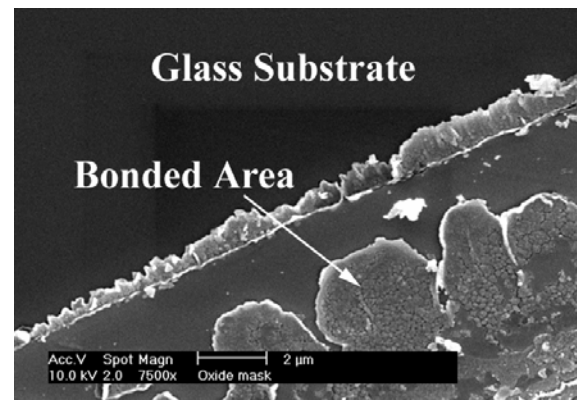


Fig. 36. Bonding interface after TMAH etching.

A vacuum package based on localized aluminum/silicon-to-glass bonding has been successfully demonstrated. With 3.4 watt heating power, ~ 0.2 MPa applied contact pressure, and 90 minutes wait time before bonding, vacuum encapsulation at 25mtorr can be achieved. Folded-beam comb drive μ -resonators are encapsulated and used as pressure monitors. Long-term testing of un-annealed vacuum-packaged μ -resonators with a Q of 2500 has demonstrated stable operation after 20 weeks. A μ -resonator with Q of ~ 9600 has been vacuum encapsulated and shown to be stable after 7 weeks [19].

The vacuum packaging presented here is based on the hermetic packaging technology using a localized aluminum/silicon-to-glass solder bonding technique reported previously. Built-in folded-beam comb drive μ -resonators are used to monitor the pressure of the package. Figure 37 shows the fabrication process of the package and resonators. Thermal oxide (2 μ m) and LPCVD Si₃N₄ (3000Å) are first deposited on a silicon substrate for electrical insulation followed by the deposition of 3000Å LPCVD polysilicon. This polysilicon is used as both the ground plane and the electrical interconnect to the μ -resonators as shown in Figure 37(a). Figure 37(b) shows a 2 μ m LPCVD SiO₂ layer that is deposited and patterned as a sacrificial layer for the fabrication of polysilicon μ -resonators using a standard surface micromachining process. A 2 μ m-

thick phosphorus-doped polysilicon is used for both the structural layer of micro resonators and the on-chip microheaters. This layer is formed over the sacrificial oxide in two steps to achieve a uniform doping profile. The resonators are separated from the heater by a short distance to prevent their exposure to the high heater temperature, as shown in Figure 37(c). This concludes the fabrication of μ -resonators.

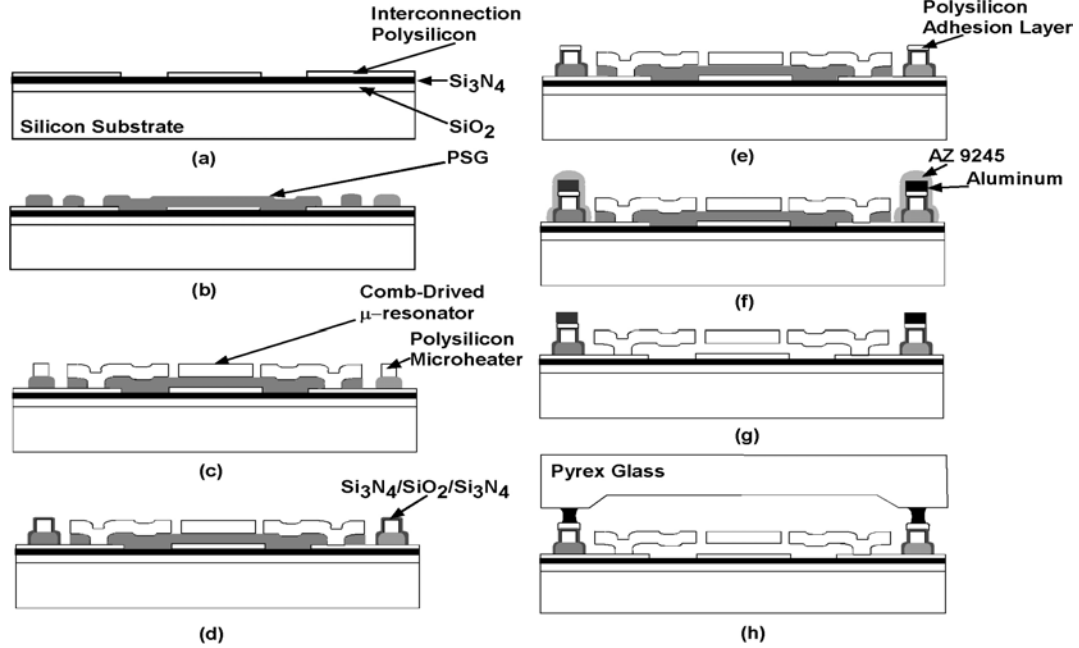


Fig. 37. Fabrication process flow of vacuum encapsulation using localized aluminum/silicon-to-glass bonding.

In order to prevent the current supplied to the microheater from leaking into the aluminum solder during bonding, an LPCVD Si_3N_4 (750 Å)/ SiO_2 (1000 Å)/ Si_3N_4 (750 Å) sandwich layer is grown and patterned on top of the microheater as shown in Figure 37(d). Figures 37(e) and (f) show the aluminum (2.5 μm) and polysilicon (5000Å) bonding materials that are deposited and patterned. The sacrificial release is the final step to form freestanding μ -resonators. Figure 37(f) also shows a thick AZ 9245 photoresist is applied to cover aluminum/silicon-to-glass bonding system to ensure that the system withstands the attack from concentrated hydrofluoric acid. After 20 minutes of sacrificial release in concentrated HF, the system as shown in Figure 37(g) is ready for vacuum packaging. Figures 38 and 39 show SEM photos of a number of released μ -resonators surrounded by a 30 μm wide microheater with aluminum/silicon bonding layer on top. A Pyrex glass cap with a 10 μm deep recess is then placed on top with an applied pressure of ~ 0.2 MPa under a 25mtorr vacuum, and the heater is heated using 3.4 watts input power (exact amount depends on the design of the micro-heaters) for 10 minutes to complete the vacuum packaging process as shown in Figure 37(h).

To evaluate the integrity of the resonators packaged in this manner, the glass cap is forcefully broken and removed from the substrate. It is observed that no damage is found on the μ -resonator and a part of the microheater is stripped away as shown in Figure 40, demonstrating that a strong and uniform bond can be achieved without detrimental effects on the encapsulated device. Outgassing from the glass and gas resident inside the cavity

are two major factors that should be minimized in order to achieve a low pressure environment in all vacuum based encapsulation processes.

During the bonding and encapsulation process, outgassing from the glass capsule could degrade the vacuum quality of the package. In this encapsulation process, the volume of cavity formed by the recessed Pyrex glass cap and the device substrate, as shown in Figure 40, is about 1.2×10^{-8} liter. Any outgassing would result in a drastic increase of pressure in such a small volume. Two possible outgassing mechanisms could happen during the fabrication of vacuum packages: 1) desorption of moisture or gases absorbed on the glass surface, and 2) out-diffusion of gases which are resident in the glass. Desorption of moisture or gases can be easily eliminated by baking the glass and device substrates at a temperature above 150°C in a vacuum oven for several hours before bonding. In the case of out-diffusion of gases, the amount of gas out-diffusion is determined by the solubility difference of gases in the glass at different temperature and pressure environments. Since the glass cap is heated during the bonding process, out-diffusion of gases from glass will occur and becomes the major factor affecting the vacuum level of the sealed cavity.

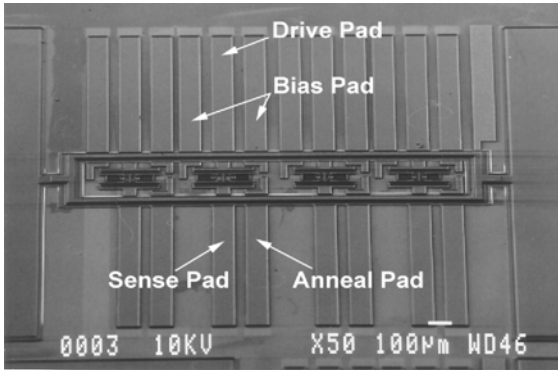


Fig. 38. SEM microphoto of folded-beam μ -resonators.

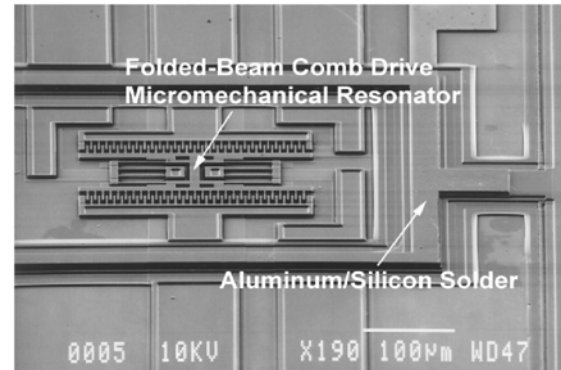


Fig. 39. Enlarged view of folded-beam μ -resonators.

A two-step pretreatment of Pyrex glass can potentially reduce the influence of gas out-diffusion. A recessed glass cap is first baked under 25 mtorr and 300°C for 1 hour, and is then coated with 3000\AA Ti/ 1000\AA Au layers on the recessed surface. Vacuum baking can reduce the total amount of gases trapped inside the glass and metal coating can provide a good diffusion barrier to gas atoms. Furthermore, Ti is a good getter material for common gases that will further reduce the amount of trapped gases inside the package and out-gassing during the bonding process. Figure 41 shows the Q of μ -resonators ($\sim 103\text{kHz}$ resonant frequency) encapsulated by glass caps with or without pretreatment and with Ti/Au layer on the recessed surface of glass. Since the Ti/Au layer effectively prevents outgassing from the glass cap during bonding, the quality factor improvement from 25 to 500 is observed.

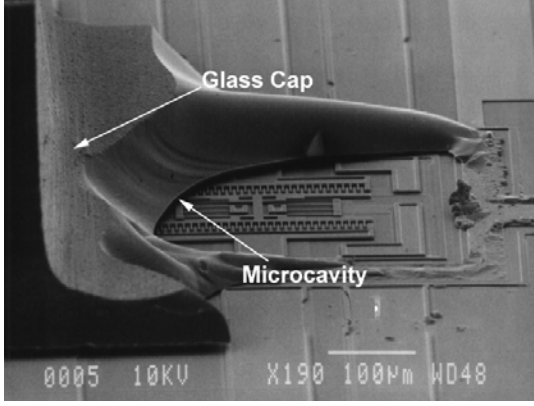


Fig. 40. The SEM photograph of encapsulated μ -resonators after the glass cap is forcefully broken away.

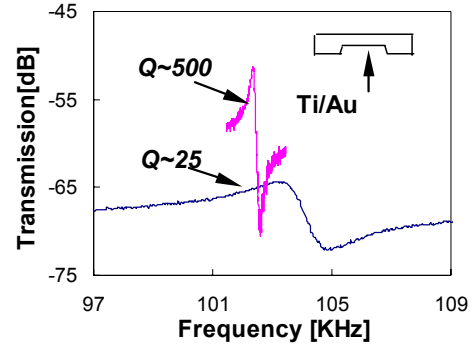


Fig. 41. The frequency spectrum of glass encapsulated μ -resonator with 90 mins. wait time in vacuum ($Q=2500$).

In the final vacuum encapsulation process, the whole packaging system is placed inside a vacuum chamber and the aluminum/silicon solder is heated up locally to initiate the bonding. Since the air trapped inside the cavity has to diffuse out, it takes time for the micro-cavity to reach the same vacuum level as the outside environment in the vacuum chamber. Gas resident time is an important experimental parameter to determine when the bonding process should start after the system is placed into the chamber. It can be estimated by using fluid mechanic theory. Figure 42 shows the simulation results of residual pressure of cavity versus gas resident time. The cavity pressure can reach lower than 30 mtorr after inserting the system into 25 mtorr vacuum chamber for 90 minutes. Therefore, the Q -factor can be increased by keeping the package under vacuum for an extended period of time (>10 minutes) before the cap is bonded to the substrate. Figure 43 shows a μ -resonator ($\sim 81\text{kHz}$) with a Q -factor of ~ 2500 bonded at 25 mtorr after ~ 90 minutes of pumping down time.

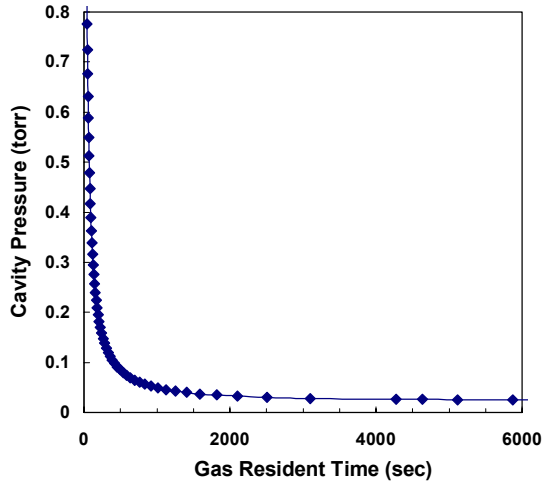


Fig. 42. Simulation result of the cavity pressure versus the gas resident time inside the cavity.

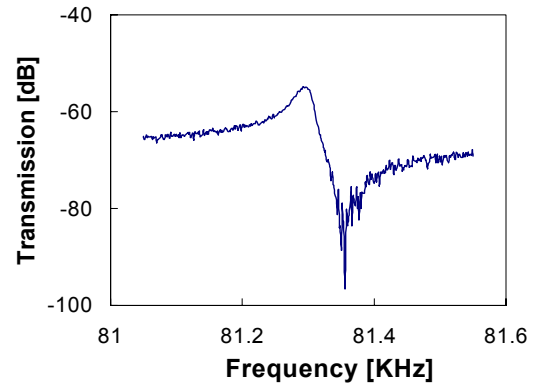


Fig. 43. The frequency spectrum of μ -resonator with 90 mins. wait time in vacuum.

4.2.2 Localized CVD Bonding for MEMS Post-Packaging

Another localized bonding process was conducted for MEMS packaging applications based on localized CVD bonding. This new bonding method applies the same filling and sealing principal of the global LPCVD hermetic sealing processes but only grows the CVD films locally [20]. This localized CVD process was expected to overcome the general bonding problem of surface roughness by selectively filling the bonding gap. As such, it has potential for bonding of devices or substrates for MEMS fabrication and packaging, as shown in Figure 44. Unfortunately, although the localized CVD process was successfully performed and characterized, the problem of heavy residual stress created during the bonding process was too great to be overcome such that the device bonding procedure can not achieve good sealing or vacuum level. As a result, we went away from this approach but came up with a “locally” localized growth and sealing process by using anodic bonding as the first step to seal most of the bonding areas. The final sealing is then accomplished by using the local CVD process and the details of the fabrication process are to be discussed in section 4.2.5. This section discusses the fundamentals of CVD sealing processes.

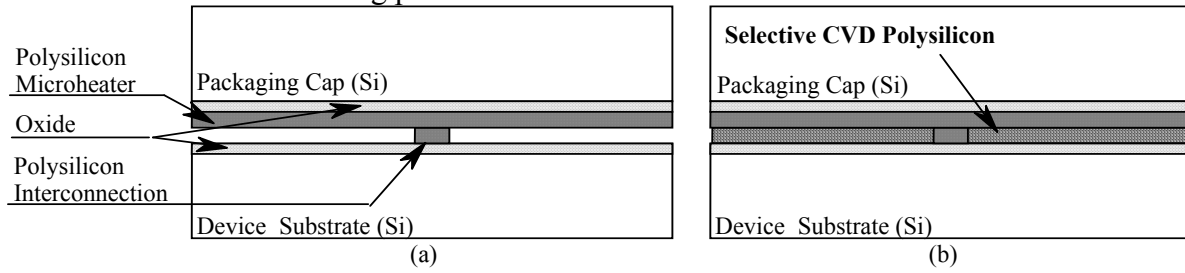


Fig. 44. (a) Schematic diagram of the bonding test. (b) Localized CVD polysilicon has filled and sealed the gap.

Figure 44 shows the schematic diagram of the localized CVD bonding process. The bottom device wafer has a polysilicon interconnection that generally introduces a bonding problem by creating a bonding gap between the packaging cap and the device substrate, as shown in Figure 44 (a). The selective CVD polysilicon deposition process is to be conducted to grow a layer of localized CVD polysilicon to fill the gap, as shown in Figure 44 (b). After the CVD bond is forcefully broken, the shape of the microheater is transferred to the device substrate as shown in the optical microphoto of Figure 45. By examining the packaging cap in the SEM, shown in Figure 46, only two traces of material can be found. Since the two trails of material resemble the shape of the microheater, they appear to be the over-deposited, localized CVD polysilicon along with the edges of the microheater. The microheater, which was originally deposited on top of the thermal oxide layer, is detached from the packaging cap completely and attached to the device substrate. These experimental results demonstrate that the localized CVD bond is very strong. Because this phenomenon is consistently observed in our experiments, it is concluded that the strength of the CVD bond is on the same order of the bond between the LPCVD polysilicon microheater and thermal oxide.

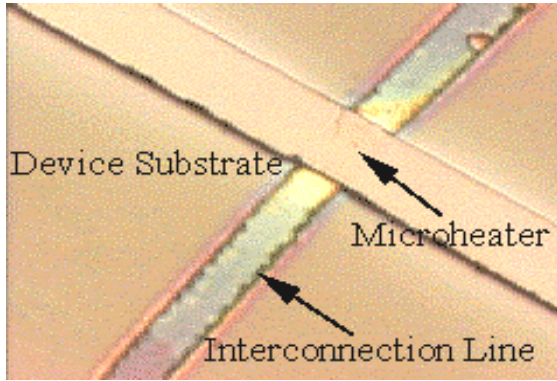


Fig. 45. Top view of the device substrate showing interconnection line and detached microheater.

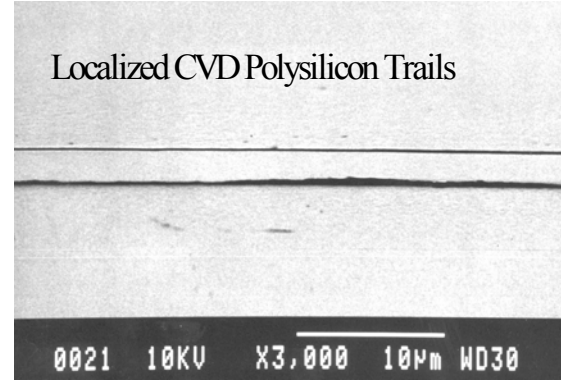


Fig. 46. SEM photo of the packaging cap showing trails of localized CVD polysilicon.

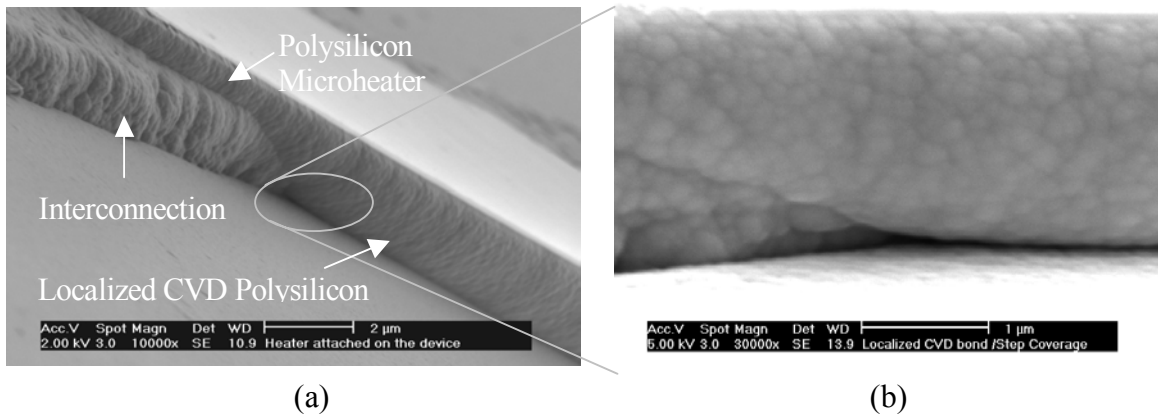


Fig. 47. Selectively deposited polysilicon has filled the 1 μm deep gap. (a) The intersection of the interconnection line and microheater. (b) The close view showing step coverage.

Figure 47(a) shows the SEM microphoto at the intersection of the interconnection line and the microheater and Figure 47(b) is the close view showing the step coverage. The newly deposited CVD polysilicon has successfully filled the 1.0 μm gap as shown. In the intersection region, localized polysilicon deposition may even occur on the interconnection line due to strong heat transfer from the microheater. In order to examine the bonding condition inside this intersection, a 30-second 10:1 HF dip is conducted followed by a 5-second silicon etchant [$\text{HNO}_3(70\%) : \text{HF}(40\%) : \text{H}_2\text{O} = 65 : 5 : 30$] dip. The close view SEM microphoto after the etching is shown in Figure 48. It is observed that the interface of the PECVD oxide and the microheater is continuous on top of the interconnection line. This suggests that a good bond is being formed either by fusion bonding or the gas filling process. At the regions outside the interconnection line, the contact between the localized CVD layer and PECVD oxide is also continuous, suggesting good bonding. On the other hand, Figure 48 also shows that silicon etchant seems to attack the original microheater faster than the deposited CVD polysilicon. This can be evidenced from the bigger and deeper voids on the top of the microheater than those on the deposited CVD polysilicon.

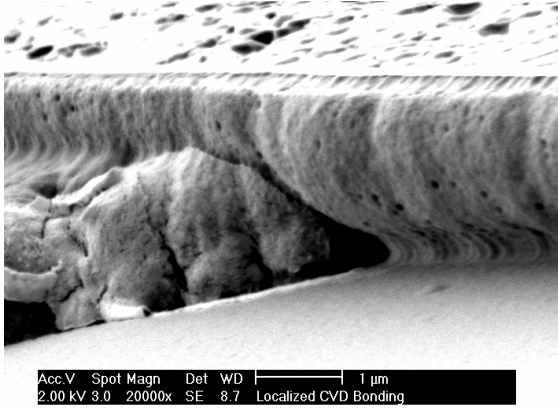


Fig. 48. Step coverage after dipping in 10:1 HF for 30 seconds and silicon etchant for 5 seconds.

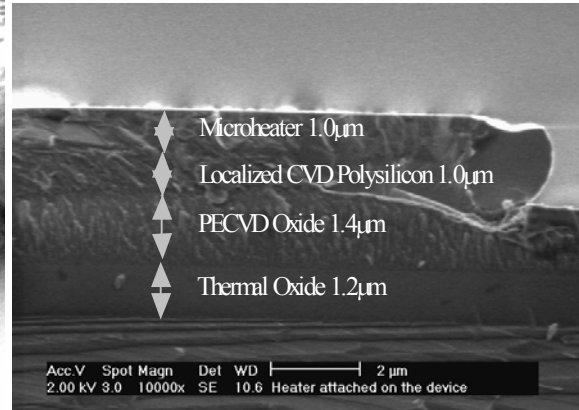


Fig. 49. Cross sectional view of localized CVD bond.

Figure 49 shows the cross sectional view of a cleaved CVD bond. It is observed that no voids can be identified on the localized CVD layer. Furthermore, it is difficult to tell the LPCVD polysilicon film (microheater) and the localized CVD polysilicon because they have very similar grain structure. On the other hand, the thermal oxide layer seems to have better uniformity than the PECVD oxide. This sample was then etched in 10:1 HF for 30 seconds and silicon etchant for 20 seconds to examine the interfaces. After these processes, Figure 50 shows the cross sectional view of silicon substrate, thermal oxide, PECVD oxide and localized CVD polysilicon. The microheater is completely etched away since the silicon etchant has a nominal etching rate of about 3 $\mu\text{m}/\text{min}$ for doped polysilicon.

In the first effort to construct the packaging cap, a microheater with a square shape was designed. Localized CVD polysilicon is then grown for 1 hour. Figure 51 shows the deposition result and it is observed that the deposition rate at the corners is higher than other places. This phenomenon can be explained by applying an electro-thermal, finite element analysis, as shown in Figure 52. When an electrical current is passing through the microheater and separating into two components, the sharp corners appear to experience higher temperature and higher deposition rate. On the other hand, a non-conducting structure is connected at the center of the microheater and a big contact pad is placed at the left-hand side. Both structures create heat loss paths that lower the temperature locally. They appear to slow down the deposition rate as suggested in Figure 51. The fact that the deposition rate is heavily dependent on the temperature profile indicates that the localized CVD is limited by surface reaction. In order to improve the uniformity, circular shape corners were designed in the new run, as shown in Figure 53. In this SEM microphoto, a uniform deposition is observed over the whole microheater that encloses the device area inside. Therefore, the new design is expected to seal micro devices uniformly inside the cap.

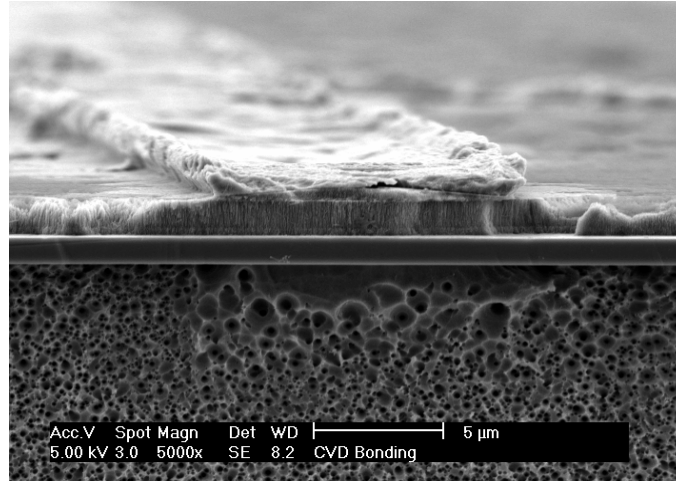


Fig. 50. Cross sectional view of a cleaved CVD bond.

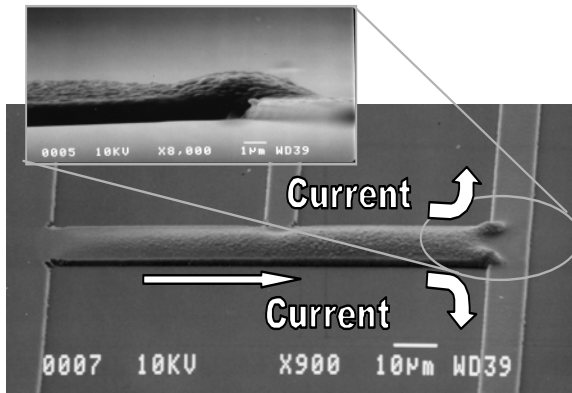


Fig. 51. The profile of localized CVD polysilicon.

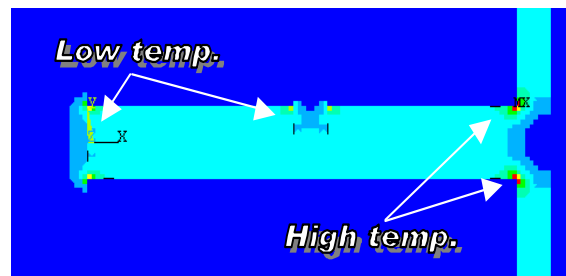


Fig. 52. FEA temperature simulation.

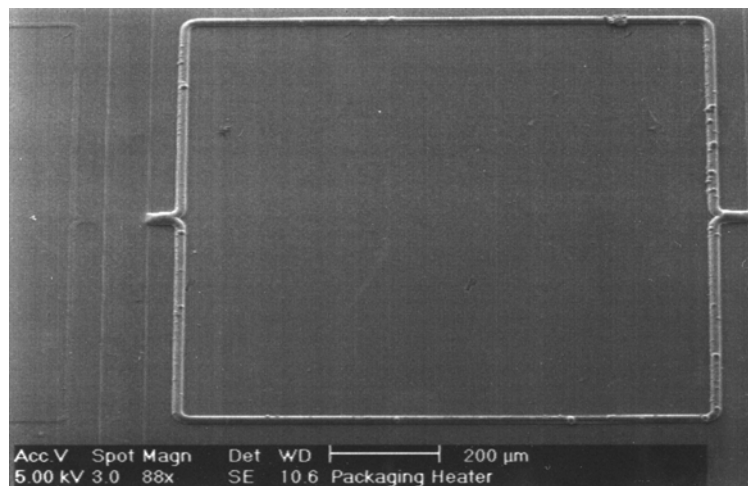


Fig. 53. Localized CVD polysilicon is uniformly deposited on a rectangular heater, 1000 x 800 μm², to enclose MEMS devices.

Figure 54(a) shows a released comb resonator with surrounding PSG layer. A silicon packaging cap substrate with microheater was used for the post-packaging process. As shown in Figure 54(b), part of the packaging microheater has been transferred to the device substrate. Moreover, the PSG layer on the device substrate has poor etching and causes a very rough surface, but the localized CVD process seems to fill the gap and will have no problem in achieving the sealing. However, we found that the thermal stress is a big problem in this process such that the microheater cracked at the completion of the process. Section 4.2.5 presents an improved design and successful vacuum encapsulation of a micro resonator.

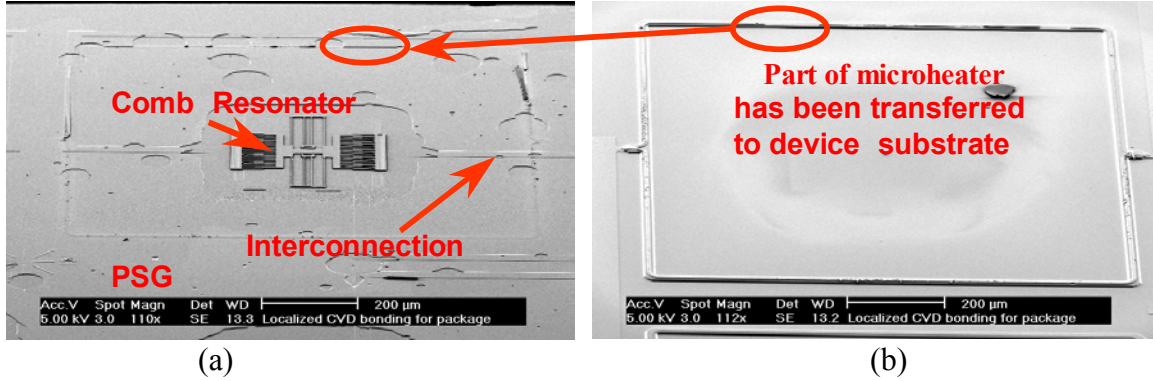


Fig. 54. (a) Device substrate after CVD bonding. (b) Cap substrate after CVD bonding.

4.2.3 Zinc Bonding for MEMS Packaging at the Wafer-Level

In addition to the new localized bonding schemes introduced in Section 4.1, two new global heating and bonding systems were also conducted for the purpose of post-MEMS packaging processes. These are zinc bonding and Rapid Thermal Processing (RTP). Both methods aim to reduce the thermal budget generally required in other bonding methods. This section summarizes the zinc bonding results. Figure 55 illustrates the schematic of the zinc bonding process for encapsulating MEMS devices [21]. The electroplated nickel on the device substrate aims to form a cavity for the MEMS device. Low melting temperature zinc is deposited on the top of the nickel layer and is used as the bonding solder. The cap wafer has a defined metal layer to assist with the zinc bonding process. The whole setup is placed inside a nitrogen oven for bonding. Figure 56 shows the microfabrication process. A silicon substrate as shown in Figure 56 (a) is first thermally oxidized to grow a 1 μm-thick oxide as the electrical insulation layer. Chromium/Gold of 200Å/2000Å in thickness is deposited afterwards. A photoresist is coated on the chromium/gold layer, followed by patterning the photoresist layer, as shown in Figure 56 (b), as the seed layer for the nickel and zinc electroplating process. A 2 μm-thick nickel is electroplated at the temperature of 50°C in a nickel-sulfate-base electrolyte and the current density is 500A/m². This layer serves as the support of the packaging cavity, see Figure 56 (c). A 2 μm-thick zinc layer is electroplated afterwards on top of the electroplated nickel at a temperature of 25°C and a current density of 200A/m² in a zinc-sulfate-base electrolyte, Figure 26 (d). After removal of the photoresist, Figure 56 (e), a cap wafer that is coated with the 200Å/2000Å of chromium/gold layer is used to seal the cavity, Figure 56 (f).

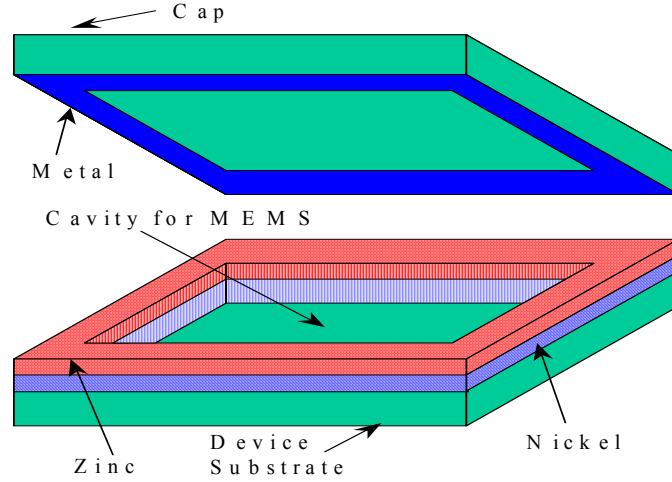


Fig.55. Schematic of the zinc bonding process: The electroplated zinc is bonded to the metal (Au) on the cap under a bonding temperature of 425°C while the electroplated nickel is not melted.

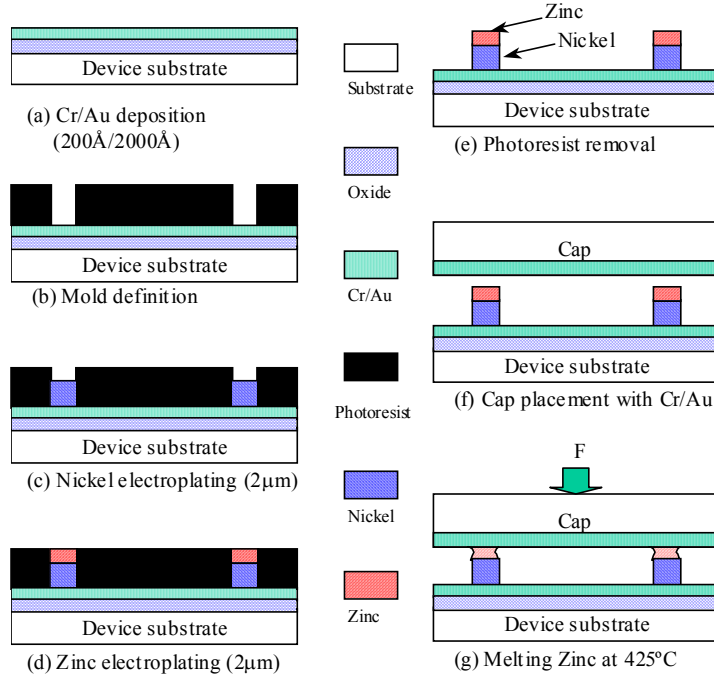


Fig. 56. Microfabrication process for the zinc bonding: zinc is electroplated on top of electroplated nickel; zinc is melted for bonding at 425°C, while nickel is not melted at this temperature and nickel functions as the structural layer to form the cavity.

After pressing the wafers with the bonding pressure of 1000N/m² and placing the wafers inside a nitrogen oven, the bonding process is completed at the temperature of 425°C for 90 minutes as shown in Figure 56 (g). During the bonding process, the electroplated zinc is melted at the temperature of 425°C and bonded with the cap wafer. The electroplated nickel having higher melting temperature than the zinc is not melted during the bonding process such that nickel can function as the structural layer to form the cavity.

Figure 57 shows an SEM photograph of the device substrate with the electroplated nickel and zinc before bonding. The encapsulation area is $600 \times 600 \mu\text{m}^2$ and the width of the zinc/nickel layer is $80 \mu\text{m}$. Figure 58 shows the enlarged view of the region “A” in Figure 57. The coarse zinc grain in Figure 58 is formed during the electroplating on top of the fine nickel layer. A layer of zinc-nickel alloy can be identified in Figure 58 between the top zinc grain and the bottom fine nickel layer. After the bonding process, the bond is forcefully broken in order to examine the bonding interface and to estimate the bonding strength. Figure 59 shows the device substrate that is severely damaged when the bond is forcefully separated. It is observed that parts of silicon are fractured and indicates a strong bond is formed and the bonding strength is comparable with the fracture toughness of silicon. Two areas, marked as B and C in Figure 59 are examined further. In Figure 60, which is the enlarged view of area B of Figure 59, one can identify the gold layer on top of the device substrate. A $5 \mu\text{m}$ wide gold stripe, at the edges of the broken silicon, seems to be missing and was believed to be torn away when the bond is forcefully broken. On the other hand, shown in Figure 61 is the area that zinc/nickel layer is still left on the device substrate. The close view SEM picture, when compared with Figure 58, suggests that a new structure is formed. Since the processing temperature is higher than the melting temperature of zinc, the granular structure on the side wall of the encapsulating ring is possibly the recrystallized zinc that flows over the nickel layer from the top during the bonding process. The top zinc layer shows signs of broken connections that may be the result of high external force used to break the bond. These experimental results indicate that electroplated zinc may melt and recrystallize after being heated up. Depending on the material of the cap substrate, this melting and recrystallizing process may be a good catalyst for bonding, as demonstrated in this work. Since the demonstrated bonding temperature is in the range of 425°C , which is lower than many of the other bonding processes commonly used in MEMS fabrication, zinc bonding may provide a feasible low cost, low temperature bonding process for MEMS packaging applications.

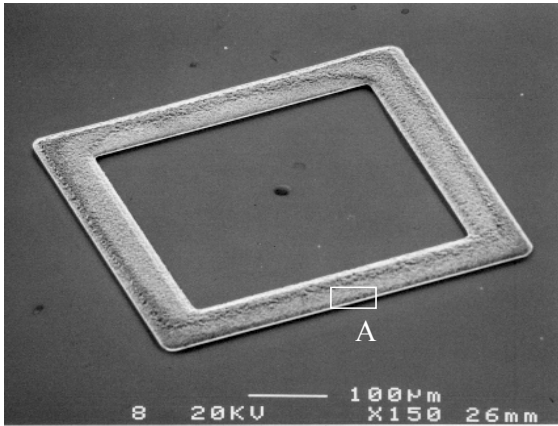


Fig. 57. SEM photograph of electroplated nickel and zinc before bonding.

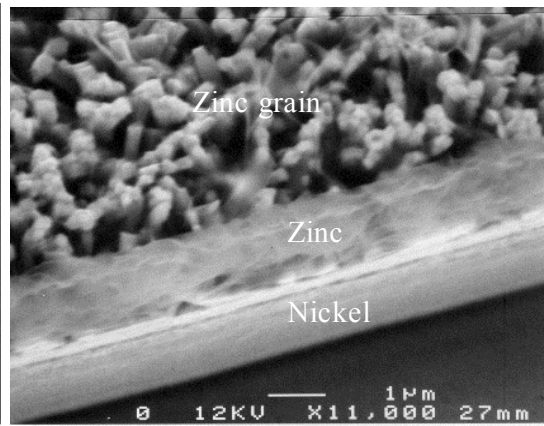


Fig. 58. Enlarged view of A in Fig. 57. The zinc is electroplated on the top of electroplated nickel.

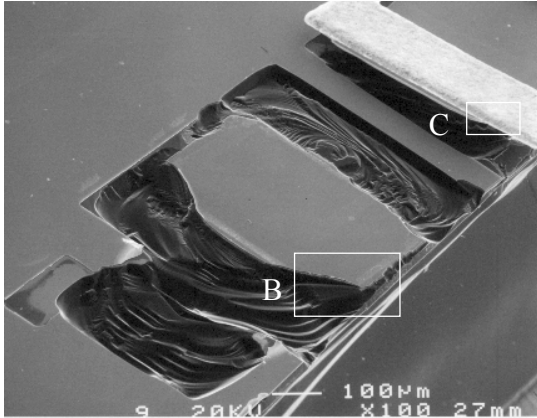


Fig. 59. SEM photograph of the silicon substrate after zinc bonding. The bonded wafer was forcefully broken.

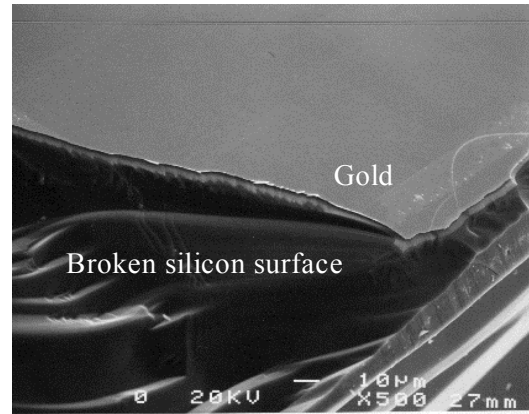


Fig. 60. Enlarged view of B in Figure 59. The broken silicon suggests that bonding strength between zinc & gold is comparable to the fracture toughness of silicon.

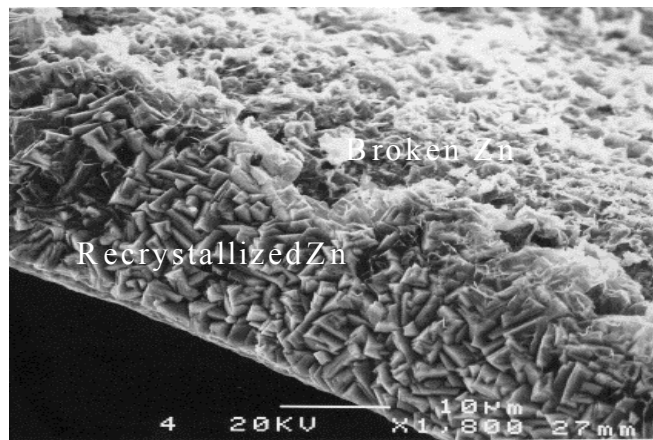


Fig. 61. Enlarged view of C in Figure 59. Electroplated nickel is covered with recrystallized zinc, generated after heating; the torn zinc is on the top of nickel.

4.2.4 Massively Parallel MEMS Post-Packaging by Using Aluminum-to-Nitride RTP Bonding

The second non-localized heating and bonding scheme is by RTP (Rapid Thermal Processing) bonding to lower the thermal budget because of the very rapid high temperature-processing step. Aluminum-to-silicon nitride bonding has been demonstrated for the first time in microsystem technologies [22]. The reason to pick silicon nitride in the bonding system is that silicon nitride has been commonly used as the top passivation material in both microelectronics and MEMS. However, bonding processes for silicon nitride generally requires high temperature and a long period of time. In this section, RTP aluminum-to-silicon nitride bonding is demonstrated and a comb-shape micro resonator is encapsulated for accelerated hermeticity tests.

Figure 62 shows the schematic illustration of this MEMS packaging process. A standard surface-micromachined MEMS structure is surrounded by an integrated sealing ring with silicon nitride as the topmost layer. A Pyrex (Corning 7740) glass wafer is deposited and patterned with aluminum sealing rings and then flip-chip assembled with

the device wafer. For aluminum bonding rings of 4 μm thick and 100-200 μm wide, the optimum bonding process is found at 750°C for 10 seconds. Figure 63 shows a comb-drive resonator resonating at 17.0 kHz under the glass package immersed in DI water. Figure 64 is the SEM microphoto of silicon substrate after forcefully breaking the bond. The glass debris is attached to the substrate and implies the bonding strength is greater than the fracture toughness of glass at 10 MPa. In order to characterize the bonding mechanism, X-ray diffraction (XRD) was conducted and the result is shown in Figure 65. Since no new crystalline structure other than Al and Si can be detected, it is concluded that the bonding mechanism is dominant by diffusion of aluminum into silicon nitride. Figure 66 shows experimental results of RTP bonding and an activation energy of 2.5 eV was obtained.

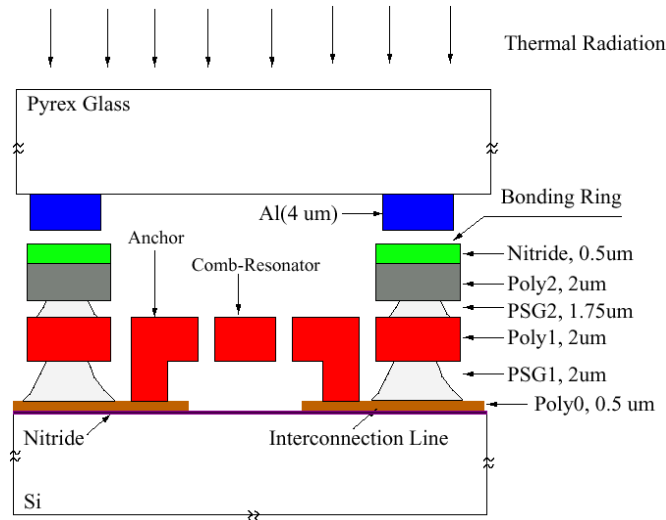


Fig. 62. The schematic diagram of massively parallel MEMS post-packaging by using RTP aluminum-to-nitride bonding.

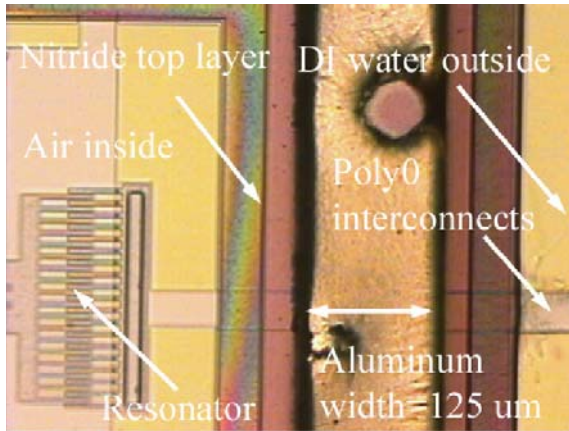


Fig. 63. A comb resonator is resonating at 17kHz while immersed in DI water.

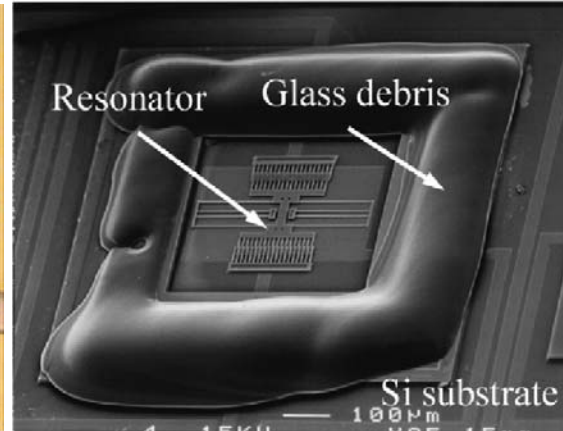


Fig. 64. Glass debris on the silicon substrate after forcefully breaking the bond.

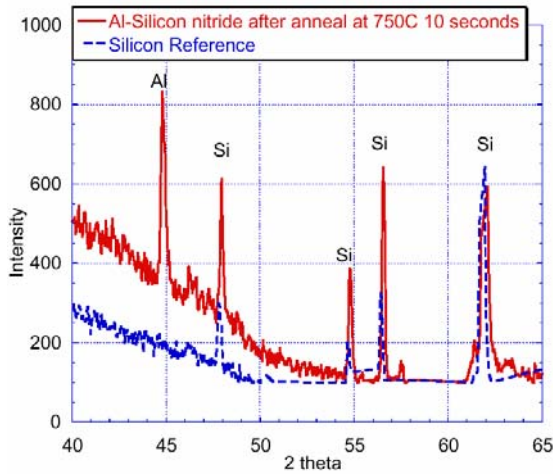


Fig. 65. X-ray diffraction (XRD) spectrum result at the bonding interface.

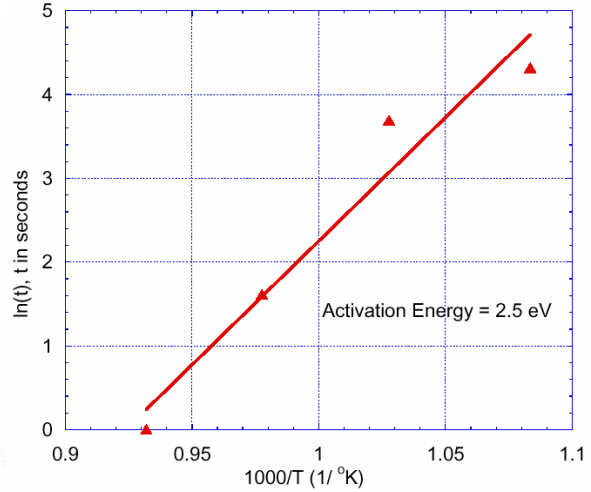


Fig. 66. Experimental tests of RTP bonding showing an activation energy of 2.5eV for the aluminum-to-nitride bonding system.

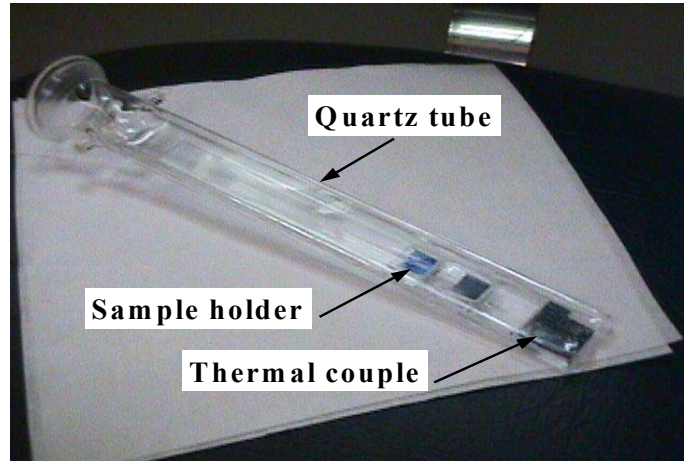


Fig. 67. Quartz tube for the RTP vacuum packaging process.

Vacuum packaging technologies based on Rapid Thermal Processing (RTP) wafer bonding was also demonstrated [23]. Following the RTP Al-to-nitride bonding procedure in our previous discussion, the flip-chip assembled pair of device wafer and glass cap wafer is aligned and loaded into a quartz tube. Figure 67 shows the quartz tube for the vacuum packaging process. A thermal couple is mounted inside the tube to monitor the temperature changes during the bonding process. After the quartz chamber is evacuated to a vacuum level of about 10 mTorr, the RTP system is activated and aluminum-to-nitride bonding is formed after 10 seconds of heating at 750°C. It is observed that vacuum can be achieved if the process is conducted carefully to avoid the out gassing problem during the bonding process. Typically, the glass cap should be baked in elevated temperature of more than 300°C for more than 10 hours for better results. Experimentally, three comb-shape micro resonators were successfully vacuum-encapsulated. The results are shown in Figure 68, with quality factors in the range of 1800, 400 and 200, when the glass cap was baked in vacuum for 12, 4 and 0 hours,

respectively. Figure 68 also shows the long-term stability of Q up to 37 weeks. The measurement was done by a micro-stroboscope. The quality factor is extracted as 1800 ± 200 corresponding to a pressure of 200 mTorr inside the package. The resulting Q is found to increase if the pre-baking process period is increased. Figure 69 shows the accelerated testing results of a vacuum-packaged comb-resonator. The Q stays at 200 after 24 hours of testing time in harsh environment (130°C , 2.7atm and 100%RH). Figure 70 shows the SEM photo of the silicon substrate after forcefully breaking the bond. The glass debris is attached to substrate and cracks formed in the bulk silicon suggest the bonding strength is greater than the fracture toughness of single crystalline silicon.

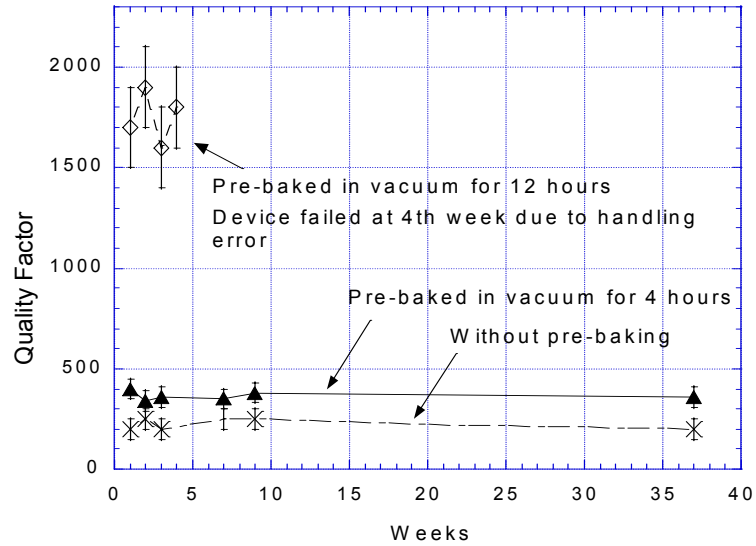


Fig. 68. Long term stability tests of Q for 37 weeks. Q is found increasing with pre-baking time in vacuum.

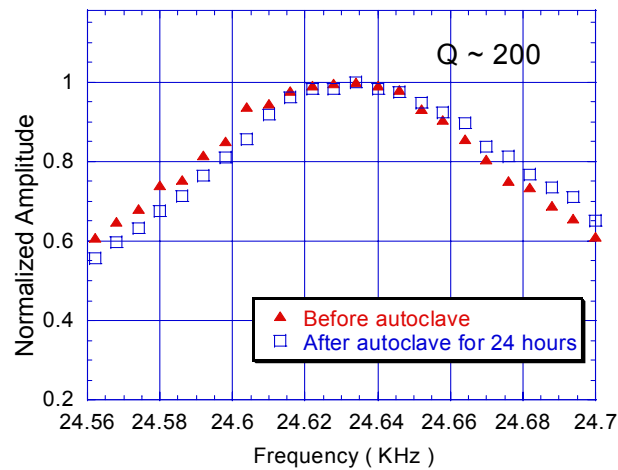


Fig. 69. Accelerated testing results of a vacuum-packaged comb-resonator. The Q stays at 200 after 24 hours of testing time in harsh environment.

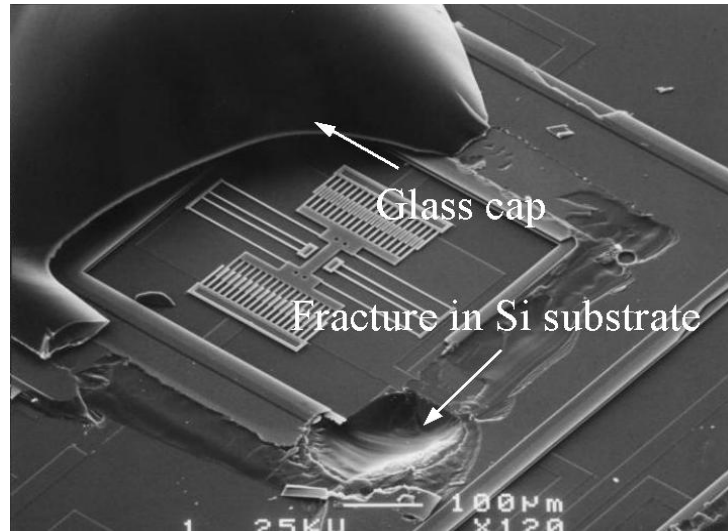


Fig. 70. SEM microphoto of silicon substrate after forcefully breaking the bond. Bulk glass is found on the silicon substrate.

4.2.5 Vacuum Packaging Using Localized CVD Deposition

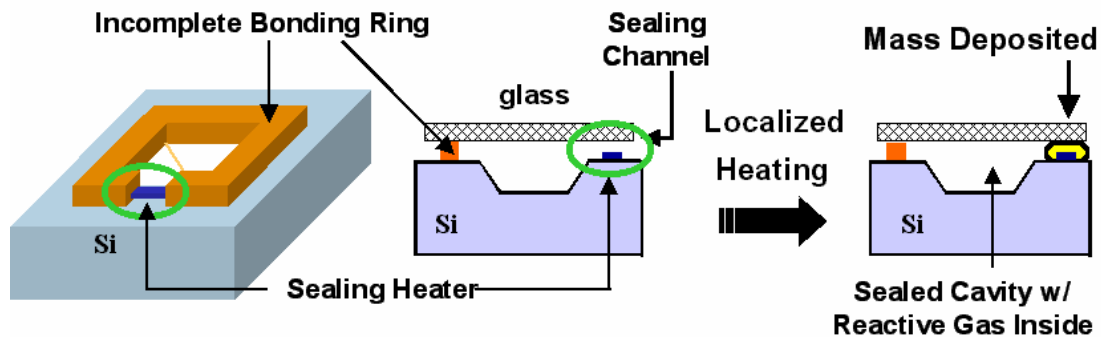


Fig. 71. Schematic diagram of the packaging approach.

This sub-section describes wafer-level hermetic packaging techniques for vacuum-sealed cavities along with selective post-package trimming using anodic bonding and localized mass deposition that was discussed in section 4.2.2. The three major tasks are: (1) to investigate wafer-level vacuum packaging for sensors and actuators and to better understand out-gassing problems in sealed reference pressure chambers, (2) to develop effective techniques for in-chamber environmental control, and (3) to evaluate the use of mass deposition for trimming the resonant frequencies of high performance microstructures. A post-packaging pressure control system has been designed to investigate the feasibility of wafer-level packaging and in-chamber environmental control by localized heating. Our approach is to package sensors or actuators in a low-pressure environment, to monitor that environment with a pressure switch, and to actively maintain it internally with a getter. The three system components are: a) first-level packaging (required to seal the device at a low pressure), which can be achieved by the selective localized cavity sealing method described in Figure 71 in the final mass deposition step; b) a pressure monitoring unit for monitoring the vacuum in the sealed

cavity and for triggering the pressure control mechanism if necessary; and c) a pressure control unit to actively maintain cavity pressure below a critical level. Our target pressure is 10mTorr, which is demanded by many high performance MEMS devices. During the normal operation of a sensor or an actuator, the pressure-monitoring unit can be turned on periodically to check the cavity pressure. If the pressure exceeds the system's critical level, the pressure control unit can be activated to restore the vacuum to an acceptable level.

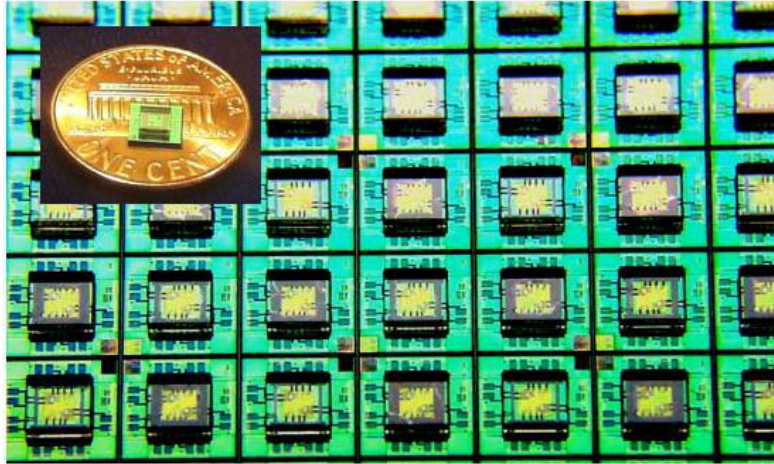


Fig. 72. An optical photograph of a device array.

A fabricated array of devices is shown in Figure 72. Each die is 5mm by 5mm with a 1.2mm by 1.2mm cavity, depending on the bonding ring design. The device cavity is formed by bonding a partially-diced 7740 Pyrex glass cap wafer to a polysilicon ring that has an opening with a sealing heater located at this opening, see Figure 71. Cavities with bonding ring widths of 150 μ m, 300 μ m, and 500 μ m were fabricated. Each cavity contains two comb resonators and two polysilicon gettering heaters (Figure 73).

The package is sealed using selective CVD, followed by reaction of the residual gas within the cavity using the gettering heaters to create the desired reference pressure. Localized CVD is performed in a low-vacuum silane environment. The channels are 2 μ m wide, and are sealed in a PECVD chamber with a 40sccm SiH₄ flow at 200mT. The gettering heater is activated to getter the Si atoms in the cavity. The packaged resonators were tested to evaluate the quality of the seal. This measurement was performed with the package exposed to atmosphere. Quality factors of 2300 were obtained from the packaged resonators (Figure 74). To estimate the pressure inside the cavity, the quality factor was measured as a function of pressure for an unpackaged resonator in a vacuum chamber. The data is shown in Figure 75. A quality factor of 2300 indicates that a cavity pressure below 50mTorr was achieved. Current design of the test vehicle has been modified to improve resonator yield and to address galvanic biasing issues during resonator release. Fabrication of this device is completed and testing is currently in progress.

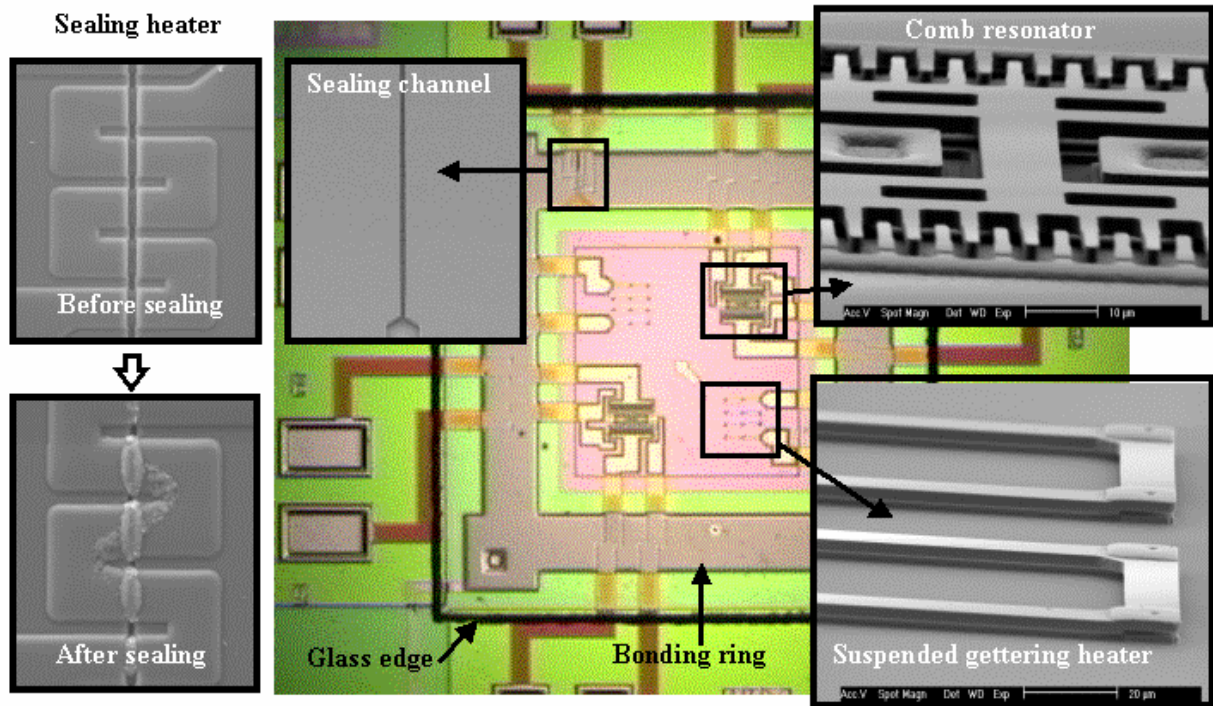


Fig. 73. Photographs of a single device and its contents.

To demonstrate frequency trimming by localized deposition, an electrostatically-driven bulk-micromachined cantilever resonator is incorporated into the design of the post-packaging pressure control system described above. The purposes of this integration are: (1) to confirm cavity pressure via two different mechanisms, (2) to compare device performance and pressure sensitivity of the vertical as well as lateral resonators, and (3) to demonstrate the process compatibility of this packaging technique with bulk-micromachined processes.

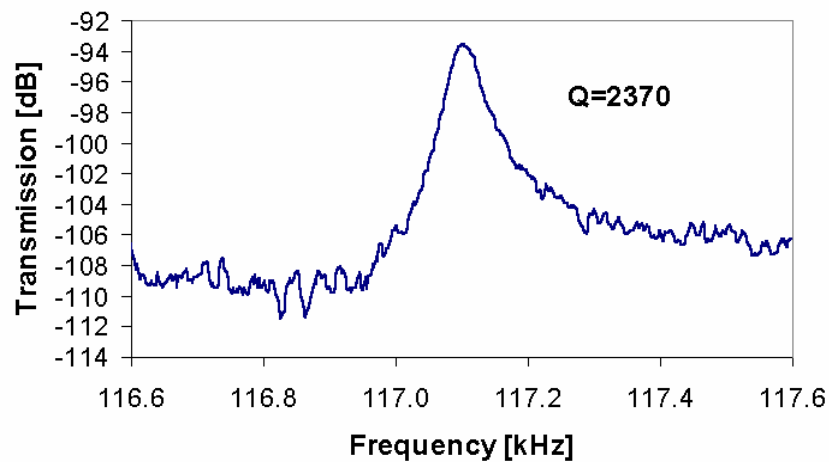


Fig. 74. A transmission spectra obtained from a packaged comb resonator.

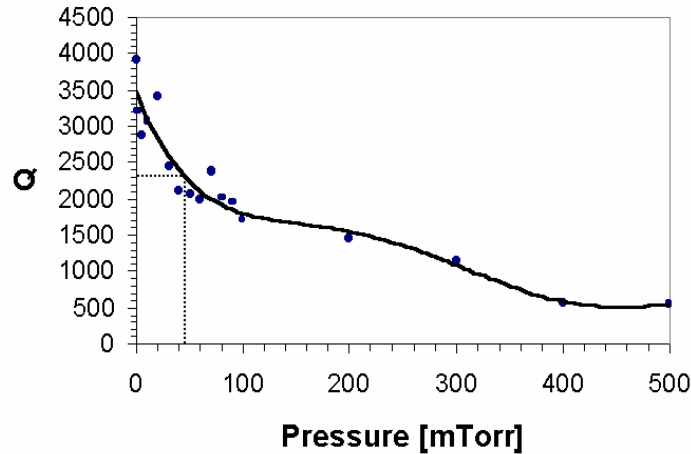


Fig. 75. Quality factor vs. pressure obtained from an unpackaged resonator.

To demonstrate process compatibility and system integration capability, this localized CVD packaging technique is applied to an absolute pressure sensor. A fabricated array of pressure sensors is shown in Figure 76. Each device is 5mm by 5mm. The reference cavity is formed using an anodic bond between glass and an incomplete polysilicon ring with a sealing heater at the ring opening. Figure 77 shows the layout of the pressure sensor. Each device consists of one pressure sensor, one sealing heater, two comb resonators, and two suspended gettering heaters. The pressure sensor is located in the center cavity, the comb resonators and the gettering heaters are in shallower cavities in the bonding area. Five different pressure sensors plus a reference sensor were designed to cover the dynamic range (500 to 800Torr). The recessed area is composed of a center cavity for the pressure sensor and four side cavities housing two comb resonators and two polysilicon gettering heaters as shown in Figure 78, which are components of the post-packaging pressure control system.

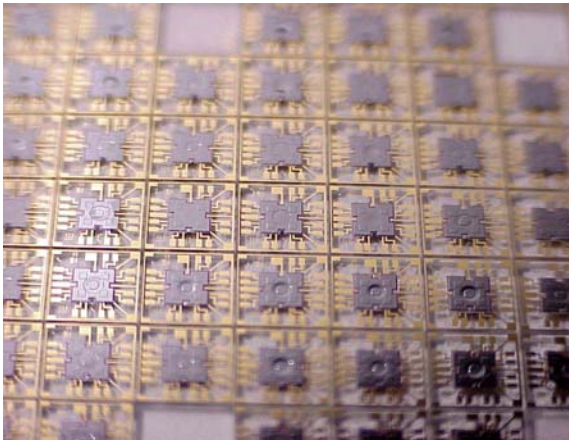


Fig. 76. An optical photograph of the fabricated pressure sensor array.

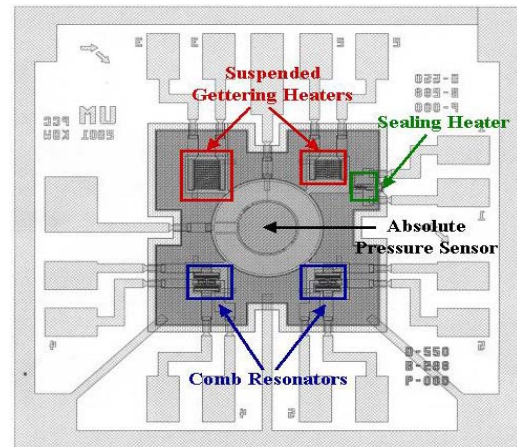


Fig. 77. Layout of an absolute pressure sensor.

The device is sealed using localized CVD, subsequently reacting any residual gas within the cavity using the getters to create the desired reference pressure, as measured

using the in-cavity resonators. Figure 79 shows the sealing channel, which has a cross-section of $2\text{ }\mu\text{m}$ by $2\text{ }\mu\text{m}$ and is sealed in a PECVD chamber with 80sccm SiH_4 flow at 250mT for 30 minutes. The estimated local deposition temperature is 600°C . The gettering heaters are then activated to further reduce the cavity pressure. Capacitance vs. pressure data obtained from some of the pressure sensors are shown in Figure 80.

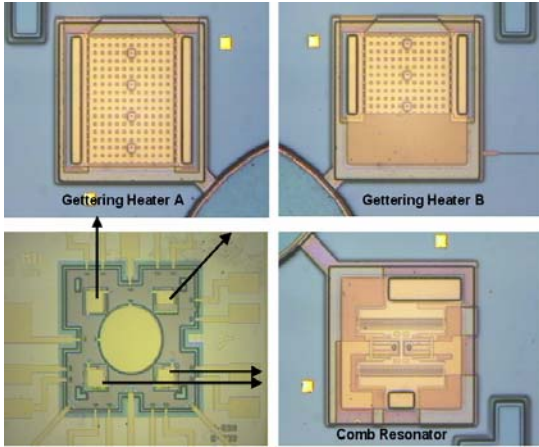


Fig. 78. Optical photograph of a single device (back side view) and its contents.

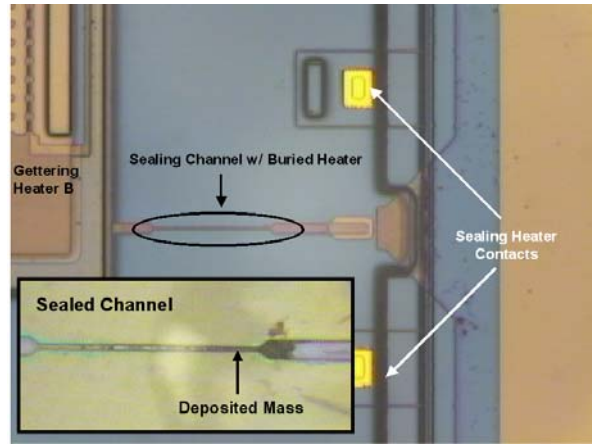


Fig. 79. Optical photo showing the details of the sealing channel region.

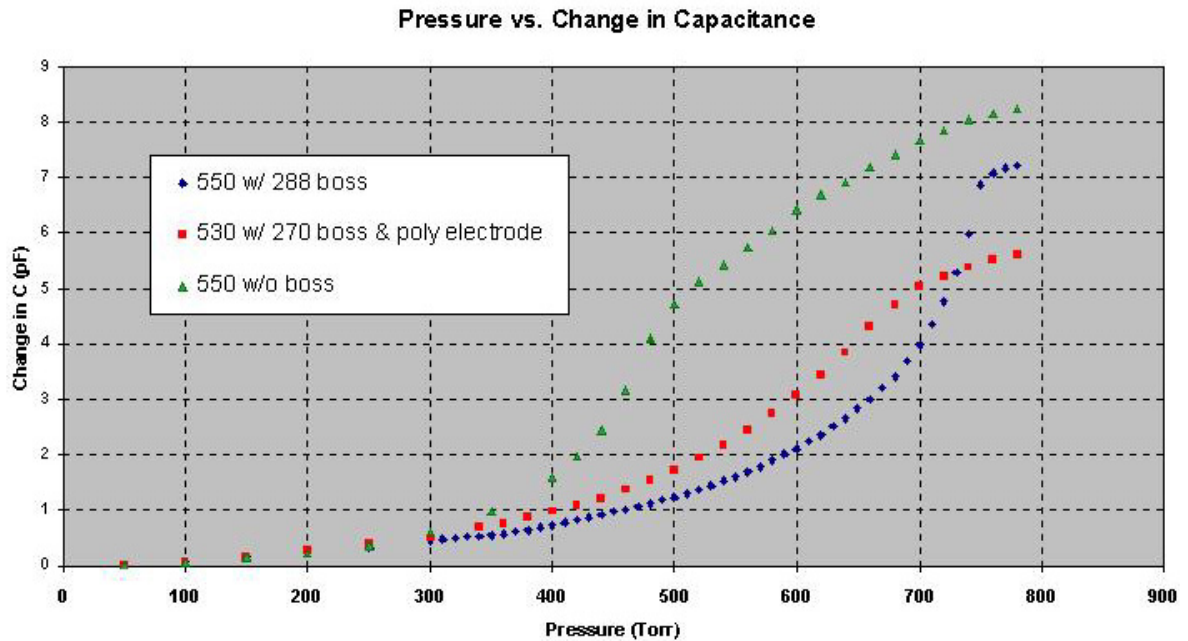


Fig. 80. Pressure vs. change in C obtained from some of the fabricated pressure sensors.

4.2.6 Reliability Tests of MEMS Packages

We were concerned about the bonding interface and potential leakage of our new localized bonding methods. In this particular study, we not only move forward in the demonstration of device-level packaging but also in an effort to characterize the bonding interface by testing the hermeticity. Hermetic packaging is a critical requirement for integrated circuit and MEMS applications. The package should protect devices not only from the hostile external environment for longer lifetime, but also from contaminants for better device performance. Previously, several researchers have proposed methods for hermetic seals and it is important in our current work to demonstrate that hermetic sealing can be accomplished by our methods of localized bonding. A micro dew point sensor is first fabricated and packaged by means of localized silicon/aluminum-to-glass bonding in this work. The schematic diagram of the process flow is illustrated in Figure 81. The structure consists of polysilicon interconnect lines, which transfer signals from the sealed inside cavity of the package to the outside world, an on-chip polysilicon microheater, and the bonding material, which in this case is aluminum/silicon. The fabrication process follows our previous discussion on localized solder bonding in section 4.2.1 with a built-in aluminum-based dew point sensor. After forming the polysilicon interconnect line and microheater, an oxide (1000Å)/nitride (500Å)/oxide (1000Å) sandwich layer is grown on top of polysilicon microheater for electrical insulation. In order to prepare the aluminum/silicon-to-glass bonding system for packaging, which has a higher bonding temperature, above 700°C, than indium solder, the sandwich dielectric insulation layer is needed to effectively prevent aluminum solder diffusion. Without the insulator, aluminum diffusion will cause electrical current to proceed along the solder, instead of the poly-silicon microheater during bonding. After depositing the dielectric layer, aluminum (2μm) and polysilicon (5000Å) are deposited and patterned. A Pyrex glass capsule is placed on top of the device substrate. In initial experiments, bonding is achieved under an applied pressure of 0.1 MPa and a current input of 92 mA. In about 5 minutes, the localized aluminum/ silicon-to-glass bond is completed. Figure 82 shows an optical micrograph of a sealed dew point sensor observed through the glass package.

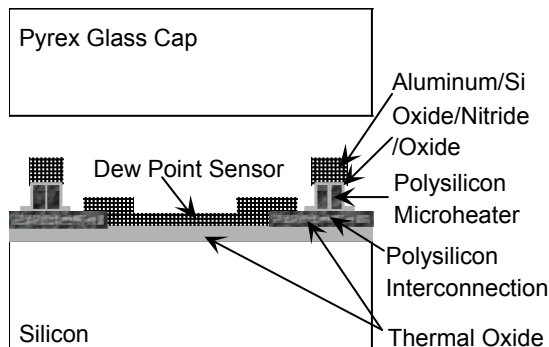


Fig. 81. Schematic diagram of hermetic package fabricated by localized aluminum/Si-to-glass bonding.

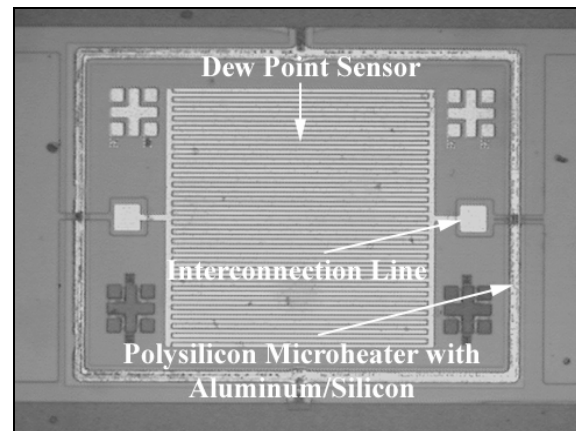


Fig. 82. Optical photograph of the hermetic package seen through the glass capsule.

The bonding temperature is controlled by the polysilicon microheater whose temperature is monitored by assuming a linear dependence of resistivity on temperature. According to a two dimensional heat transfer simulation by using FEA (Finite Element Analysis), the temperature of aluminum/silicon solder is $\approx 90\%$ of the microheater temperature due to the heat conduction loss to the electrical insulation layer. For example, it was found that a 46mA current input can make the microheater, designed as two parallel $3.5\mu\text{m}$ wide, $2\mu\text{m}$ thick phosphorus-doped polysilicon lines with $7.5 \times 10^{19}/\text{cm}^3$ dopant concentration and $2\mu\text{m}$ spacing, rise to 780°C which indicates the bonding temperature is around 700°C .

The package has been subjected to two kinds of tests: (1) a gross leak test in IPA (Isopropanol Alcohol), and (2) an accelerated test in an autoclave. Because IPA has better wettability than water, it can more easily penetrate small openings, and is more suitable for gross tests. It is observed that IPA cannot penetrate the aluminum/silicon-to-glass bond. The gross IPA test is useful in screening devices for the accelerated test. Accelerated testing is then performed in an autoclave on devices that passed the IPA immersion test. Hermeticity was tested using interdigitated patterns that operate as dew point sensors. Interdigitated dew point sensors have been widely used for lifetime testing of hermetic packages. The operating principle is based on the large resistance change between closely spaced interdigitated electrodes of the sensor. Once moisture condenses on the whole surface of electrodes, the capacitance between these electrodes will increase because the relative dielectric constant changes from dry air ($\epsilon_r=1$) to water ($\epsilon_r=80$). Moreover, water has higher electrical conductivity than dry air. Therefore, the total impedance of the dew point sensor will decrease when moisture enters and condenses inside the package. Figure 83 shows the drastic impedance and phase change for the dew point sensor after about 30 hours test. This is accompanied by moisture condensation inside the sensor as shown in Figure 84.

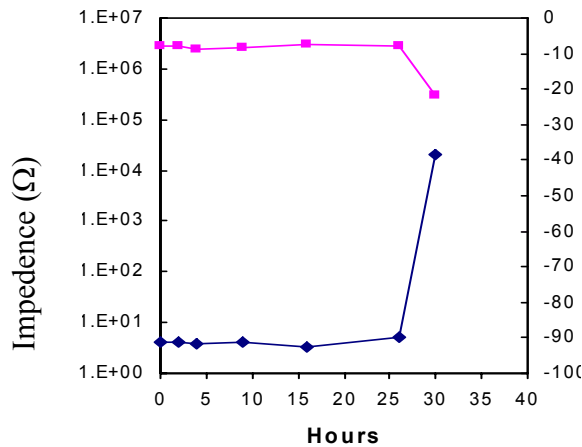


Fig. 83. Results from the autoclave test. After 30 hours, a drastic change is measured.

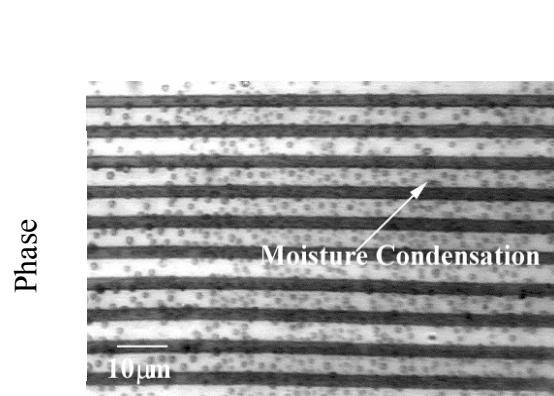


Fig. 84. Moisture condensation is found inside the package on the sensor.

In the first series of tests, a total of 11 packages were tested in the autoclave under the same bonding conditions. Six of these packages failed almost immediately after insertion into the autoclave, two failed after 30 hours, two failed after 120 hours, and one failed after 200 hours. In order to determine the failure mechanisms, the glass package was forcefully removed from the silicon substrate and the bonding region was examined.

It was observed that in many regions, either the glass or the microheater with its underneath silicon substrate was stripped and attached onto the other substrate, indicating a strong bond. However, when the bonding process was not conducted correctly, moisture can diffuse into the package. In the package that lasted 200 hours, the unbonded region is much smaller, and almost undetectable.

The strong hermetic sealing relies on the formation of aluminum oxide and silicon precipitate while aluminum solder reacts with silicon dioxide under high temperature environment. According to the broken interface between the glass and silicon substrate, the bonding strength is higher than the failure strength of Pyrex glass or silicon which is about 10MPa. Such a strong bond is very suitable for packaging. In the previous autoclave test results, the unbonded region is identified as a major leakage path for moisture diffusion. Since the bonding quality of aluminum/silicon-to-glass is determined by the interface reaction of aluminum-to-glass, which depends on bonding temperature and time, another 11 packages were re-fabricated and subjected to the autoclave test. In this second set of devices, all of eleven new packages are produced by increasing the bonding time and contact pressure, which were changed from 5 minutes to 7.5 minutes and from 0.1MPa to 0.2MPa, respectively. Increasing the contact pressure and bonding time ensure that aluminum solder intimately contacts and totally reacts with the glass substrate. Figure 85 shows the autoclave test results for this set of devices. Only one package failed immediately after insertion into the autoclave, three failed after 10 hours, three failed after 30 hours, one failed after 80 hours and three have survived more than 320 hours and are still under test. Even though some improvement has been obtained, it is evident that some devices still fail prematurely. Because raising the bonding temperature instead of time can also improve bonding quality, there are still many ways to improve bonding yield and quality. These other techniques are being studied.

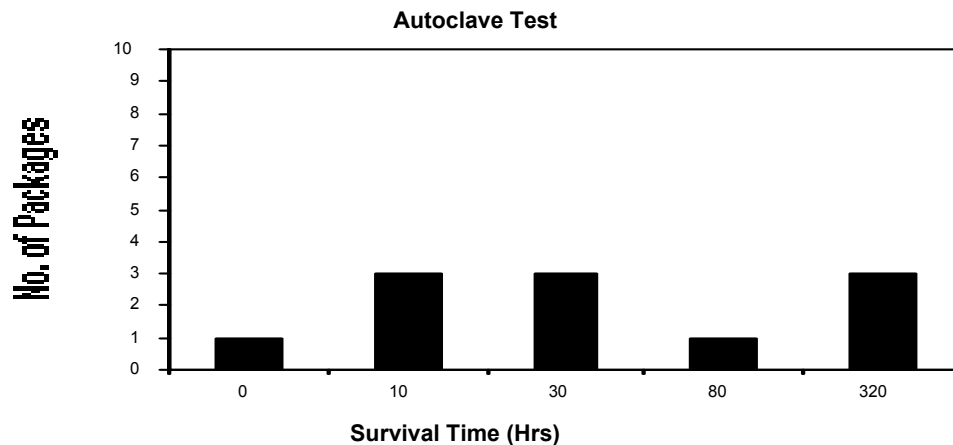


Fig. 85. Statistical autoclave test results of another 11 packages produced by increasing bonding time and pressure.

Based on Weibull distribution approximation which is a common statistical theory to calculate the mean time to failure (MTTF) of packages, it is found that the MTTF of the 22 glass-silicon packages formed using aluminum/silicon-to-glass bonding is only about 32 hours. Though this value is higher than published MTTF of epoxy-molded packages, which is about only 8 hours under 1 atm, 100%RH, and 130°C

environment, it is still much lower than we expected, especially for a metal seal. As mentioned, no unbonded regions can be found on the packages once they survive for more than 200 hours. Therefore, the failure mechanism should be different and needs to be identified. Moreover, MTTF is estimated by statistical methods, and the pressure effect of autoclave on the hermeticity test is still unknown. Using more devices for the test will provide more accurate MTTF and help us further understand the reliability of this packaging technology.

In order to develop bonding processes for massively parallel post-packaging for MEMS, we have successfully demonstrated the feasibility of hermetic wafer bonding based on rapid thermal processing (RTP). RTP is capable of providing low thermal budget; fast and inexpensive manufacture means and excellent bonding strength. As such, wafer bonding by RTP has promising potential for wafer-level MEMS fabrication and packaging. Most existing bonding technologies such as fusion and anodic bonding suffer from high temperature treatment, long processing time and damage to the circuitry. RTP has been used for many post-IC processes at low and controllable thermal budget such that RTP bonding, if successfully demonstrated, can solve the above problems in wafer bonding and provide an excellent way for MEMS post-processing.

Figure 86 shows the schematic illustration of wafer-level hermetic bonding by using RTP. A silicon substrate is deposited and patterned with aluminum to form an encapsulation area and a Pyrex glass wafer is placed on top and put into an RTP chamber. It is found that within a processing time of only 2 seconds at 990°C by thermal radiation, hermetic bonding is achieved. Figures 87 and 88 are bonding results seen under an optical microscope in air and immersed in IPA (Isopropanol Alcohol), respectively. In this particular case, one of the chambers is not fully sealed such that IPA went into the right bottom chamber (Figure 88). However, all the other chambers are completely sealed with no IPA penetration. Figure 89 is the close view SEM microphoto of the glass wafer after forcefully breaking the bonds. The originally flat glass wafer now has fractures along the bonding boundaries.

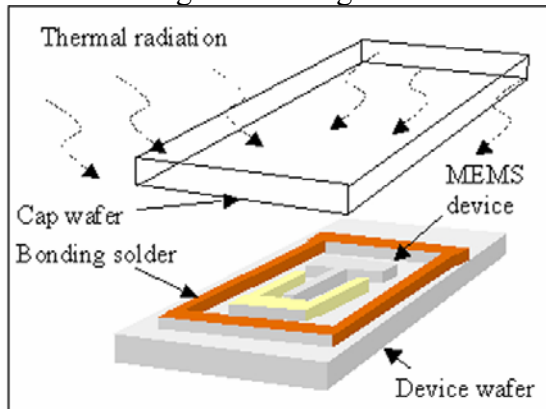


Fig. 86. Schematic of bonding by RTP (Rapid Thermal Processing).

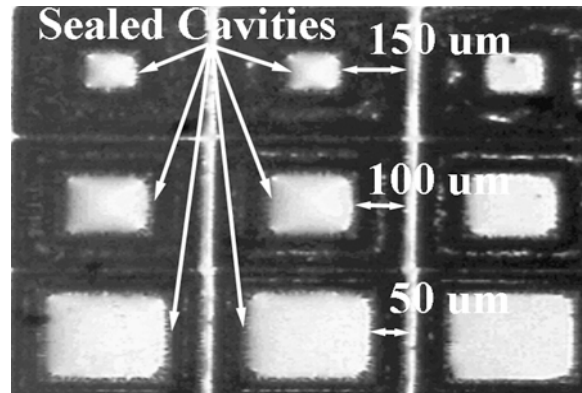


Fig. 87. Sealed cavities by RTP bonding with solder widths of 50, 100 and 150 μm .

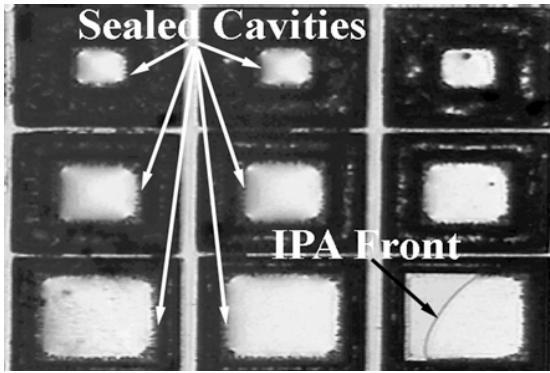


Fig. 88. Hermetic sealing is demonstrated by immersing into IPA liquid.

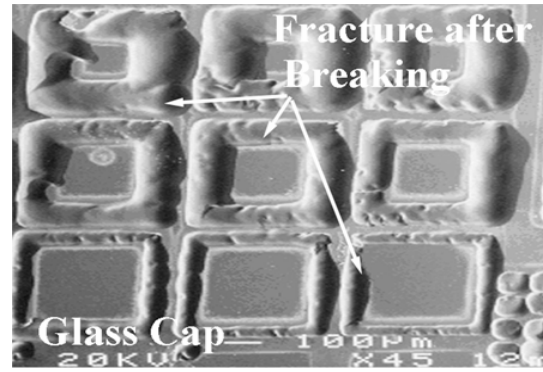


Fig. 89. Glass wafer under SEM after breaking the bond.

Two kinds of hermeticity tests were conducted: (1) IPA leak test and (2) autoclave test at 120°C and 20.7 Psi of steam for 80 minutes. IPA leak test is chosen because it is easier for IPA than water to penetrate small bonding defects in detecting gross leakage. In the preliminary characterizations, 21 samples have been tested for 240 hours, as shown in Figure 90. As expected, cavities with thick and wide aluminum solder have better survival rate. It is found that the survival rate reaches 100 % if the aluminum solder has width of 150 μm and thickness of 3.8 μm. However, even in the worst case when the solder width is 50 μm and the thickness is 3.2 μm, more than 40% of cavities still passed the IPA leak test. The major cause of failure is believed to be the lack of proper bonding pressure. In this bonding set up, the bonding pressure is provided only from the gravity force of the glass cap. As a result, non-uniform pressure distribution is expected during the RTP bonding process and failure occurs when the glass cap and the aluminum solder failed to have intimate contact. A mechanical fixture is currently under design to provide better bonding pressure and to improve the RTP bonding results.

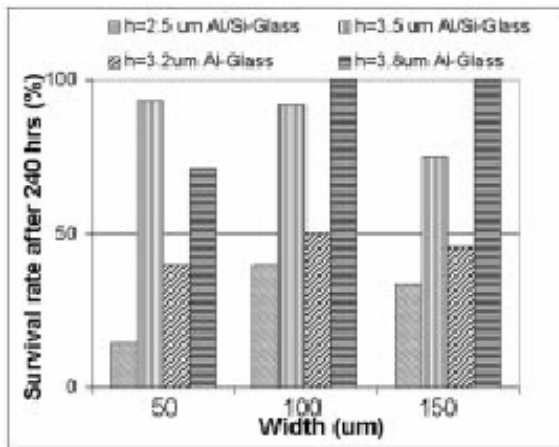


Fig. 90. IPA leak test by immersing packaged die into IPA for 240 hours. Where "h" is the aluminum solder thickness.

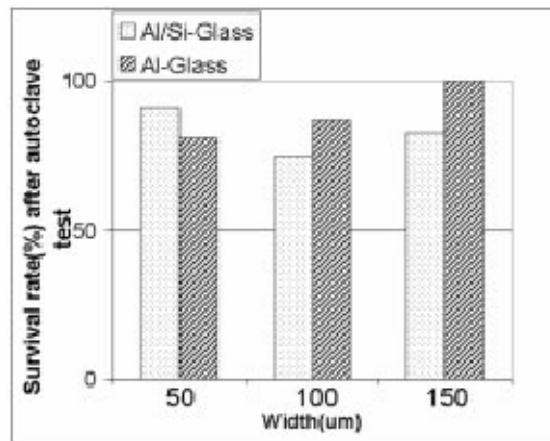


Fig. 91. Autoclave test by putting die into a 120°C, 20.7 Psi steam chamber for 80 minutes after passing IPA tests.

After the gross IPA leak test, successfully packaged cavities are put into autoclave chamber for tests under harsh environment. The average survival rate is 75% and reaches

100% for cavities with wide and thick (such as 150 μm wide and 4.5 μm thick) aluminum solder, as shown is Figure 91. RTP bonding could have introduced severe thermal stress and possible failure mechanisms to cause long-term stability problems. However, the autoclave testing serves as accelerated testing and the results prove that good reliability by RTP bonding can be accomplished.

A hermetic glass-silicon package formed by RTP aluminum-to-nitride bonding has been demonstrated and characterized by means of accelerated hermeticity testing. Surface-micromachined comb-drive resonators have been hermetically packaged and tested in an autoclave chamber (130°C, 2.7 atm and 100%RH). In order to determine the reliability of the package, the life time data are first fit with a Lognormal model and analyzed using maximum likelihood estimator, as shown in Figure 92. The results show that for packages with sealing ring width of 200 μm and average sealing area of 1000 x 1000 μm^2 , the lower 90% interval of mean time to failure (MTTF) is estimated as 270 years under jungle condition (35°C, 1 atm and 95% RH). Thermal shock and temperature cycling tests between -195 and 200°C for 20 cycles have been performed, and only 2 out of 59 packages were found failed after the test.

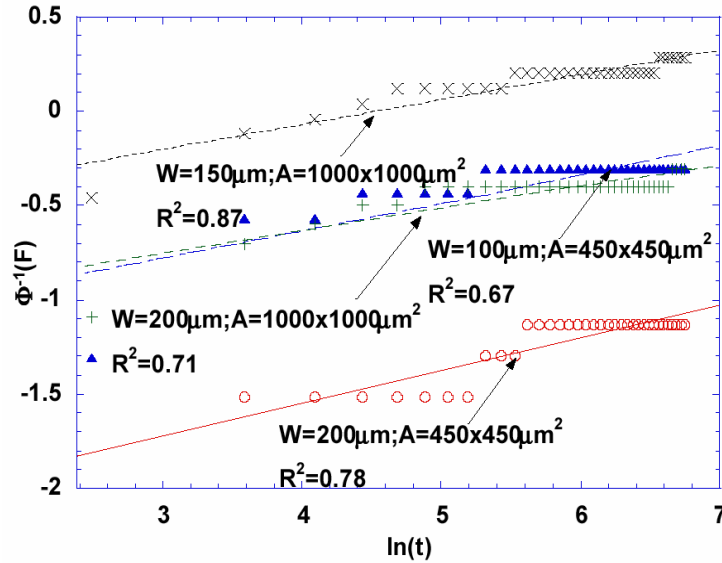


Fig. 92. Statistical failure function versus time for accelerated testing analysis.

4.3 Task III: Massively Selective Trimming

4.3.1 Frequency Tuning Using Electro-Thermal Effects

The first scheme developed in this task is based on localized resistive heating for active frequency tuning [24]. The innovative scheme is applied to a comb-shape resonator, as illustrated in Figure 93. The tuning beam is to be locally heated to generate stress and to alter the resonant frequency of the structure. Thermal stressing effects of this tuning beam have been successfully modeled, simulated and experimentally demonstrated. Two major characterizations have been accomplished: electrothermal responses and dynamic responses.

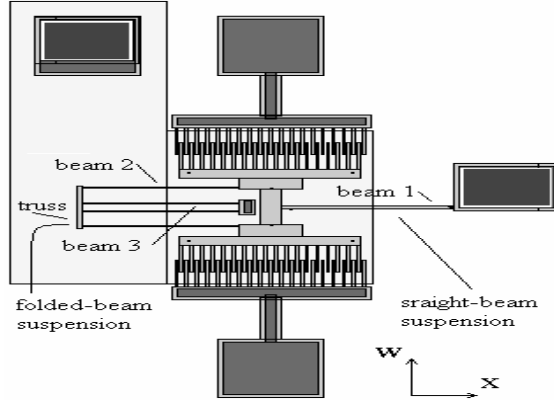


Fig. 93. Schematic diagram of a tunable comb-shape resonator. Beam 1 is the heating and tuning beam.

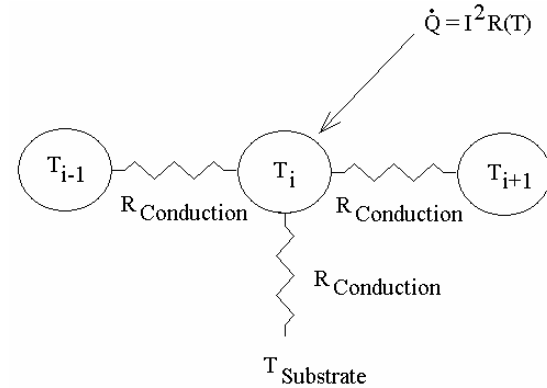


Fig. 94. Electrothermal model showing the elements of each discrete node. A total of 124 nodes were used.

The thermal model developed was a discrete time and space model. The device was first split into smaller thermal masses. The straight-beam suspension was split into 40 pieces, the folded beam suspension was split into 124 pieces, and the central rigid portion was split into two large masses. Each of these masses is treated as shown in Figure 94, where T_i is the temperature of the i -th node and $T_{\text{substrate}}$ is the temperature of the substrate which is assumed to remain constant at room temperature. $I^2 R(T)$ is the power going into the i -th node where I is the current flowing through the node and R is the electrical resistance of the node. With this model the transient responses of the temperature versus time can be graphed as seen in Figure 95. From this model, the temperature rise and fall times of the system are found to be around 140 μsec . Using the model developed above, a temperature profile of the system at a time significantly larger than the rise time can be attained. The temperature profile of the system for a given input current is shown in Figure 96 where nodes 1-25 are the inner portion of the folded-beam suspension, nodes 26-32 are the truss portion of the folded-beam suspension, nodes 33-58 are the outer portion of the folded-beam suspension, node 59 is the rigid central mass, and nodes 60-100 are the straight-beam suspension. Experimentally, we found the highest temperature spot agrees with what is predicted analytically. Therefore, we conclude that this electrothermal model for localized heating is feasible to predict the electrothermal responses of the system.

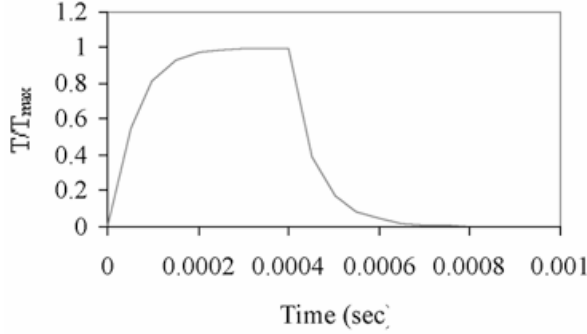


Fig. 95. Transient temperature simulation. indicates 0.2 msec is required for heating to reach steady state.

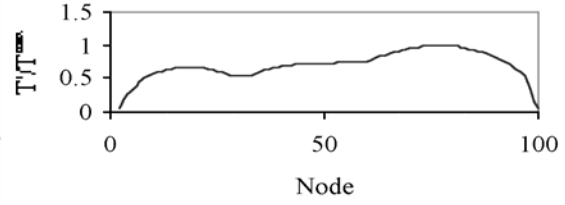


Fig. 96. Temperature distribution of the microsystem based on the electrothermal model.

This localized heating will cause local thermal stress and affect the resonant frequency of the comb-resonator. A simplified dynamic model is derived to characterize these effects. Shown in Figure 97 is the simplified model where K_x is the stiffness of the truss in the folded-beam suspension in the x direction. The stiffness of the folded-beam suspension in the w direction is k. The straight-beam suspension has moment of inertia, I, cross-sectional area, A, and length L. E is the Young's modulus and ρ is the density of polysilicon. M_{eff} is the effective mass of the combination of the folded-beam suspension and the rigid central portion of the device. In deriving the governing equation, the softening effect of the spring is ignored as the beam deflects because the compressive force P due to the heating is the dominant effect. The equations of motion governing the transverse vibration $w(x,t)$ as a function of the position x along the length of the beam and the time t is given by a linear partial differential equation. It can be solved with correct boundary and initial conditions.

Five different structures from four different dice are tested over a range of tuning powers. The change in resonance verses the applied tuning power is plotted for the 5 different devices along with the predicted theoretical response in Figure 98(a). As seen in the plot the theory predicts a quasi-linear change in resonance verses power and the experimental data points are close to the theoretical prediction when the input power is lower than 30 mW. However, the model does not take into account several secondary effects, including non-linearities due to the softening of the spring as the structure deflects, the change in specific heat, thermal conductivity, or the thermal coefficient of expansion as the temperature increases.

The frequency response of the resonator was measured. The driving frequency is changed every 100 Hz and the amplitude is recorded. This is done scanning both into the higher frequencies and into the lower frequencies until the amplitude is relatively low. Several tuning currents are conducted and recorded as shown in Figure 98(b) from 0 mA to 5 mA. As seen in the plot the system starts out with a fairly linear response. As the tuning current is increased the response begins to go more and more non-linear. This effect is to be expected. Non-linearities arise from the stiffening of the straight-beam suspension as the device deflects and the stiffening comes from the stretching of the beam as it deflects.

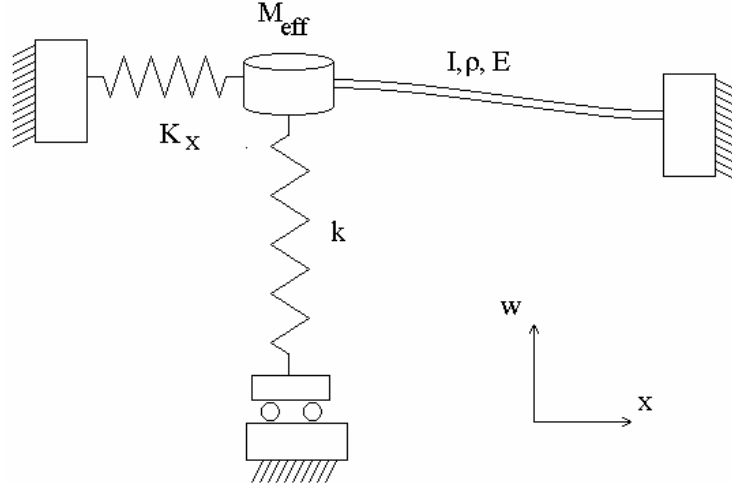


Fig. 97. A simplified model for dynamic analysis.

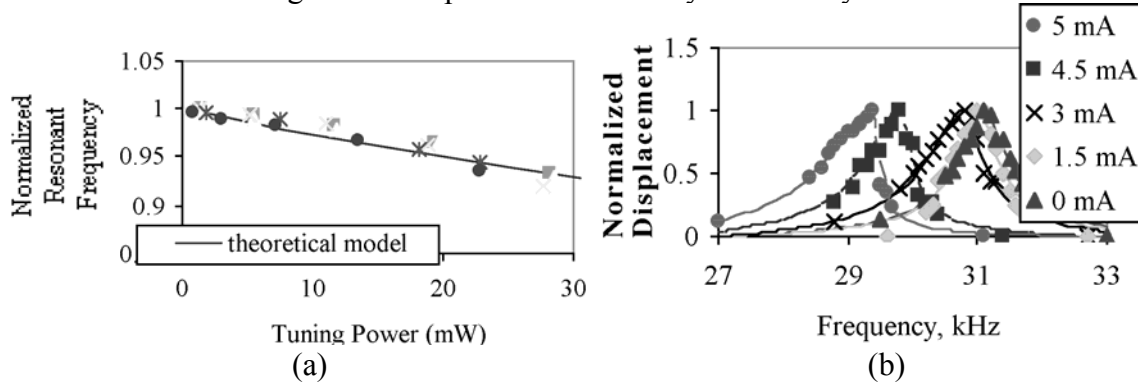


Fig. 98. (a) Frequency response of a tunable resonator at 5 different tuning amperages. (b) Variation of resonant frequency vs. tuning power for 5 different devices compared to theoretical model.

4.3.2 Frequency Tuning Using Localized CVD Deposition

The second frequency tuning scheme is based on localized CVD process, as discussed in section 4.2.2. Frequency tuning is required in micro-resonators because variations in micromachining processes cause frequency scatter in the devices. Telecommunication applications require operation at precise frequencies. Costs are reduced by batch processing, but devices that deviate from frequency specifications must be rejected and this reduces the process yield. Selective polysilicon deposition was developed to correct variations in devices after fabrication by adding material [25]. It consisted of electrically-heating suspended polysilicon structures in a silane environment to locally decompose the gas and deposit polysilicon. Its application to frequency tuning is summarized below. A new, special comb-drive resonator, shown in Figure 99, was designed which had the standard four-beam suspension on one side replaced with a single-beam. This feature enables one to predict the location of the thermal hotspot. Another feature was the reduced section, “heater”, at the end of the single beam. It promotes deposition in the junction of the single beam and the plate of the rotor, where a higher change in frequency will occur per unit mass deposited. A third feature was folding back the end of the single beam before anchoring it, to allow the free expansion of the tip. This reduces residual stress from fabrication and heating.

The dimensions of the final device were arrived at by using finite-element simulations. A thermal-stress simulation was developed to design against buckling at deposition temperatures (typical, 500-800°C), while keeping frequency at levels measurable by optical observation (<100kHz was chosen). The buckling strength and maximum frequency of the device were competing factors. Short beams with large cross sections were required to prevent buckling at low temperatures, and relatively long beams were required to keep the frequency under 100kHz. These requirements were balanced by iteration of the design with the simulations. In a particular tuning experiment, a special comb-drive resonator had initial frequency of 85.9kHz. Selective polysilicon deposition was performed by gradually applying voltage across the rotor until the power dissipation reached 10mW. The total process time was about 15 minutes. Polysilicon was deposited in islands on the single beam, as shown in Figure 100. The resonant frequency increased 2.6%. Data were collected from a dozen other samples where selective deposition was performed by other procedures. Depending on the initial resistance of the sample, the power dissipation during heating and process time used, some variability in the deposited polysilicon (volume and texture) was found. Continuously and uniformly deposited layers, judged to be the best, were found for longer process times. Increases in frequency from 0.7% to 2% were obtained. For certain continuous and uniform depositions, the percent change in frequency due to the location and amount of deposition was determined and validated by using simulation. Suggested future work includes developing in situ frequency tuning and characterizing the thermal properties of polysilicon for modeling.

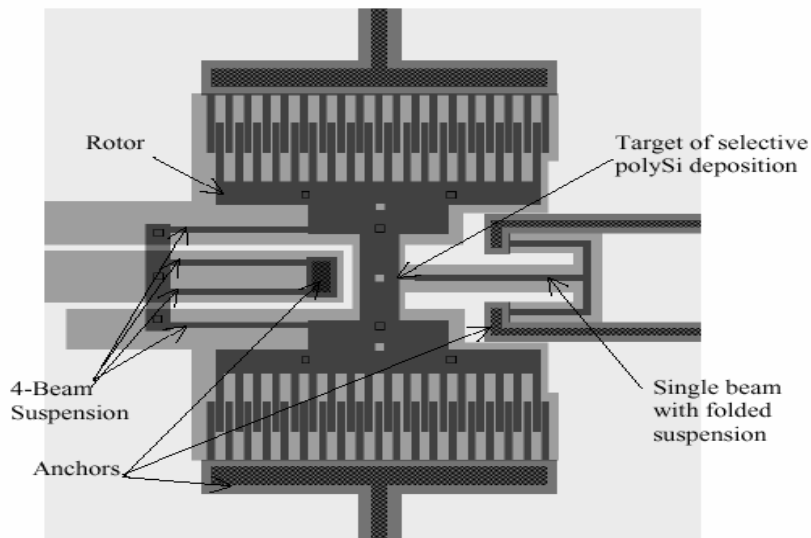


Fig. 99. Design layout of the special comb-drive resonator for tuning using selective polysilicon deposition.

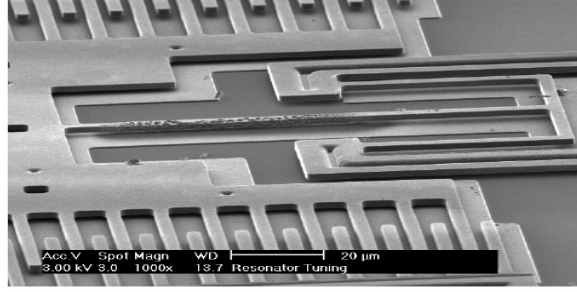


Fig. 100. SEM of special comb-drive resonator with selectively deposited polysilicon. The change in resonant frequency was 2.6%.

4.3.3 Frequency Tuning Using Pulsed Laser Deposition (PLD)

The third frequency tuning scheme is based on localized, pulsed laser deposition as illustrated in Figure 101 for post-packaging natural frequency tuning of micro resonators [26]. Following the RTP Al-to-nitride bonding process described in section 4.2.4, the flip-chip assembled pair of device wafer and glass cap wafer is loaded into a quartz envelope. After heating for 10 seconds at 750°C, a bond is formed. A pulsed laser is then introduced to locally vaporize the metal film above the target resonator.

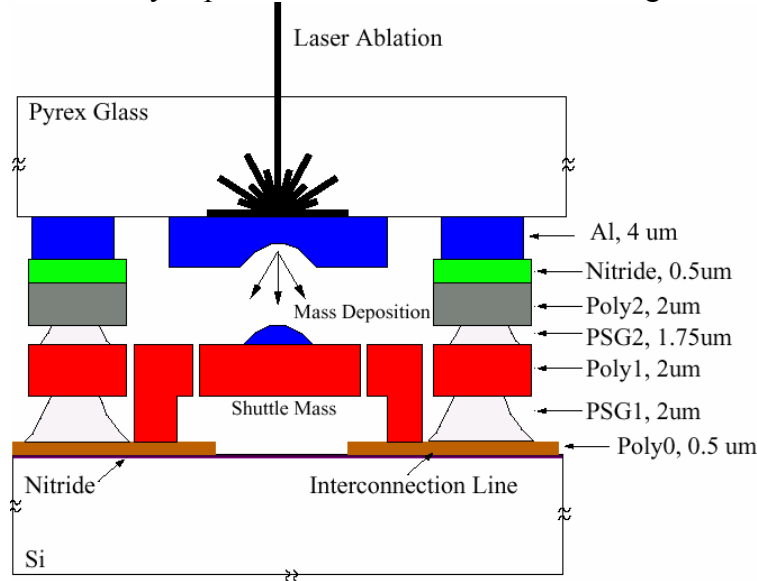


Fig. 101. The schematic diagram of the post-packaging frequency tuning process by PLD for MEMS resonators.

Under the laser power, the metal was evaporated and then re-deposited onto the resonator to change (lower) the natural frequency of the resonator, as shown in Figure 102. Figure 103 shows the spectrum of a resonator before and after PLD frequency tuning. A frequency shift (Δf , in %) of -1.2% is observed. Figure 104 shows the experimental results of Δf versus $[(m_0/(m_0+\Delta m))^{0.5}-1]$, where m_0 and Δm are the resonator's original mass and the mass deposited by PLD, respectively. In the analysis, m_0 is calculated using the comb-resonator mask layout and Δm is estimated using image processing software to measure the deposition area. The theoretical response of Δf versus $[(m_0/(m_0+\Delta m))^{0.5}-1]$ is linear from an undamped spring-mass vibration model, as

shown in Figure 104, and the experimental data correspond to the analytical prediction well. Moreover, a maximum frequency-shift of -18.1% is demonstrated.

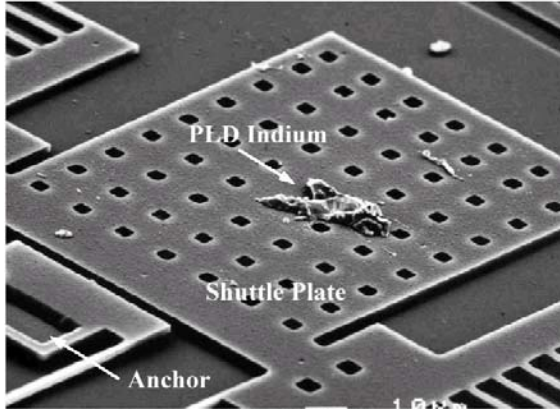


Fig. 102. SEM microphoto shows indium is deposited onto a resonator shuttle plate using PLD.

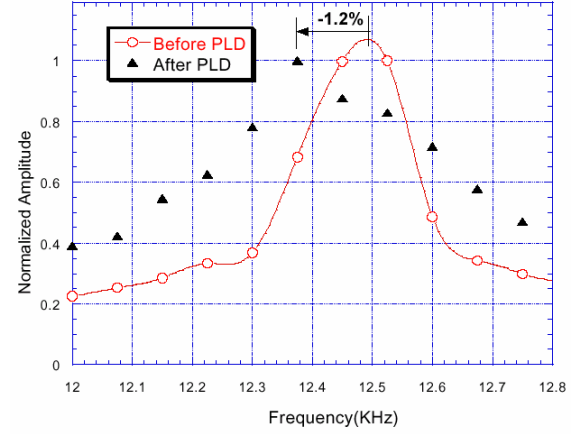


Fig. 103. Spectrum measured by a micro-stroboscope for a resonator before and after PLD. A frequency shift of -1.2% is observed.

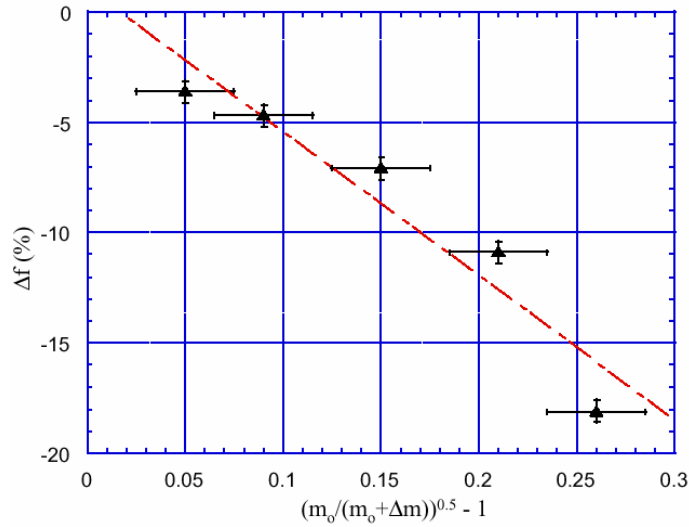


Fig. 104. Experimental results showing the linear correspondence of Δf and $[(m_0/(m_0 + \Delta m))^{0.5} - 1]$ as predicted by the undamped vibration model.

5.0 Conclusions and Recommendations

5.1 Conclusions

This project has achieved many major accomplishments toward “Massively Parallel Post-Packaging for MEMS.” These achievements can be summarized in three areas: (1) innovative bonding processes; (2) post-fabrication packaging demonstrations and characterizations on various MEMS devices; and (3) demonstrations and characterizations of post-fabrication device trimming. This final report covers many aspects of these accomplishments. Additional detailed results and procedures can be found in well-documented conference publications and journal publications as listed at the end of this final report. An overview of the project, including background information was published in IEEE Transactions on Advanced Packaging [27] and it provides the motivation and approaches for the major directions of the project. In summary, we were able to develop several new bonding processes, including localized eutectic bonding process, localized fusion bonding process, localized solder bonding process, localized CVD bonding process, localized nano-second laser welding process, localized inductive heating and bonding process, localized ultrasonic bonding process and RTP bonding process. Every new bonding process represents technology innovation and advancement. In combination of these new bonding processes, new material bonding systems were also investigated and established. These include aluminum-to-glass, aluminum-to-nitride, and aluminum-to-aluminum bonding systems. The new bonding processes and systems make possible the device encapsulation demonstrations such as vacuum encapsulated micro resonators by using localized aluminum-to-glass bonding, by using RTP bonding and by using localized CVD bonding. These vacuum bonded devices have gone through various types of characterization, including quality factor measurements, long-term stability monitoring and accelerated tests. In the other device packaging area, selective trimming of micro resonators were successfully demonstrated by three different schemes, including active trimming by localized heating and stressing effect, permanent trimming by localized CVD deposition and by pulsed laser deposition. We are confident that these new and innovative technologies and demonstrations will make a great impact on MEMS packaging research and commercial applications as well as military applications in the future.

5.2 Recommendations

We feel obligated to provide recommendations and future directions because there are many MEMS packaging research areas that require further developments. Among the new packaging processes we have established in this program, localized bonding schemes based on resistive heating will be best applicable for device level packaging applications due to the constraint that heating current has to be physically applied to the resistors. Although wafer-level packaging is possible and was proposed [28], it goes beyond the scope of University research and requires much development work because the foundations of the approach were provided by this project. Similar recommendations apply to the methods of localized nano-second welding, localized CVD bonding, localized induction heating and localized ultrasonic bonding processes. Among these, we feel that localized CVD and ultrasonic bonding processes require very dedicated process control to minimize the possible thermal stress and may require more

development effort to stabilize the process parameters as compared to the localized nano-second laser welding and localized induction heating and bonding methods. Furthermore, it is recommended that all of the remote heating methods (induction, laser, ultrasonic) be applied on the wafer-level with the assistance of an X-Y stage. As such, only individual areas on the wafer will be processed at one time to reduce the possible thermal stress effects. Because these methods provide very fast bonding results, the packaging process will be accomplished in relatively short time.

In the device encapsulation area, we feel that many investigations should be continued. These include the long-term monitoring of the sensor performance (such as quality factor), more accelerated tests for the life prediction of sensors, other reliability issues associated with microstructures as well as MEMS packaging processes. In this project, we opened up several research fronts in the area of MEMS packaging and device evaluation. For example, comb-shape resonators were first vacuum encapsulated by the newly developed bonding processes. Long-term tests and accelerated tests were then conducted to evaluate both the packaging process and the reliability of the microstructures. Unfortunately, in the University environment, we can only fabricate and test limited number of microstructures and the very comprehensive analyses of these reliability-related issues should be conducted by statistical data. One possible future direction in this area is to collaborate with industrial companies and gather statistical data from their database for statistical analyses. Another area to be addressed further is the failure mechanism of the packaged devices. Would most of the failures come from the packaging process or the microstructures? After the failure mechanisms are identified, what are the ways to prevent failure or to improve the lifetime of the devices? If these technical and research issues can be addressed in the near future, it will help the future development of the MEMS research, devices and commercial products tremendously.

In the device trimming area, it becomes important but inevitable when MEMS devices are ready for the commercial market. The fine manufacturing process just cannot overcome the natural variations inherit in these microstructures. As a result, device trimming and adjustment will be necessary. We have developed several new trimming schemes with excellent demonstration results in this project. However, it will be difficult to implement some of the processes in a real industrial setup and will require more research in these areas. For example, both the localized CVD process and pulsed laser deposition process will require on-chip control and monitoring circuit to adjust the trimming processes when needed. The logistics and approach were detailed in this project [29, 30]. Once this control mechanism is established, massively parallel trimming process can be accomplished.

Bibliography

- [1] R.R. Tummala, E.J. Rymaszewski (eds), "Microelectronics Packaging Handbook", Van Nostrand Reinhold, New York, 1989.
- [2] G. Wallis and D. Pomerantz, "Filed Assisted Glass-Metal Sealing", *J. of Applied Physics*, Vol. 40, pp. 3946-3949, 1969.
- [3] K.E. Peterson, P. Barth, et al., "Silicon Fusion Bonding for Pressure Sensors", *1988 Solid-State Sensor and Actuator Workshop*, Hilton Head, pp. 144-147, 1988.
- [4] J.J. Sniegowski, H. Guckel and R.T. Christenson, "Performance Characteristics of Second Generation polysilicon Resonating Beam Force Transducers", *IEEE Solid-State Sensor and Actuator Workshop*, Hilton Head Island, 9-12, 1990.
- [5] Liwei Lin, K. McNair, R.T. Howe and A.P. Pisano, "Vacuum Encapsulated Lateral Microresonators", *7th Int. Conference on Solid State Sensors and Actuators*, pp. 270-273, Yokohama, Japan, June, 1993.
- [6] T.A. Core, W.K. Tsang, and S. Sherman, "Fabrication Technology for an Integrated Surface-Micromachined Sensor", *Solid State Technology*, October, pp. 39-47, 1993.
- [7] See the Supporting Letter from Dr. John "Jack" Martin, Leader in MEMS Micropackaging, Analog Devices Inc.
- [8] M.-H Kiang, O. Solgaard, R.S. Muller and K.Y. Lau, "Surface-Micromachined Electrostatic-Comb Driven Scanning Micromirrors for Barcode Scanners", *1996 Micro Electro Mechanical Systems Workshop*, pp. 192-197, 1996.
- [9] For example, see some of the programs currently running at DARPA/ETO/MICROFLUIDICS.
- [10] Liwei Lin, C.T.-C. Nguyen, R.T. Howe and A.P. Pisano, "Micro Electromechanical Filters for Signal Processing", *1992 Micro Electro Mechanical Systems Workshop*, pp. 226-231, 1992.
- [11] W.C. Tang, C.T.-C. Nguyen and R.T. Howe, "Laterally Driven Polysilicon Resonant Microstructures", *Sensors and Actuators*, Vol. A20, pp.25-32, 1989.
- [12] Liwei Lin, Y.T. Cheng and K. Najafi, "Formation of Silicon-Gold Eutectic Bond Using Localized Heating Method," *Japanese Journal of Applied Physics, Part II*, Vol. 11B, pp. 1412-1414, Nov. 1998.
- [13] Y.T. Cheng, Liwei Lin and Khalil Najafi, "Localized Silicon Fusion and Eutectic Bonding for MEMS Fabrication and Packaging," *IEEE/ASME Journal of Microelectromechanical Systems*, Vol. 9, pp. 3-8, March 2000.
- [14] Y.T. Cheng, Liwei Lin and K. Najafi, "A Hermetic Glass-Silicon Package Formed Using Localized Aluminum/Silicon-Glass Bonding," *IEEE/ASME Journal of Microelectromechanical Systems*, Vol. 10, No. 3, pp. 392-399, 2001.
- [15] A. Cao and Liwei Lin, "Selective Induction Heating for MEMS Packaging and Fabrication," 2001 ASME International Mechanical Engineering Congress and Exposition, Proceedings of the MEMS Symposia, CD ROM, Vol. 2, New York, New York, Nov. 2001.
- [16] Cheng Luo and Liwei Lin, "The Application of Nanosecond-Pulsed Laser Welding Technology in MEMS Packaging with a Shadow Mask," *Sensors and Actuators*, Vol. A 97-98, pp. 398-404, 2002.

- [17] J.B. Kim, M. Chiao and Liwei Lin, "Ultrasonic Bonding of In/Au and Al/Al for Hermetic Sealing of MEMS Packaging," Proceedings of IEEE Micro Electro Mechanical Systems Conference, pp. 415-418, Las Vegas, Jan. 2002.
- [18] D. Bystrom and Liwei Lin, "Residual Stress Analysis of Silicon-Aluminum-Glass Bonding Processes," 2002 ASME International Mechanical Engineering Congress and Exposition, Proceedings of the MEMS Symposium, to appear, New Orleans, Louisianan, November 2002.
- [19] Y.T. Cheng, W.T. Hsu, K. Najafi, C.T. Nguyen and Liwei Lin, "Vacuum Packaging Technology Using Localized Aluminum/Silicon-to Glass Bonding," *IEEE/ASME Journal of Microelectromechanical Systems*, Vol. 11, pp. 556-565, 2002.
- [20] G.H. He, Liwei Lin and Y.T. Cheng, "Localized CVD Bonding for MEMS Packaging," *10th Int. Conference on Solid State Sensors and Actuators, Transducer's 99*, Technical Digest, Sendai, Japan, June 1999, pp. 1312-1315.
- [21] K.B. Lee and Liwei Lin, "Zinc Bonding for MEMS Packaging at the Wafer-Level," 2001 ASME International Mechanical Engineering Congress and Exposition, Proceedings of the MEMS Symposia, CD ROM, Vol. 2, New York, New York, Nov. 2001.
- [22] Mu Chiao and Liwei Lin, "Hermetic Wafer Bonding Based on Rapid Thermal Processing," *Sensors and Actuators*, Vol. 91A, pp. 404-408, July 2001.
- [23] Mu Chiao and Liwei Lin, "A Wafer-Level Vacuum Packaging Process by RTP Aluminum-to-Nitride Bonding," *Technical Digest of Solid-State Sensors and Actuators Workshop*, pp. 81-85, Hilton Head Island, June 2002.
- [24] Todd Remtema and Liwei Lin, "Active Frequency Tuning for Microresonators by Localized Thermal Stressing Effects," *Sensors and Actuators*, Vol. 91A, pp. 326-332, July, 2001.
- [25] D. Joachim and Liwei Lin, "Selective Polysilicon Deposition for Frequency Tuning of MEMS Resonators," Proceedings of IEEE Micro Electro Mechanical Systems Conference, pp. 727-730, Las Vegas, Jan. 2002.
- [26] M. Chiao, "MEMS Packaging by Rapid Thermal Processing," PhD dissertation, Mechanical Engineering Department, UC-Berkeley, May 2002.
- [27] Liwei Lin, "MEMS Post-Packaging by Localized Heating," *IEEE Trans. on Advanced Packaging*, Vol 23, pp. 608-616, Nov. 2000.
- [28] Y.T. Cheng, "Localized Heating and Bonding Technique for MEMS Packaging," PhD dissertation, Electrical Engineering and Computer Science Department, The University of Michigan, Dec. 2000.
- [29] P.P.L. Chang-Chien, "Silicon-Glass Wafer-Level Encapsulation with in-Chamber Vacuum-Level Control," PhD dissertation, Electrical Engineering and Computer Science Department, The University of Michigan, May 2002.
- [30] D. Joachim, "Selective Deposition of Polycrystalline Silicon for Tuning Microelectromechanical Resonators: Experiment and Simulation," PhD dissertation, Mechanical Engineering Department, The University of Michigan, May 2001.

List of Publications

Journals

- [1] Cheng Luo and Liwei Lin, "The Application of Nanosecond-Pulsed Laser Welding Technology in MEMS Packaging with a Shadow Mask," *Sensors and Actuators*, Vol. A 97-98, pp. 398-404, 2002.
- [2] M. Chiao and Liwei Lin, "Accelerated Hermeticity Testing of a Glass-Silicon Package Formed by RTP Aluminum-to-Silicon Nitride Bonding," *Sensors and Actuators*, Vol. A 97-98, pp. 405-409, 2002.
- [3] Y.T. Cheng, Liwei Lin and K. Najafi, "A Hermetic Glass-Silicon Package Formed Using Localized Aluminum/Silicon-Glass Bonding," *IEEE/ASME Journal of Microelectromechanical Systems*, Vol. 10, No. 3, pp. 392-399, 2001.
- [4] Jr-Hung Tsai and Liwei Lin, "Micro-to-Macro Fluidic Interconnectors with an Integrated Polymer Sealant," *Journal of Micromechanics and Microengineering*, Vol.11, No. 5, Sep. pp. 577-581, 2001.
- [5] Mu Chiao and Liwei Lin, "Hermetic Wafer Bonding Based on Rapid Thermal Processing," *Sensors and Actuators*, Vol. 91A, pp. 404-408, July 2001.
- [6] Todd Remtema and Liwei Lin, "Active Frequency Tuning for Microresonators by Localized Thermal Stressing Effects," *Sensors and Actuators*, Vol. 91A, pp. 326-332, July 2001.
- [7] Liwei Lin (position paper), "MEMS Packaging at the Wafer Level," *Journal of Materials Processing and Manufacturing Science*, Vol. 8, No. 4, pp.347~349, 2000.
- [8] Liwei Lin, "MEMS Post-Packaging by Localized Heating," *IEEE Trans. on Advanced Packaging*, Vol 23, pp. 608-616, Nov. 2000.
- [9] Y.T. Cheng, Liwei Lin and Khalil Najafi, "Localized Silicon Fusion and Eutectic Bonding for MEMS Fabrication and Packaging," *IEEE/ASME Journal of Microelectromechanical Systems*, Vol. 9, pp. 3-8, March 2000.
- [10] Mu Chiao and Liwei Lin, "Self-Buckling of Micromachined Beams Under Resistive heating," *IEEE/ASME Journal of Microelectromechanical Systems*, Vol. 9, pp. 146-151, March 2000.
- [11] Liwei Lin, Y.T. Cheng and K. Najafi, "Formation of Silicon-Gold Eutectic Bond Using Localized Heating Method," *Japanese Journal of Applied Physics, Part II*, Vol. 11B, pp. 1412-1414, Nov. 1998.
- [12] Y.T. Cheng, W.T. Hsu, K. Najafi, C.T. Nguyen and Liwei Lin, "Vacuum Packaging Technology Using Localized Aluminum/Silicon-to Glass Bonding," *IEEE/ASME Journal of Microelectromechanical Systems*, Vol. 11, pp. 556-565, 2002.
- [13] Liwei Lin, "Thermal Challenges in MEMS Applications: Phase Change Phenomena and Thermal Bonding Processes," *Microelectronics Journal*, accepted.
- [14] D. Joachim and Liwei Lin, "Selective Polysilicon Deposition for Frequency Tuning of MEMS Resonators," *IEEE/ASME Journal of Microelectromechanical Systems*, accepted.

Conferences

- [1] Mu Chiao and Liwei Lin, "A Wafer-Level Vacuum Packaging Process by RTP Aluminum-to-Nitride Bonding," *Technical Digest of Solid-State Sensors and Actuators Workshop*, pp. 81-85, Hilton Head Island, June 2002.

- [2] A. Cao, M. Chiao and Liwei Lin, "Selective and Localized Wafer Bonding Using Induction Heating," *Technical Digest of Solid-State Sensors and Actuators Workshop*, pp. 153-156, Hilton Head Island, June 2002.
- [3] P.P.L. Chang-Chien, and K.D. Wise, "A Barometric Pressure Sensor with Integrated Reference Pressure Control Using Localized CVD," *Technical Digest of Solid-State Sensors and Actuators Workshop*, pp. 90-93, Hilton Head Island, June 2002.
- [4] D. Joachim and Liwei Lin, "Selective Polysilicon Deposition for Frequency Tuning of MEMS Resonators," *Proceedings of IEEE Micro Electro Mechanical Systems Conference*, pp. 727-730, Las Vegas, Jan. 2002.
- [5] Mu Chiao and Liwei Lin, "Vacuum packaging of microresonators by rapid thermal processing," *Proceedings of SPIE on Smart Electronics, MEMS, and Nanotechnology*, Vol. 4700, No. 37, San Diego, March 17-21, 2002.
- [6] J.B. Kim, M. Chiao and Liwei Lin, "Ultrasonic Bonding of In/Au and Al/Al for Hermetic Sealing of MEMS Packaging," *Proceedings of IEEE Micro Electro Mechanical Systems Conference*, pp. 415-418, Las Vegas, Jan. 2002.
- [7] (Invited Lecture)Liwei Lin, "Thermal Challenges in MEMS Applications: Phase Change Phenomena and Thermal Bonding Processes," *Proceedings of the International Conference Thermes 2002, Thermal Challenges in Next Generation Electronic Systems*, pp.35-44, Santa Fe, Jan. 2002.
- [8] K.B. Lee and Liwei Lin, "Zinc Bonding for MEMS Packaging at the Wafer-Level," 2001 ASME International Mechanical Engineering Congress and Exposition, *Proceedings of the MEMS Symposia*, CD ROM, Vol. 2, New York, New York, Nov. 2001.
- [9] A. Cao and Liwei Lin, "Selective Induction Heating for MEMS Packaging and Fabrication," 2001 ASME International Mechanical Engineering Congress and Exposition, *Proceedings of the MEMS Symposia*, CD ROM, Vol. 2, New York, New York, Nov. 2001.
- [10] D. Joachim and Liwei Lin, "Design of MEMS Resonators for Tuning with Selective Polysilicon Deposition," 2001 ASME International Mechanical Engineering Congress and Exposition, *Proceedings of the MEMS Symposia*, CD ROM, Vol. 2, New York, New York, Nov. 2001
- [11] M. Chiao and Liwei Lin, "Accelerated Hermeticity Testing of a Glass-Silicon Package Formed by RTP Aluminum-to-Silicon Nitride Bonding," *11th Int. Conference on Solid State Sensors and Actuators, Transducer's 01*, Technical Digest, pp. 190-193, Munich, Germany, June 2001.
- [12] C. Lu and Liwei Lin and M. Chiao, "Nanosecond-Pulsed Laser Bonding with a Built-in Mask for MEMS Packaging Applications," *11th Int. Conference on Solid State Sensors and Actuators, Transducer's 01*, Technical Digest, pp. 214-217, Munich, Germany, June 2001.
- [13] P.P.L. Chang-Chien and K.D. Wise, "Wafer-Level Packaging Using Localized Mass Deposition," , *11th Int. Conference on Solid State Sensors and Actuators, Transducer's 01*, Technical Digest, pp. 182-185, Munich, Germany, June 2001.
- [14] Y.T. Cheng, W.T. Hsu, Liwei Lin, C.T. Nguyen and K. Najafi, "Vacuum Packaging Technology Using Localized Aluminum/Silicon-to Glass Bonding," *Proceedings of IEEE Micro Electro Mechanical Systems Conference*, pp. 18-21, Jan. 2001, Interlaken, Switzerland.

- [15] Mu Chiao and Liwei Lin, "Hermetic Wafer Bonding Based on Rapid Thermal Processing," *Technical Digest of Solid-State Sensor and Actuator Workshop*, pp. 347-350, Hilton Head Island, June 2000.
- [16] Todd Remtema and Liwei Lin, "Active Frequency Tuning for Microresonators by Localized Thermal Stressing Effects," *Technical Digest of Solid-State Sensor and Actuator Workshop*, pp. 363-366, Hilton Head Island, June 2000.
- [17] Y.T. Cheng, Liwei Lin and K. Najafi, "Fabrication and Hermeticity Testing of a Glass-Silicon Package Formed Using Localized Aluminum/Silicon-to-Glass Bonding," *Proceedings of IEEE Micro Electro Mechanical Systems Workshop*, pp. 757-762, Jan. 2000, Miyazaki, Japan.
- [18] D. Joachim and Liwei Lin, "Localized Deposition of Polysilicon for MEMS Post-Fabrication Processing," 1999 ASME International Mechanical Engineering Congress and Exposition, *Proceedings of Micro-Electro-Mechanical Systems(MEMS)*, MEMS-Vol. 1, pp. 37-42, Nashville, Tennessee, 1999.
- [19] G.H. He, Liwei Lin and Y.T. Cheng, "Localized CVD Bonding for MEMS Packaging," *10th Int. Conference on Solid State Sensors and Actuators, Transducer's 99*, Technical Digest, Sendai, Japan, June 1999, pp. 1312-1315.
- [20] Yu-Ting Cheng, Liwei Lin and Khalil Najafi, "Localized Bonding with PSG or Indium Solder as Intermediate Layer," *Proceedings of IEEE Micro Electro Mechanical Systems Workshop*, pp. 285-289, Jan. 1999, Orlando, Florida
- [21] Liwei Lin (Invited Paper), "Micro-Mechanics in MEMS Development," 1998 *International Conference on Mechatronic Technology*, pp. 167-172, Nov. 30 - Dec. 2, 1998, Hsin-Chu, Taiwan
- [22] Liwei Lin, R.T. Howe and A.P. Pisano, "Microelectromechanical Filters for Signal Processing," *IEEE/ASME Journal of Microelectromechanical Systems*, Vol. 7, pp. 286-294, Sep. 1998.
- [23] Y.T. Cheng, Liwei Lin and Khalil Najafi, "Localized Silicon Fusion and Eutectic Bonding for MEMS Fabrication and Packaging," *Proceedings 1998 Solid-State Sensors and Actuators Workshop*, pp. 233-236, Hilton Head, SC, June 7-10, 1998.
- [24] D. Bystrom and Liwei Lin, "Residual Stress Analysis of Silicon-Aluminum-Glass Bonding Processes," 2002 ASME International Mechanical Engineering Congress and Exposition, *Proceedings of the MEMS Symposium*, to appear, New Orleans, Louisianan, November 2002.